



**Development and Implementation of a Biomechanical
Multibody Model for Human Motion Analysis**

Maria Leonor de Barros Saraiva

UMinho | 2022



Universidade do Minho

Escola de Engenharia

Maria Leonor de Barros Saraiva

**Development and Implementation of a
Biomechanical Multibody Model for
Human Motion Analysis**

outubro de 2022



Universidade do Minho

Escola de Engenharia

Maria Leonor de Barros Saraiva

**Development and Implementation of a
Biomechanical Multibody Model for
Human Motion Analysis**

Dissertação de Mestrado

Mestrado Integrado em Engenharia Biomédica

Biomateriais, Reabilitação e Biomecânica

Trabalho efetuado sob orientação de

Professor Doutor João Paulo Flores Fernandes

Professor Doutor Pedro Filipe Lima Marques

DIREITOS DE AUTOR E CONDIÇÕES DE UTILIZAÇÃO DO TRABALHO POR TERCEIROS

Este é um trabalho académico que pode ser utilizado por terceiros desde que respeitadas as regras e boas práticas internacionalmente aceites, no que concerne aos direitos de autor e direitos conexos.

Assim, o presente trabalho pode ser utilizado nos termos previstos na licença abaixo indicada.

Caso o utilizador necessite de permissão para poder fazer um uso do trabalho em condições não previstas no licenciamento indicado, deverá contactar o autor, através do RepositóriUM da Universidade do Minho.

Licença concedida aos utilizadores deste trabalho



Atribuição-NãoComercial
CC BY-NC

<https://creativecommons.org/licenses/by-nc/4.0/>

Acknowledgments

This space is dedicated to those who, in different ways, contributed to the development and conclusion of this dissertation. I would like to express my sincere acknowledgment to all of them.

I would first like to thank Professor Doctor Paulo Flores and Professor Doctor Filipe Marques, my supervisors, for providing me the opportunity to work in the field of Biomechanics and for their advice, supervision and guidance throughout this last project of my Integrated Master's degree. In the future, the admiration and respect I have for you will always remain. Thanks should also go to Mariana Rodrigues da Silva for her support and help during this year, and for the knowledge she was able to transmit to me, in particular with regard to the literature review methodology. Additionally, I would like to thank Professor Doctor Miguel Tavares da Silva for the advice throughout this work.

I am also grateful to my parents for supporting me in every way over these last five years of education and personal development.

Finally, I would like to express a special thanks to my boyfriend for his encouragement, trust and for being always present.

Thank you.

STATEMENT OF INTEGRITY

I hereby declare having conducted this academic work with integrity. I confirm that I have not used plagiarism or any form of undue use of information or falsification of results along the process leading to its elaboration.

I further declare that I have fully acknowledged the Code of Ethical Conduct of the University of Minho.

Abstract

Development and Implementation of a Biomechanical Multibody Model for Human Motion Analysis

The present Master's dissertation is comprised in the field of Biomechanics of Human Motion and its main purpose is to develop and implement a two-dimensional computational multibody model on the MATLAB software, to analyze the dynamic behavior of the human body and its interaction with the surrounding environment.

A multibody model of the right side of the human body is developed, with the objective of performing a dynamic analysis of the human gait, in which kinematic and kinetic data are prescribed, and all degrees-of-freedom are guided. The developed model is described under the multibody systems formulation, using cartesian coordinates, and the trajectories of the bodies that guide the biomechanical model, as well as the external applied forces were obtained from experimental data acquisition.

The contact modeling is, then, considered for the foot-ground interface, and two application examples are described and discussed. The first application example concerns a simulation of a simple leg motion, generated by the action of the gravitational force, and aims to validate the methodologies of contact geometry definition and contact detection. The second application example is presented for studying the foot-ground contact in human gait. This interaction is geometrically defined by circles positioned at specific locations on the foot plantar surface, and a plane, describing the ground. The contact is detected based on the relative interpenetration of the surfaces, and appropriate constitutive laws associated with the normal and tangential forces developed during the contact are applied. After a manual parameter adjustment method, an optimization process is implemented to obtain the most suitable values for the geometric and contact parameters of the proposed model. Finally, the results obtained from computational and experimental analysis are compared, with the aim of validating the proposed approach. The final foot-ground contact model presents good overall results for the vertical and tangential contact forces and for the center-of-pressure position.

Keywords: Biomechanics; Human Gait; Multibody Systems Formulation; Dynamic Analysis; Foot-Ground Contact Model

Resumo

Desenvolvimento e Implementação de um Modelo Biomecânico Multicorpo para Análise do Movimento Humano

A presente dissertação de Mestrado insere-se no domínio da Biomecânica do Movimento Humano e o seu principal objetivo é desenvolver e implementar um modelo computacional multicorpo bidimensional, em MATLAB, tendo em vista a análise do comportamento dinâmico do corpo humano e da sua interação com o ambiente envolvente.

Com o objetivo de realizar uma análise dinâmica da marcha humana, na qual os dados cinemáticos e cinéticos são prescritos e todos os graus-de-liberdade são guiados, é desenvolvido um modelo multicorpo do lado direito do corpo humano. O modelo é descrito sob a formulação de sistemas multicorpo, utilizando coordenadas cartesianas. As trajetórias dos corpos que guiam o modelo, bem como as forças externas nele aplicadas foram obtidas através da aquisição de dados experimentais.

Adicionalmente, a modelação do contacto é aplicada à interface pé-solo, sendo descritos e discutidos dois exemplos de aplicação. O primeiro exemplo de aplicação diz respeito a uma simulação de um movimento simples da perna, gerado pela ação da força gravítica, e tem como objetivo validar as metodologias de definição da geometria e de deteção de contacto. O segundo exemplo de aplicação é apresentado para estudar o contacto pé-solo na marcha humana. Esta interação é definida geometricamente por círculos posicionados em localizações específicas na superfície plantar do pé, e por um plano que descreve o solo. O contacto é detetado com base na pseudo-penetração das superfícies, e são aplicadas leis constitutivas associadas às forças normal e tangencial desenvolvidas no contacto. Após um ajuste manual dos parâmetros, é implementado um processo de otimização para obter os valores mais adequados dos parâmetros geométricos e de contacto do modelo proposto. Por fim, os resultados obtidos das análises computacional e experimental são comparados, com o objetivo de validar esta abordagem. O modelo de contacto pé-solo final apresenta bons resultados gerais para as forças de contacto vertical e tangencial, assim como para a posição do centro de pressão.

Palavras-Chave: Biomecânica; Marcha Humana; Formulação de Sistemas Multicorpo; Análise Dinâmica; Modelo de Contacto Pé-Solo

Contents

Acknowledgments.....	ii
Abstract.....	iv
Resumo.....	v
List of Figures.....	viii
List of Tables.....	xii
List of Abbreviations and Acronyms.....	xiv
Chapter 1 – Introduction.....	1
1.1. Motivation.....	1
1.2. Scope and Objectives.....	2
1.3. Literature Review.....	3
1.3.1. Evolution of the Human Gait Analysis.....	4
1.3.2. Foot-Ground Contact Modeling Strategies.....	5
1.4. Structure of the Dissertation.....	6
1.5. Contributions of the Work.....	8
Chapter 2 – Characterization of the Human Lower Limb.....	9
2.1. Biomechanical Considerations.....	9
2.2. Basic Anatomy.....	13
2.3. Gait Characterization.....	21
2.4. Summary.....	24
Chapter 3 – Multibody Systems Methodologies.....	26
3.1. Multibody Systems Overview.....	26
3.2. Constraints Formulation.....	31
3.2.1. Revolute Joint.....	32
3.2.2. Guiding Constraints.....	33
3.3. Description of the Equations of Motion.....	34
3.4. Resolution of the Equations of Motion.....	36
3.5. Summary.....	40

Chapter 4 – Dynamic Analysis of the Human Gait	41
4.1. Biomechanical Multibody Model Description	42
4.2. Kinematic Constraints Formulation	44
4.3. Initial Conditions and Kinematic Consistency	46
4.4. External Applied Forces	49
4.5. Results and Discussion.....	52
4.5.1. Polynomial Interpolation of the Experimental Data	53
4.5.2. Integration Algorithm for the Resolution of the Equations of Motion	56
4.5.3. Baumgarte Stabilization Method	58
4.5.4. Motion Visualization	62
4.6. Summary.....	63
Chapter 5 – Modeling of Foot-Ground Interaction	65
5.1. Generalities on Contact Problems	66
5.2. Contact Detection Methodology	67
5.3. Contact Resolution Approach.....	70
5.4. Application Example 1: Leg Drop Motion.....	74
5.5. Application Example 2: Human Gait Analysis	85
5.6. Summary.....	103
Chapter 6 – Concluding Remarks	104
6.1. Conclusions	104
6.2. Future Developments	106
References	107
Appendix I – Optimizations Results	115

List of Figures

Figure 1.1. Number of studies organized according to the contact geometry considered in the foot-ground interaction model..... 6

Figure 2.1. Anatomical reference planes and spatial coordinate system {Adapted from (Winter, 2009)}. 10

Figure 2.2. (a) Hip flexion; (b) Hip extension; (c) Knee flexion; (d) Knee extension; (e) Dorsiflexion of the foot; (f) Plantarflexion of the foot; (g) Flexion of the toes; (h) Extension of the toes {Adapted from (Muscolino, 2017)}. 11

Figure 2.3. (a) Anterior view of the bones of the lower limb; (b) Superior view of the bones of the foot {Adapted from (Tortora & Derrickson, 2010)}. 14

Figure 2.4. (a) Anterior view of the hip joint; (b) Detail of the hip joint {Adapted from (Tortora & Derrickson, 2010)}. 15

Figure 2.5. Three-joint structure of the knee. (a) Anterior view; (b) Lateral view {Adapted from (Neumann, 2010; Tortora & Derrickson, 2010)}. 15

Figure 2.6. Joints of the foot {Adapted from (Betts et al., 2017)}. 16

Figure 2.7. (a) Anterior view of the hip joint flexors; (b) Posterior view of the hip joint extensors (the adductor brevis and gluteus minimus are not represented) {Adapted from (Muscolino, 2017)}. 17

Figure 2.8. (a) Posterior view of the knee joint flexors; (b) Anterior view of the knee joint extensors (the vastus intermedius is not represented) {Adapted from (Muscolino, 2017)}. 18

Figure 2.9. (a) Anterior view of the ankle joint dorsiflexors; (b) Posterior view of the ankle joint plantarflexors {Adapted from (Muscolino, 2017)}. 19

Figure 2.10. (a) Plantar view of the flexors of the big toe; (b) Plantar view of the flexors of toes two through five; (c) Dorsal view of the extensors of the big toe; (d) Dorsal view of the extensors of toes two through five {Adapted from (Muscolino, 2017)}. 20

Figure 2.11. Phases of the gait cycle..... 22

Figure 2.12. Sagittal plane angular rotation of the lower limb joints during a gait cycle. (a) Hip motion; (b) Knee motion; (c) Ankle motion {Adapted from (Neumann, 2010)}. 24

Figure 3.1. Generic representation of a multibody system (Machado et al., 2012). 27

Figure 3.2. Components of a vector attached to a body in global and local systems of coordinates. 29

Figure 3.3. Locating point P_i relative to the body-fixed and global coordinate systems. 30

Figure 3.4. Revolute joint connecting bodies i and j (Flores & Lankarani, 2012). 32

Figure 3.5. Representation of a trajectory described by the CM of a free body.....	34
Figure 3.6. Flowchart of computational procedure for dynamic analysis of multibody systems based on the direct integration method {Adapted from (Flores et al., 2008)}.....	37
Figure 3.7. Open-loop (without the application of BSM) and closed-loop (with the application of BSM) control systems.....	39
Figure 4.1. ½ HAT-leg model representation.....	42
Figure 4.2. (a) Representation of the local reference frames on the ½ HAT-leg model; (b) Representation of the orientation of each segment with respect to the global coordinate system.....	44
Figure 4.3. Non-constant distances between anatomical points from frame-to-frame, during the digitalization process ($L_{k-2} \neq L_{k-1} \neq L_k$) {Adapted from (Tavares da Silva, 2003)}.....	47
Figure 4.4. Representation of the previous kinematic analysis of the system positions {Adapted from (Maireles, 2007)}.....	48
Figure 4.5. Filtering procedure using the Butterworth 2 nd order, low pass filter: (a) the raw signal; (b) the frequency response curve of the filter; (c) the filtered signal {Adapted from (Tavares da Silva, 2003)}.....	49
Figure 4.6. Representation of the gait cycle with the evolution of the GRF components over the stride period.....	51
Figure 4.7. (a) Components of GRF and its point of application; (b) The transferred forces and moments to the foot's CM.....	51
Figure 4.8. Interpolating curves of guiding data. The zone of accentuated curvature was zoomed in, in two of the graphs. The curves represent the trajectory described by the CM of the body 1 – (a) x -coordinate and (b) y -coordinate – and the variation of the orientation of the four bodies with time – (c) body 1, (d) body 2, (e) body 3, and (f) body 4.....	54
Figure 4.9. Interpolating curves of GRF data. The regions where an abrupt variation of the variable under analysis is noticed were zoomed in. (a) Longitudinal GRF evolution; (b) Vertical GRF evolution; (c) Evolution of x -coordinate of the point of application of the GRF; (d) Evolution of y -coordinate of the point of application of the GRF.....	55
Figure 4.10. Error of the angle of the body 4 obtained with ($\alpha = 5$; $\beta = 5$) and without constraints violation stabilization.....	58
Figure 4.11. Influence of the values of the Baumgarte parameters on the error of the position constraint equations. The graphs (a) to (f) show the variation of the position constraints associated with the revolute joints with time; The graphs (g) to (l) show the variation of the position constraints associated with the guidings with time.....	60

Figure 4.12. Influence of the values of the Baumgarte parameters on the error of the velocity constraint equations. The graphs (a) to (f) show the variation of the velocity constraints associated with the revolute joints with time; The graphs (g) to (l) show the variation of the velocity constraints associated with the guidings with time.	61
Figure 4.13. Initial position of the ½ HAT-leg model in the MATLAB simulation.	62
Figure 4.14. The gait cycle representation performed with the ½ HAT-leg model in MATLAB.	63
Figure 5.1. (a) Non-contact situation; $\delta > 0$; (b) Instant of the beginning or ending of contact; $\delta = 0$; (c) Contact situation, $\delta < 0$	67
Figure 5.2. Representation of the contact between two generic bodies.	68
Figure 5.3. (a) Components of contact forces and respective points of application; (b) The transferred forces and moments to the bodies' CM.	70
Figure 5.4. Leg-foot model representation.	74
Figure 5.5. Representation of the local reference frames on the leg-foot model in the initial position. ...	75
Figure 5.6. Joint resistance moment modeled using a system of nonlinear spring and damper.	77
Figure 5.7. Nonlinear behavior of the joint motion-limiting moment.	77
Figure 5.8. (a) Representation of the leg's frame ($\mathbf{v}_i, \mathbf{v}_{i_2}$) and the foot's vector (\mathbf{v}_j); (b) Vectors configuration in neutral position of the ankle; (c) Vectors configuration in plantarflexion of the ankle; (d) Vectors configuration in dorsiflexion of the ankle.	78
Figure 5.9. Representation of the contact geometry adopted in (a) the first approach (two points); and in (b) the second approach (two circles).	80
Figure 5.10. (a) Normal GRF for the circle located at the heel; (b) Normal GRF for the circle located at the MTP joints; (c) Total normal GRF registered for the foot; (d) Tangential GRF for the circle located at the heel; (e) Tangential GRF for the circle located at the MTP joints; (f) Total tangential GRF registered for the foot.	83
Figure 5.11. Initial position of the leg-foot model in the MATLAB simulation.	84
Figure 5.12. The simple leg motion representation performed with the leg-foot model in MATLAB.	85
Figure 5.13. ½ HAT-leg model representation in the initial position, and depiction of the local reference frames.	86
Figure 5.14. New reference frame created in the foot.	91
Figure 5.15. Initial guess: (a) Contact circles arrangement; (b) Comparison between the experimental and simulated normal contact force; (c) Comparison between the experimental and simulated tangential contact force; (d) Comparison between the experimental and simulated COP position.	93

Figure 5.16. Comparison between the experimental data and the results obtained from the optimization of the coefficient of friction, for (a) the normal contact force; (b) the tangential contact force; (c) the COP position. 102

List of Tables

Table 2.1. Range of motion of the human lower limb joints (Panero & Zelnik, 1979; Tavares da Silva, 2003).....	12
Table 4.1. Anthropometric data for the segments of the ½ HAT-leg model (Meyreles, 2007; Winter, 2009).....	43
Table 4.2. Body numbers i and j and local coordinates of the point P (Flores, 2010).....	45
Table 4.3. Guiding constraints input (Flores, 2010)	46
Table 4.4. Initial conditions of the positions and of the velocities for every rigid body in the system (Flores, 2010).....	47
Table 4.5. Initial velocities of the bodies after the correction	48
Table 4.6. Ground reaction force input (Flores, 2010)	50
Table 4.7. Simulation time for each interpolation method	56
Table 5.1. Mass and moment of inertia of each segment of the leg-foot model (Moreira, 2009).....	75
Table 5.2. Body numbers i and j and local coordinates of each revolute joint (point A)	75
Table 5.3. Initial conditions of the positions and of the velocities for every rigid body in the system	76
Table 5.4. Joint resistance data (Tavares da Silva, 2003; Tavares da Silva et al., 1997).....	79
Table 5.5. Contact parameters and local coordinates of contact points (P_1 and P_2) on the main foot part (body 2)	80
Table 5.6. Contact and geometric parameters of contact circles	82
Table 5.7. Contact parameters for the considered contact circles	87
Table 5.8. Number of circles, their arrangement, and the obtained results.....	88
Table 5.9. Contact parameters for the considered contact circles	91
Table 5.10. Initial guess and lower and upper limits of each parameter for optimization process.....	92
Table 5.11. Comparison between the results obtained from the optimizations performed with three different approaches for the definition of the objective function	95
Table 5.12. Comparison between the results obtained from the optimizations performed with different weights for each component	97
Table 5.13. Comparison between the results obtained from the optimizations performed with different weights for normal contact force	99

Table 5.14. Comparison between the results obtained from the optimizations performed with different number of circles.....	100
Table I.1. Results obtained from the optimizations performed with three different approaches for the definition of the objective function: simulation time, objective function value, optimal solution values, circles arrangement and deformation registered for each circle	115
Table I.2. Results obtained from the optimizations performed with different weights for each component: simulation time, objective function value, optimal solution values, circles arrangement and deformation registered for each circle.....	116
Table I.3. Results obtained from the optimizations performed with different weights for the normal contact force: simulation time, objective function value, optimal solution values, circles arrangement and deformation registered for each circle	117
Table I.4. Results obtained from the optimizations performed with different number of circles: simulation time, objective function value, optimal solution values, circles arrangement and deformation registered for each circle.....	119
Table I.5. Initial guess, lower and upper limits and results obtained from the optimization of the friction coefficient for each circle: simulation time, objective function value, optimal solution values, circles arrangement and deformation registered for each circle	120

List of Abbreviations and Acronyms

The general nomenclature used in the present work is listed below. Specific variables and parameters utilized only in a particular formulation are locally described.

2D	Two-dimensional
3D	Three-dimensional
BSM	Baumgarte stabilization method
c_r	Coefficient of restitution
CM	Center-of-mass
COP	Center-of-pressure
DAE	Differential algebraic equations
DIM	Direct integration method
DOF	Degrees-of-freedom
f_n	Normal contact force
f_t	Tangential contact force
f_x	Longitudinal ground reaction force
f_y	Vertical ground reaction force
\mathbf{g}	Generalized force vector
g	Gravitational acceleration
GRF	Ground reaction force
HAT	Head-arms-trunk
J	Objective function
k	Generalized contact stiffness
\mathbf{M}	Global mass matrix
m	Mass of a body, number of kinematic constraints
MBS	Multibody system
MTP	Metatarsophalangeal
n	Nonlinear exponent factor, number of cartesian coordinates
ODE	Ordinary differential equations
\mathbf{q}	Generalized coordinates vector

$\dot{\mathbf{q}}$	Generalized velocities vector
$\ddot{\mathbf{q}}$	Generalized acceleration vector
r	Circle radius
t	Time
$v_{0,n}$	Penetration velocity tolerance
$v_{0,t}$	Tolerance velocity to smooth friction transition
v_t	Tangential relative velocity
x, y	Global coordinates
α, β	Baumgarte stabilization parameters
γ	Right-hand side vector of accelerations constraint equations
δ	Relative penetration or deformation
$\dot{\delta}$	Relative normal contact velocity
$\delta^{(-)}$	Initial normal impact velocity
θ	Body orientation with respect to the global coordinate system
λ	Vector of Lagrange multipliers
μ	Friction coefficient
μ_c	Coulomb friction coefficient
μ_d	Viscous friction coefficient
\mathbf{v}	Right-hand side vector of velocities constraint equations
ξ, η	Local coordinates
Φ	Vector of kinematic constraints
$\Phi_{\mathbf{q}}$	Jacobian matrix of the constraint equations
ϕ	Constraint equations

Chapter 1 – Introduction

In this first chapter a general overview of the topics covered in the present dissertation is provided. First, the motivation inherent to the development of this work is addressed, followed by a clarification of the scope and objectives to be achieved during its course. In the third section, a literature review of the state-of-the-art of the field of investigation is provided, and in the subsequent section, the structure of this dissertation, including a brief description of the content covered in each chapter, is provided. Finally, the contributions that this work intends to provide are also stated.

1.1. Motivation

Biomechanics is an area of investigation that can be understood as the application of mechanical concepts to biological systems. In particular, Biomechanics of the Human Motion provides conceptual and mathematical tools essential for understanding how the human body moves, focusing on the analysis of forces and moments applied on the musculoskeletal system and their effects on the movement of the anatomical structures. In this context, the multibody systems (MBS) dynamics aims to study the characteristics of the motion of biomechanical systems and how the application of external and internal forces affects and restricts such movement (Knudson, 2007; Meireles, 2007).

According to Dunn et al. (2005), modeling is the process by which the principles of physics, chemistry, or biology are expressed in a mathematical formulation that characterizes the system or the phenomena under consideration, describing the behavior of the system and its interaction with its environment. The mathematical models are then solved by numerical methods through computational algorithms (Dunn et al., 2005).

Recently, the interest in studying the dynamics of human motion through the use of computational models has been increasing, due to the possible use of this method for quantitative prediction, quantitative hypothesis testing and the estimation of various dynamic variables which are challenging to measure experimentally, such as forces and moments transmitted by the joints. The analysis of the human motion, through computational simulations, allows to appraise a variety of different scenarios on a valid representation of the human system, while providing a cost-effective and less time-consuming approach, when compared with experimental procedures. The study of the human motion using MBS

formulations has experienced several developments in the past decades, which led to their successful application in the fields of rehabilitation, clinical, sports or equipment design (Rodrigues da Silva et al., 2021; Siegler et al., 1982).

The human movement simulation through computational methods requires the implementation of mathematical models that accurately describe the behavior of the human body and its interaction with the surrounding environment. From this perspective and taking into consideration the advances in the field of Biomechanics of the Human Motion and its practical application, it becomes necessary to formulate new computational methodologies that comprise strategies for modeling the interaction between the foot and the ground, considering realistic representations of the foot and appropriate numerical descriptions of its interaction with the ground. In this work, a 2D biomechanical model of human body is developed with the objective of studying the dynamics of the human gait and the behavior of the foot-ground interface.

1.2. Scope and Objectives

The purpose of this dissertation is to develop and implement a biomechanical multibody model to analyze the dynamic behavior of the human body and its interaction with the surrounding environment.

The first step will consist in the characterization of the biomechanical model, including its anatomical description, and determination of the geometrical and inertial aspects. The definition of the initial configuration of the system will also be taken as an important step in this phase. The model will be defined using the MBS formulation to study its motion in the sagittal plane. Therefore, the fundamental aspects associated with MBS dynamics must also be addressed, particularly the type of coordinates, constraints, and forces acting on the system.

The contact modeling will be considered and critically analyzed for introduction on the biomechanical model. The foot-ground interaction will be modeled and implemented, highlighting three main tasks that must be fulfilled – the geometry definition, the contact detection, and the resolution of the contact problem, applying appropriate constitutive laws in the normal and tangential directions. The initial focus will be the study of the foot-ground contact in a simulation of a simple leg motion, with the intention of validating the methodologies of contact geometry definition and contact detection. Then, the foot-ground contact model will be implemented in a simulation of the human gait and the obtained ground reaction forces will be compared to experimental data, in order to validate the entire methodology of foot-ground contact analysis.

The biomechanical model, the considered contact models and the dynamic analysis will be developed and implemented in a computational MATLAB code.

The specific goals of this work can be defined in the following points:

- To present a complete and updated literature review on the existing foot-ground contact modeling strategies for human motion analysis;
- To develop a biomechanical multibody model of the right side of the human body in MATLAB for dynamic analysis;
- To establish a computational foot-ground contact model;
- To incorporate the developed foot-ground contact model in the biomechanical model;
- To validate the proposed model.

The obtained model may be useful to simulate the biomechanics of the human gait in non-pathologic situations and may represent an instrument that helps to understand and identify gait abnormalities.

1.3. Literature Review

Over the last few decades, the development of accurate mathematical models of the human body has been one of the greatest challenges in the field of biomechanics. The implementation of mathematical models that correctly describe the behavior of the human body and its interaction with the surrounding environment is of high importance to understand and analyze human motion (Abu-Faraj et al., 2015; Tavares da Silva, 2003).

In the clinical field, the computer simulation of several human capabilities has revealed to be useful in pretreatment evaluation (Arnold & Delp, 2005), surgical decision (Delp et al., 1997), and postoperative assisting (Eschweiler et al., 2017; Li et al., 2018). It also represents an instrument to evaluate and improve the performance of elite athletes (Burgess et al., 2006; Raasch et al., 1997; Roemer, 2010) and enables the analysis and prevention of athletic injuries (Trasolini et al., 2022; Wan & Shan, 2016). The gait analysis also helps to understand more about orthopedic and neuromuscular disorders such as cerebral palsy, stroke and Parkinson disease (Arnold & Delp, 2005; Öunpuu et al., 1996; Winter, 1984). Additionally, other applications may include evaluation of prosthetic joint replacement (Andriacchi & Hurwitz, 1997; Pérez-González et al., 2008) and orthotic application (Brodke et al., 1989; Silva et al., 2010).

In this field of investigation, the dynamic analysis of the human gait usually involves the acquisition and reconstruction of trajectories from markers placed at specific locations on the human body. Typically, the motion capture is done through synchronized cameras and then, it is required to digitalize the anatomical points and reconstruct the movement. For the external forces' measurement, force plates synchronized with the cameras, are utilized. These devices provide the components of the ground reaction force (GRF) and the center-of-pressure (COP), i.e., the point in the platform, in which the resultant of the forces is applied (Abu-Faraj et al., 2015).

1.3.1. Evolution of the Human Gait Analysis

The primary studies of human gait remount from the 17th century and were based on simple visual observation. Giovanni Borelli (1608-1679), in his work *De Motu Animalium*, employed a geometric method to analyze complex movements, such as locomotion, running, and jumping. This 17th century scientist was recognized by one of the first descriptions of the distinct phases of the gait cycle and the action of muscles during walking. Therefore, Borelli is recognized as the “Father of Biomechanics” (Abu-Faraj et al., 2015; Baker, 2007).

In the first half of the 19th century, Wilhelm (1804–1891) and Eduard (1806–1871) Weber developed methods for the quantitative measurement of locomotion using observations of the stance and swing phases of the gait cycle. In 1836, these scientists registered the position of the trunk and lower limbs at fourteen different instants in the gait cycle and created illustrations of the body structure during locomotion. They also postulated the pendulum theory of gait, which suggested that the swinging limb acts as a pendulum attached to the hip and the swing phase of the gait is a purely passive movement, where the swing limb advanced just through gravitational force, not being required muscular activity. This hypothesis was invalidated by Guillaume Duchenne (1806-1875), who demonstrated that paralytic patients could not advance the swinging limb, due to the absence of thigh flexors (Abu-Faraj et al., 2015; Baker, 2007).

Étienne Marey (1830-1904) transformed the study of locomotion from a mere qualified observation to a quantified scientific analysis. This scientist implemented the first Biomechanics laboratory, and invented numerous motion capture machines, including a force platform (Abu-Faraj et al., 2015).

More recently, David Winter (1930-2012) refined experimental techniques for the gait analysis and presented fundamental concepts to the study of human locomotion, among which are automated motion capture and the powers produced by joint moments of force (Abu-Faraj et al., 2015).

1.3.2. Foot-Ground Contact Modeling Strategies

As mentioned previously, the human gait analysis requires the experimental evaluation of the GRF in order to provide a complete and accurate description of the human performance. However, the measurement and data acquisition of the GRF are constrained in the number of human steps, since the experimental apparatus and platforms have limited lengths. With the purpose of overcoming this drawback, several formulations to mimic the human foot-ground interaction have been proposed in the literature, which provide numerical approaches to calculate the GRF without the need of any experimental measurement (Moreira et al., 2009; Van Hulle et al., 2020).

The application of foot-ground contact modeling strategies for human motion analysis reveals usefulness in several fields, namely for studying the biomechanical response of human motion for both healthy and pathological cases, or in the presence of orthotic and prosthetic devices. Moreover, the modeling and implementation of computational strategies for the contact mechanics of the foot-ground interaction also plays an important role in humanoid robots (Gonçalves et al., 2022; Xie et al., 2022), walking machines (Coelho et al., 2021; Safartoobi et al., 2021; Taheri & Zhao, 2020), among other mobile MBS.

Regardless of the high number of research works on the foot-ground contact interaction in the context of biomechanics of human motion, it is of paramount importance to have a comprehensive review on the available approaches to allow the comparison of their similarities and differences. This has been the main motivation for preparing a review article, entitled “A review on foot-ground contact modeling strategies for human motion analysis” (Saraiva et al., 2022), which evidences a detailed analysis, discussion and summary of the key features and main limitations of the computational strategies to mimic the foot and ground contact interaction in the human locomotion available in the literature.

The search approach adopted in the review was carried out on the electronic databases PubMed, Web of Science and Scopus to identify publications focusing on foot-ground contact modeling strategies. As the consequence of a critical reading of those publications, some additional papers were identified and included in the review. A total of 30 papers were analyzed, in which different contact geometries were established with the goal of defining the foot and ground surfaces. Points, circles, ellipses, spheres, ellipsoids, rectangular contact elements and surfaces obtained from 3D scanning procedures were found to be the most common types of contact geometries considered. Figure 1.1 depicts the number of studies organized according to the contact geometry considered in their analyses.

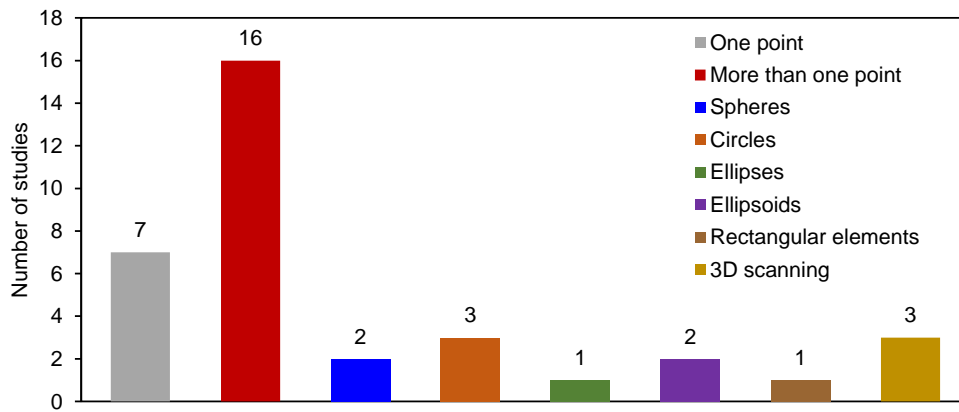


Figure 1.1. Number of studies organized according to the contact geometry considered in the foot-ground interaction model.

Regarding the resolution of the foot-ground interaction, the formulations based on contact force approaches (adopted by more than 75% of the studies) were preferred to the methods based on geometrical constraints. Furthermore, one of the main limitations reported in the analyzed papers dealt with the restriction of the motion to the sagittal plane. Overall, it was observed that a standard and general procedure to formulate the human foot-ground contact is still lacking, and, in this sense, future investigation should be conducted to report the parameters and the numerical aspects of the foot-ground model in a clear manner. To better understand the analysis and comparison of the studies included in the revision, the interested reader is referred to the published article (Saraiva et al., 2022).

1.4. Structure of the Dissertation

The present dissertation is structured in six main chapters, including this as a first chapter, in which the motivation, as well as the scope and objectives of this work are described. In addition, a literature review centered on the foot-ground contact modeling approaches is provided and the contributions of the work are stated.

The following chapter introduces the characterization of the human lower limb, starting by covering some biomechanical aspects, with the aim of establishing the terminology associated with the human movement, focusing, in particular, on the movements of the lower limb in the sagittal plane. Furthermore, a brief description of that structure anatomy is presented, and the depiction of the normal gait cycle is addressed, focusing on its main parameters and determinants.

The third chapter introduces the main fundamentals of the formulation for the dynamic analysis of multibody systems. Therefore, the concept of MBS, the explanation of the cartesian coordinates, the

formulation of the revolute joints and the guiding constraints, the establishment of the equations of motion, and how to advance the analysis in time are reviewed, as well as the Baumgarte Stabilization Method, for minimization of the integration errors. Essentially, the aim of this chapter is to provide the reader with a complete overview of the formulations implemented for dynamic analysis, which follow closely the work of Nikravesh (1988) and are the supporting structure for all the methodologies presented in the forthcoming chapters.

Chapter four fully describes the two-dimensional biomechanical multibody model of the right side of the human body developed, namely the geometric description of the rigid bodies, the connection between bodies by ideal revolute joints, the guidings that prescribe the gait motion, and the introduction of the GRF. The constraint equations are also explicitly presented. The utilized biomechanical model was implemented in a computational program developed in MATLAB, and the processes involved are described in this chapter too. At this point, the main results arising from the performed dynamic analysis are presented and discussed.

In Chapter five, the main aspects related to the modeling and simulation of contact problems, in the context of MBS, are presented, and two examples of application concerning the foot-ground interaction, are described in detail, analyzed, and discussed. The fundamental aspects of a generic problem of contact mechanics are approached, and the methodologies that deal with contact detection and contact resolution are introduced. Two application examples are shown, in which the foot-ground interaction is studied. First, a simple leg motion is simulated with the intention of validating the methodologies of contact geometry definition and contact detection. This simulation consists of a simple drop test in which the motion of the model is generated only by the action of the gravitational force. Lastly, in order to validate the entire methodology of foot-ground contact analysis, a second application example is presented, for the study of the interaction between the foot and the level ground during human gait. With the purpose of correctly determining the contact forces, an optimization process is implemented to obtain the most suitable values for the geometric and contact parameters of the proposed model, and the results obtained from computational and experimental analyses are compared using a multibody model of the right side of the human body, with the aim of validating the proposed approach.

Finally, in the sixth Chapter, the final comments of this dissertation are stated and recommendations for future developments are given.

1.5. Contributions of the Work

This dissertation provides contributions in the area of biomechanics of human motion, in particular with regard to the foot-ground contact interaction. It provides a complete and updated literature review on the existing foot-ground contact modeling strategies for human motion analysis, gathering the available approaches, to allow a comparison of their similarities and differences. This comprehensive review comprises a detailed analysis, discussion and summary of the key features and main limitations of the computational strategies to mimic the foot and ground contact interaction in the human locomotion available in the literature.

Furthermore, a two-dimensional biomechanical multibody model of the right side of the human body was developed in MATLAB for dynamic analysis, and a computational foot-ground contact model was established. Hence, this dissertation also provides contributions in the area of biomechanical computer simulation, concerning the application of a biomechanical model in the study of the human gait and in the analysis of the interaction between the foot and the ground. The obtained model may be useful to simulate the biomechanics of the human gait for non-pathologic situations, in the sagittal plane, and may represent an instrument that helps to understand and identify gait abnormalities.

Below, a list of the publications that comprise outputs from this investigation is presented:

1. **Saraiva, L.**, Rodrigues da Silva, M., Marques, F., Tavares da Silva, M., & Flores, P. (2022). A review on foot-ground contact modeling strategies for human motion analysis. *Mechanism and Machine Theory*, 177, 105046. <https://doi.org/10.1016/j.mechmachtheory.2022.105046>
2. **Saraiva, L.**, Rodrigues da Silva, M., Marques, F., Tavares da Silva, M., & Flores, P. (2022, December 5-6). A foot-ground contact model for human motion analysis [Abstract]. *DSM2022 - 2ª Conferência Nacional de Dinâmica de Sistemas Multicorpo*, Guimarães, Portugal (accepted for oral presentation).
3. **Saraiva, L.**, Rodrigues da Silva, M., Marques, F., Tavares da Silva, M., & Flores, P. (2022, December 5-6). Current perspectives on the modeling of the foot-ground interaction for human motion analysis [Abstract]. *DSM2022 - 2ª Conferência Nacional de Dinâmica de Sistemas Multicorpo*, Guimarães, Portugal (accepted for presentation in poster format).

Chapter 2 – Characterization of the Human Lower Limb

In the present chapter, a characterization of the human lower limb is presented. The lower limb may be defined as the part of the human body that includes the thigh, the leg, and the foot, comprising three principal joints, namely the hip, the knee and the ankle. The structure of the lower limb is specialized for support of the body's weight, locomotion, and maintenance of body stability (Standring, 2016).

The chapter starts by covering some biomechanical aspects, with the objective of establishing the terminology associated with the human movement, focusing, in particular, on the movements of the lower limb in the sagittal plane. Moreover, the range of motion of lower limb joints is addressed.

Furthermore, a brief description of that structure anatomy is presented, specifically with regard to bones, joints, and muscles. At this stage, it is important to emphasize the foot segment as a crucial structure in the biomechanical function of the human lower extremity. The foot is a complex multiarticular structure that supports the weight of the complete human body and is the only part of the body that is continuously acting on an external surface (Moreira, 2009).

Then, the depiction of the normal gait cycle is addressed, focusing on its main parameters and determinants. The magnitude of movement, in terms of angular rotation, of the main lower limb joints for a normal gait cycle is also covered.

Lastly, a summary of these aspects is presented.

2.1. Biomechanical Considerations

The human motion analysis and its description require the use of specialized terminology, to accurately and unequivocally describe different postures, movement types and position relations between the anatomical segments of the human body. Preceding the description of the biomechanics of the human lower extremity, the anatomical reference planes need to be presented (Figure 2.1). There are three established planes, perpendicular to each other. Each plane divides the human body into two halves of equal mass, and the point that specifies the intersection between these three planes is the center-of-mass (CM) of the body. These planes are extremely useful to describe large amplitude movements and to define specific terminology of the types of movements of the human body (Hall, 2012; Muscolino, 2017; Winter, 2009).

The sagittal plane is a vertical plane that divides the body into right and left parts. The frontal plane, also called coronal plane, is a vertical plane that divides the body into anterior and posterior parts. The transverse plane, or axial plane, is a horizontal plane cutting through the body at right angles to the sagittal and frontal planes, dividing the body in lower and upper halves. The vertical direction (superior–inferior) is y , the direction of progression (anterior–posterior) is x , and the sideways direction (medial–lateral) is denoted as z (Muscolino, 2017; Winter, 2009).

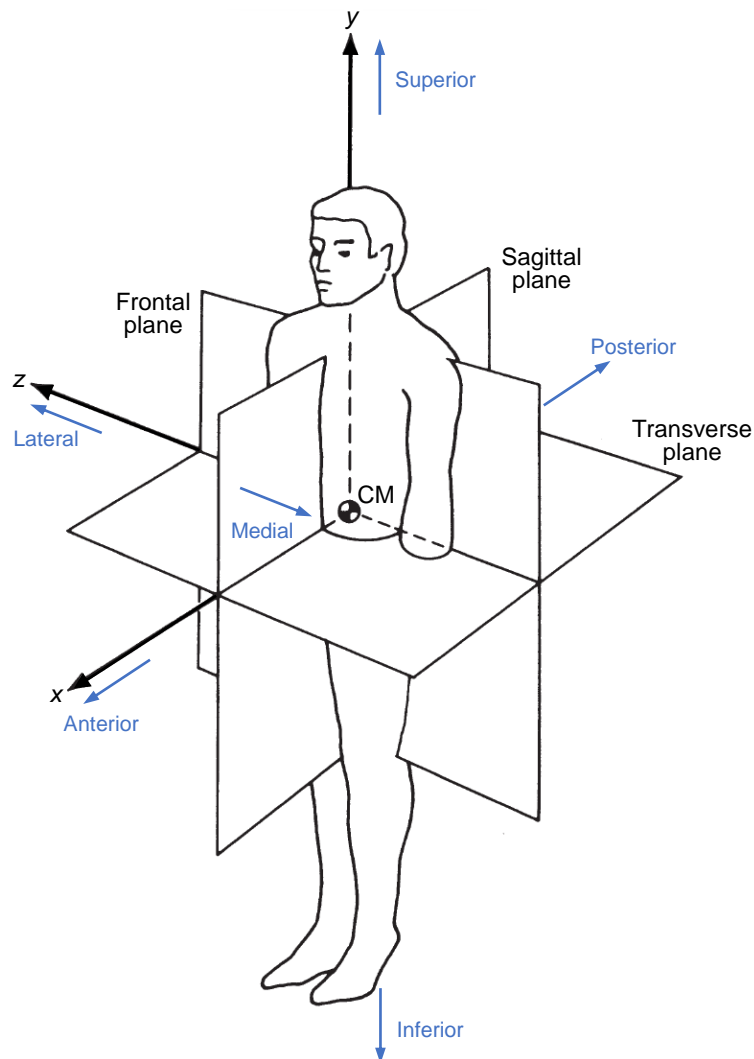


Figure 2.1. Anatomical reference planes and spatial coordinate system {Adapted from (Winter, 2009)}.

The description of the relative positioning of various points or structures of the human body is performed in relation to the anatomical reference position, with the objective to perform a clear and consistent characterization. The anatomical reference position is defined by the human body standing

erect and facing forward with the arms at the sides and the legs parallel to one another. The palms are facing forward, and the fingers and toes are extended (Hall, 2012; Muscolino, 2017).

When the human body is arranged in the anatomical reference position, all body segments are assumed to be positioned at zero degrees, and the rotation of any segment is measured as the angle established between the body segment's actual position and the anatomical reference one (Hall, 2012).

The human lower limb motion is more commonly analyzed in the sagittal plane, since joints present in the human lower limb exhibit motion primarily in this plane (Oatis, 2009). The main movements occurring in the sagittal plane are designated as flexion and extension, which represent the movements that involve a rotation in this plane. Focusing on the lower limb, the hip flexion is the anterior movement of the thigh within the sagittal plane, while the extension is the posterior movement of this segment. From the knee joint and further distally, flexion of a body part moves posteriorly. Therefore, extension is the anterior movement of a segment. For the foot segment, other terms are used – dorsiflexion for the extension movement and plantarflexion for the flexion. Dorsiflexion occurs when the foot moves superiorly, in the direction of its dorsal surface, and plantarflexion is when it moves inferiorly, in the direction of its plantar surface. These movements are depicted in the Figure 2.2 (Muscolino, 2017).

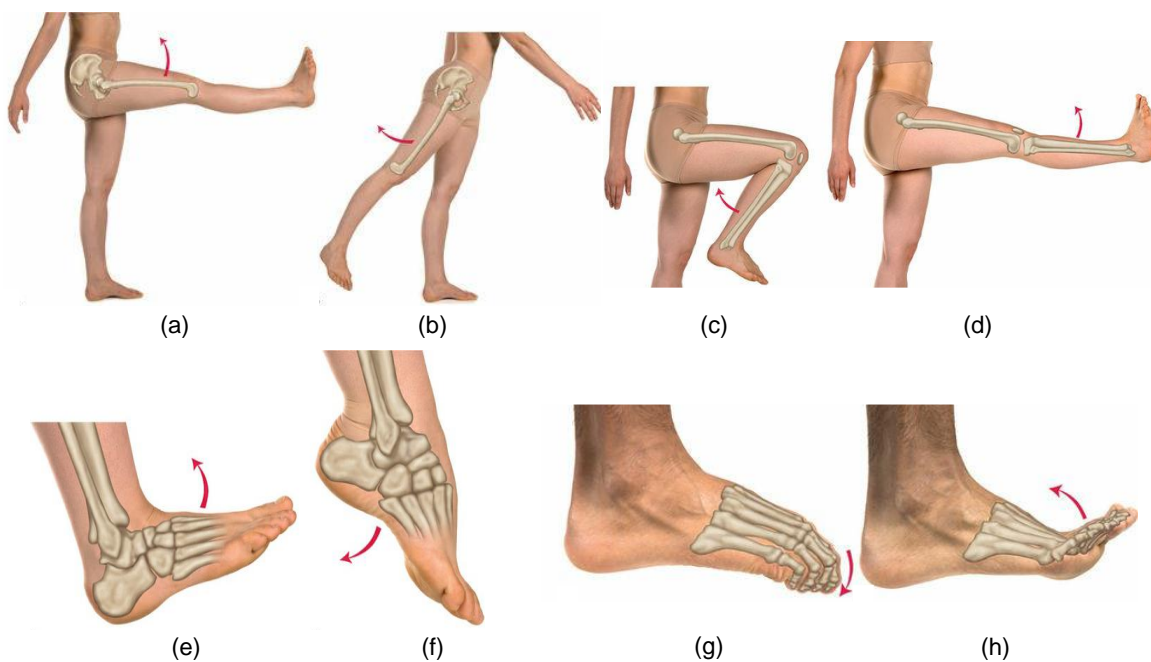


Figure 2.2. (a) Hip flexion; (b) Hip extension; (c) Knee flexion; (d) Knee extension; (e) Dorsiflexion of the foot; (f) Plantarflexion of the foot; (g) Flexion of the toes; (h) Extension of the toes {Adapted from (Muscolino, 2017)}.

These movements are restricted by the limits imposed by the joints. Joint range of motion refers to the extent of osteo-kinematic motion allowed by a joint, when performing a movement with or without assistance (Abu El Kasem et al., 2020). The measurement of the angles that establish the complete spectrum of joint motion is complex and varies according to the measurement techniques, the conditions under which the data are obtained, and the particular aspects of the subject, such as the age, sex, body geometry or the clothes and footwear being used (Panero & Zelnik, 1979; Tavares da Silva, 2003). In Table 2.1, the description and representation of the range of motion of the most relevant joints of the human lower limb are presented.

Table 2.1. Range of motion of the human lower limb joints (Panero & Zelnik, 1979; Tavares da Silva, 2003)

Joint name	Motion name	Joint range of motion
Hip	Flexion / extension	
Knee	Flexion	
Ankle	Dorsiflexion / plantarflexion	
Metatarsophalangeal joint	Flexion / extension	

2.2. Basic Anatomy

The musculoskeletal system is responsible for the body movement, shape, stability, and support and consists of the specialized connective tissues of the articulated bony skeleton and the skeletal muscles that act across the articulations. The combined action of the muscles, with bones and articulations, allows the normal locomotion of the human body (Standring, 2016).

The human skeleton not only has the function of supporting the body, but it also provides attachment points for the muscles that move it and constitutes a protective structure for internal tissues and organs (Betts et al., 2017).

The lower limb contains 30 bones, namely the femur, patella, tibia, fibula, tarsal bones, metatarsal bones, and phalanges, as seen in Figure 2.3. The femur is the main bone present in the thigh, the patella articulates with the distal end of the femur, the tibia is the larger bone located on the medial side of the leg, and the fibula is the thin bone present on the lateral side of the leg. The bones of the foot are divided into three groups – tarsal bones, metatarsal bones, and phalanges (Betts et al., 2017).

The tarsal bones are located on the posterior portion of the foot and comprise a group of seven bones, the talus, calcaneus, cuboid, navicular and three cuneiform bones, named the first, second, and third cuneiforms. The metatarsal bones are five elongated bones, numbered I to V from the medial to lateral position. The toes contain 14 small bones, the phalanges. The great toe has two phalanges – proximal and distal – and the other four toes have three phalanges each – proximal, middle, and distal (Oatis, 2009; Tortora & Derrickson, 2010).

The foot can also be described by three functional units, the hindfoot, midfoot, and forefoot. The hindfoot, also called rearfoot, consists of the talus and calcaneus, and the remaining tarsal bones compose the midfoot. The forefoot comprises the metatarsal bones and the phalanges (Neumann, 2010; Oatis, 2009).

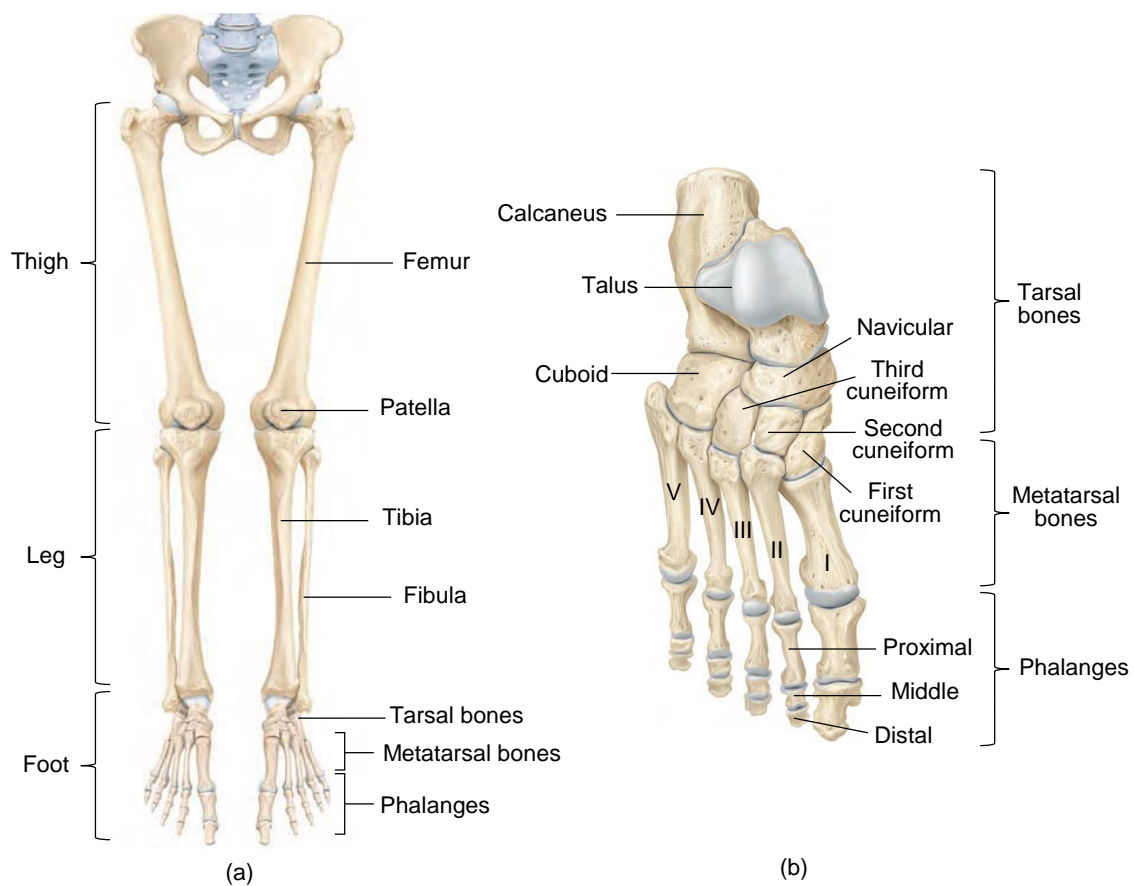


Figure 2.3. (a) Anterior view of the bones of the lower limb; (b) Superior view of the bones of the foot (Adapted from (Tortora & Derrickson, 2010)).

Although the bones can be considered perfectly rigid, they are articulated by joints that give the human body a huge flexibility. Joints are formed where two or more bones come together, and their main functions are, on the one hand, to allow or inhibit relative movement in a given direction and, on the other hand, to transmit forces between the bones through the muscles (Betts et al., 2017).

The major joints of the lower limb are the hip, the knee and the ankle. The hip joint is a synovial ball-and-socket joint, where the head of the femur (ball) articulates with the acetabulum present in the pelvic girdle (socket), as seen in Figure 2.4. This type of articulation allows motion in the three planes, which makes the femur capable of moving in both anterior-posterior and medial-lateral directions and of rotating around its long axis (Betts et al., 2017; Standring, 2016).

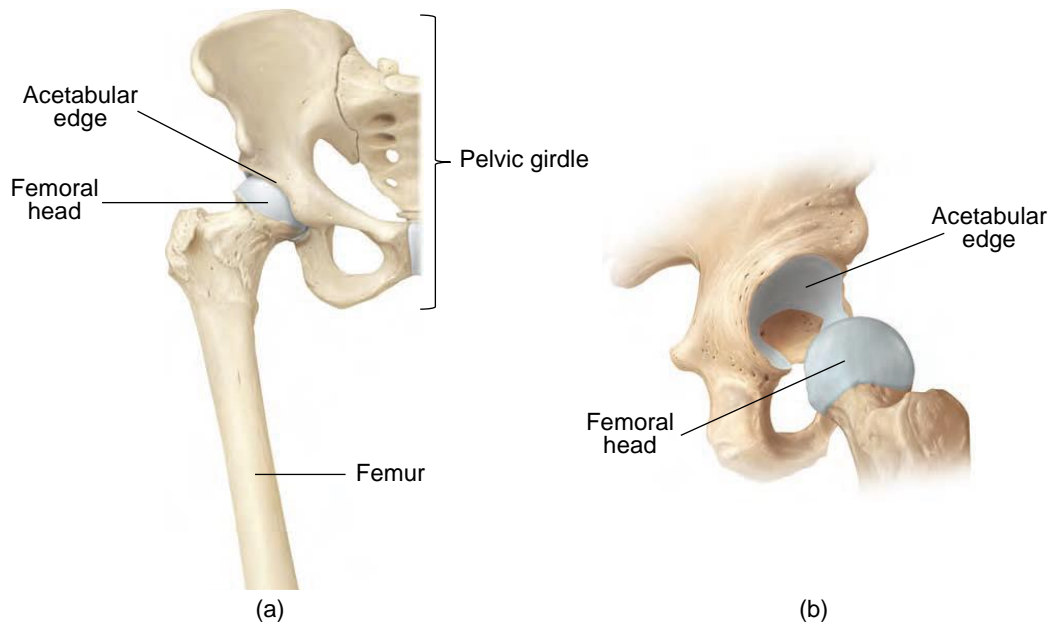


Figure 2.4. (a) Anterior view of the hip joint; (b) Detail of the hip joint {Adapted from (Tortora & Derrickson, 2010)}.

The knee joint is located between the femur, tibia and fibula and is, actually, a structure composed of three joints, the patellofemoral, the tibiofemoral and the superior tibiofibular joints (Figure 2.5). The patellofemoral joint is located between the articular side of the patella and the distal femur. During the normal walking process, as the knee flexes and extends, a gliding motion occurs between the articular surfaces of the patella and the femur. The tibiofemoral joint consists of the articulations between the condyles of the tibia, that are small and nearly flat, and the femoral condyles, which are convex and have a large articular surface area, allowing extensive knee motion in the sagittal plane. The superior tibiofibular joint is a plane synovial joint and allows just minor gliding movements (Betts et al., 2017; Neumann, 2010; Standring, 2016).

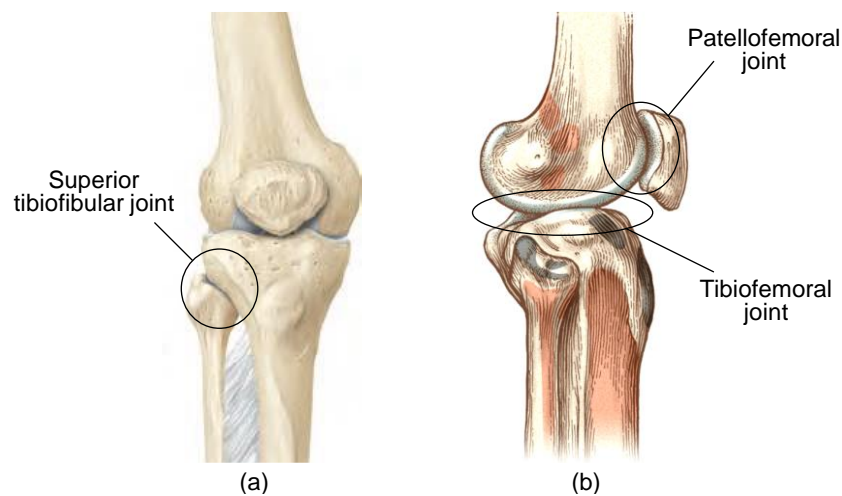


Figure 2.5. Three-joint structure of the knee. (a) Anterior view; (b) Lateral view {Adapted from (Neumann, 2010; Tortora & Derrickson, 2010)}.

The human foot comprises a total of 31 joints. The ankle (talocrural) joint is a hinge joint established between the talus and the distal ends of the tibia and fibula. This joint allows only dorsiflexion and plantarflexion of the foot. The articulations located between the tarsal bones are plane synovial joints, and all the small movements that occur at these joints contribute to the inversion and eversion foot motions, in the frontal plane. The most significant of these articulations is the subtalar joint, situated between the talus and calcaneus bones. Among the other joints of the foot, can be highlighted the metatarsophalangeal (MTP) articulations, which are ovoid or ellipsoid joints between the metatarsal heads and the proximal phalangeal bases. Collectively, all foot joints make possible the complex movements required for the normal daily activities, such as stabilization in standing, shock absorption and propulsion in gait (Betts et al., 2017; Neumann, 2010; Standring, 2016). In Figure 2.6, the joints present in the foot are depicted.

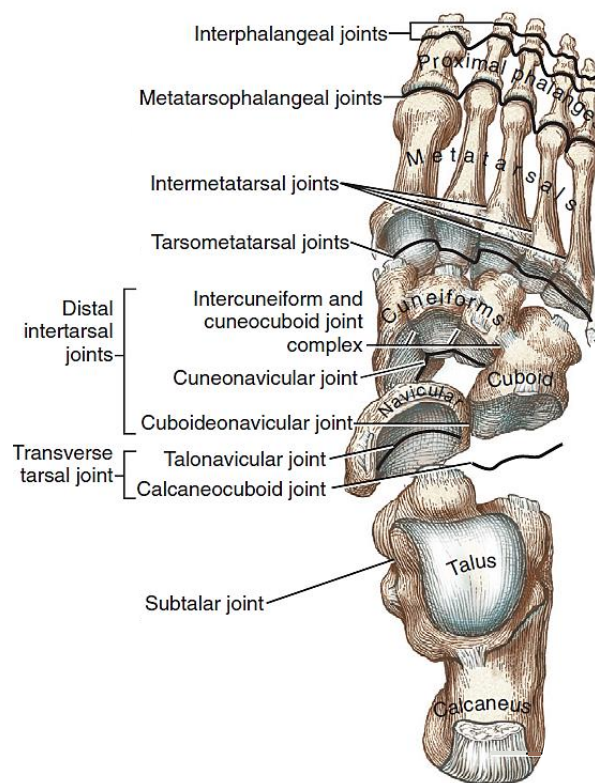


Figure 2.6. Joints of the foot {Adapted from (Betts et al., 2017)}.

The lower limb comprises many muscles that act on more than one joint, which usually causes the joints to move collectively rather than in isolation. The muscles of the lower limb are important in the maintenance of equilibrium during locomotion and in stance. Furthermore, they have the function of contracting and producing body movements (Standring, 2016; Tortora & Derrickson, 2010).

To be able to generate these movements, the configuration of the muscles and the way they act around the joints are very important. The main muscles that are responsible for the flexion and extension movements of the main joints of the lower limb in the sagittal plane are illustrated in Figure 2.7 to Figure 2.10.

The muscles that act across a joint may be classified in primary or secondary muscles, based on their actions. The primary muscles are the ones that effectively produce the movement the body is performing, while the secondary muscles have the function of assisting the primary muscles to achieve the produced motion and ensure stability and efficiency for the primary muscles (Neumann, 2010). The primary hip flexors (Figure 2.7 (a)) are the psoas major, iliacus, sartorius, tensor fasciae latae, rectus femoris, adductor longus, and pectineus. Secondary hip flexors are the adductor brevis, gracilis, and anterior fibers of the gluteus medius and of the gluteus minimus. The primary hip extensors (Figure 2.7 (b)) are the gluteus maximus, the long head of the biceps femoris, the semitendinosus, the semimembranosus, and the posterior fibers of the adductor magnus. The anterior fibers of the adductor magnus and the posterior fibers of the gluteus medius and of the gluteus minimus are secondary extensors (Muscolino, 2017; Neumann, 2010).

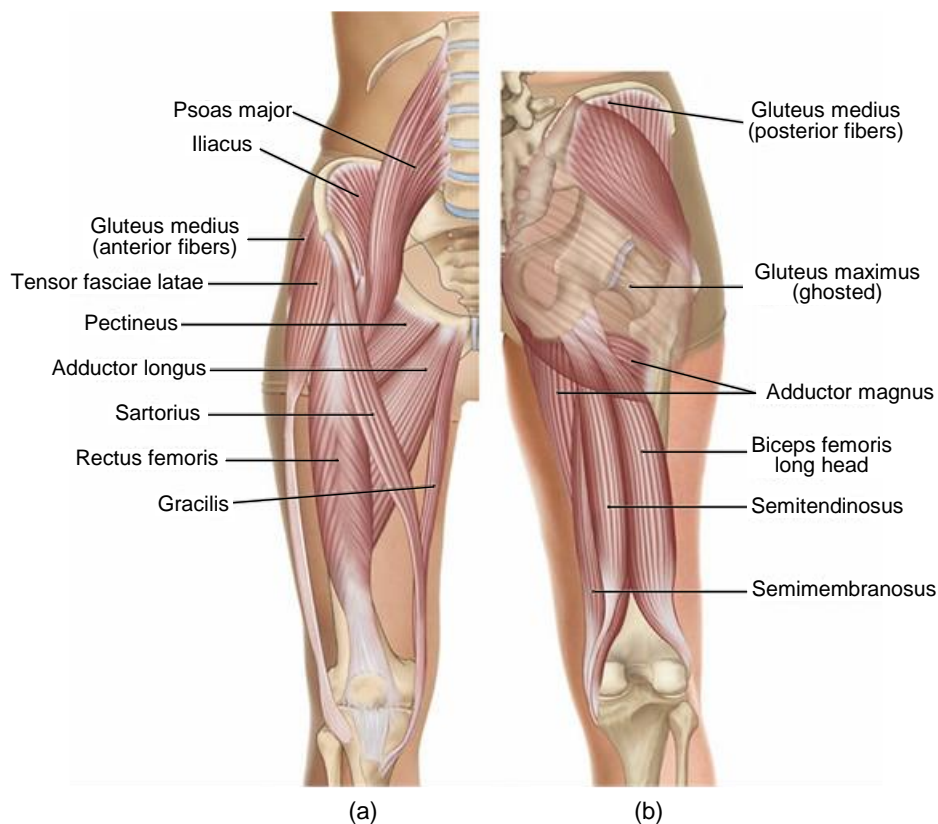


Figure 2.7. (a) Anterior view of the hip joint flexors; (b) Posterior view of the hip joint extensors (the adductor brevis and gluteus minimus are not represented) {Adapted from (Muscolino, 2017)}.

The muscles that are responsible for knee flexion (Figure 2.8 (a)) are the semitendinosus, semimembranosus, biceps femoris, sartorius, gracilis, popliteus, gastrocnemius, and plantaris. The rectus femoris, vastus lateralis, vastus medialis, vastus intermedius, tensor fasciae latae and gluteus maximus are knee extensors (Figure 2.8 (b)) (Muscolino, 2017; Neumann, 2010).

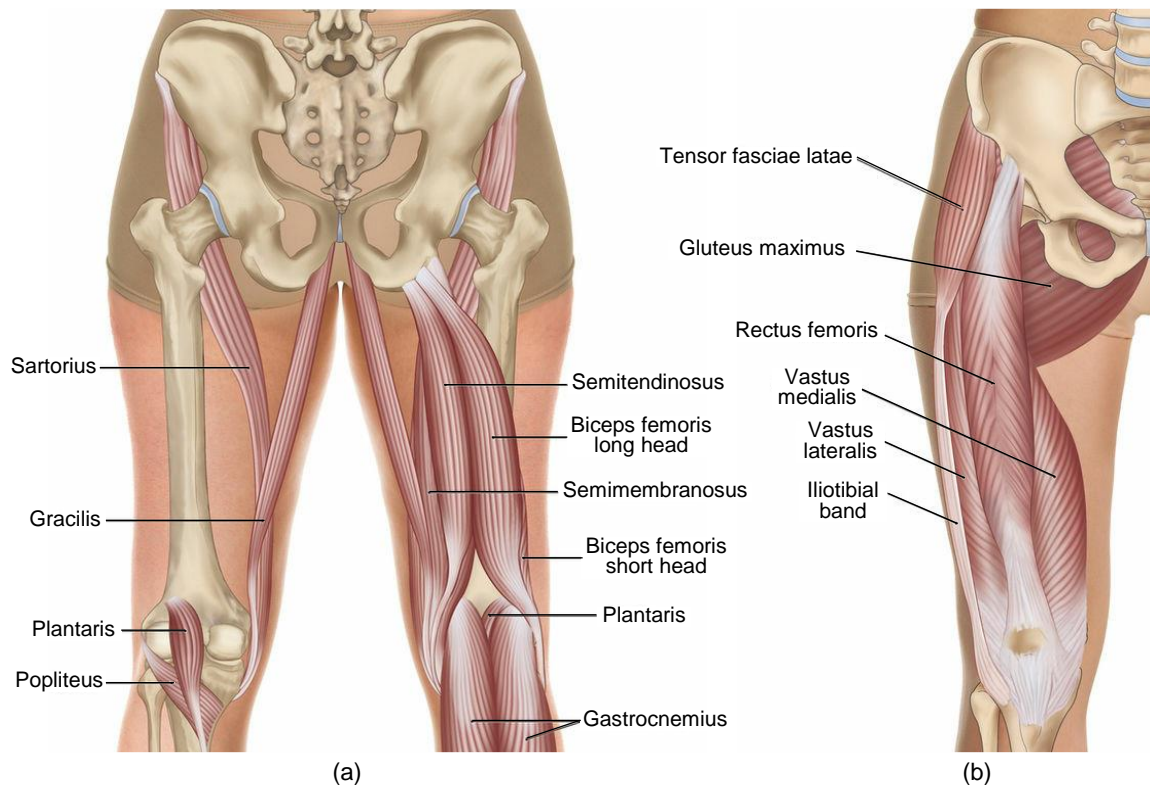


Figure 2.8. (a) Posterior view of the knee joint flexors; (b) Anterior view of the knee joint extensors (the vastus intermedius is not represented) {Adapted from (Muscolino, 2017)}.

The ankle joint dorsiflexors (Figure 2.9 (a)) are the tibialis anterior, extensor digitorum longus, fibularis tertius and extensor hallucis longus. Gastrocnemius, soleus, plantaris, tibialis posterior, flexor digitorum longus, flexor hallucis longus, fibularis longus and fibularis brevis are responsible for plantarflexion movements (Figure 2.9 (b)) (Muscolino, 2017).

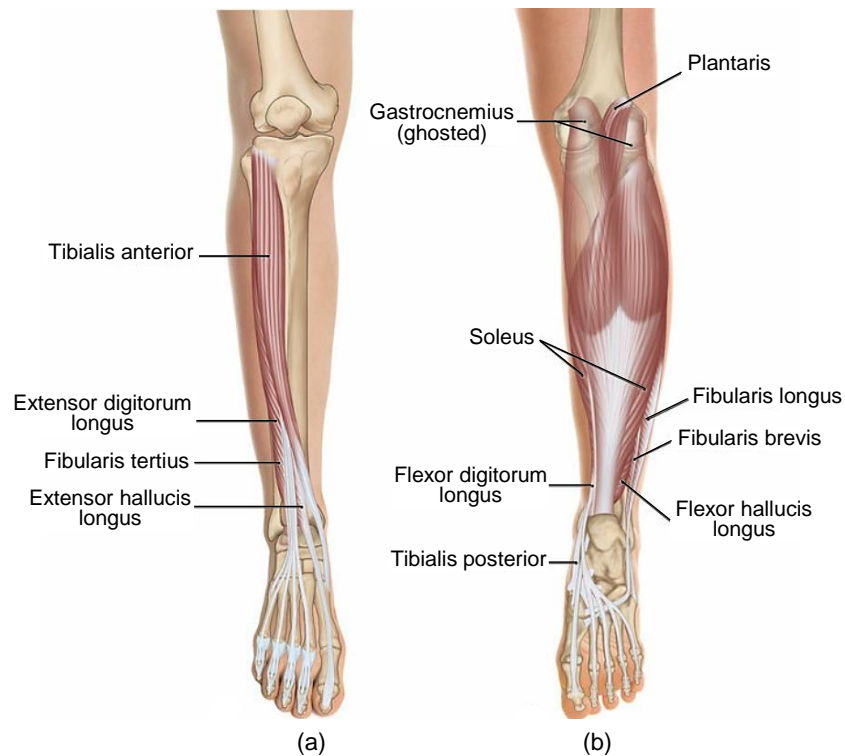


Figure 2.9. (a) Anterior view of the ankle joint dorsiflexors; (b) Posterior view of the ankle joint plantarflexors {Adapted from (Muscolino, 2017)}.

In the foot, the muscles that are responsible for the metatarsophalangeal joint flexion in the great toe (Figure 2.10 (a)) are the flexor hallucis longus, flexor hallucis brevis, adductor hallucis and abductor hallucis. For the remaining four toes (Figure 2.10 (b)), the MTP flexor muscles are the flexor digitorum longus, flexor digitorum brevis, quadratus plantae, flexor digiti minimi pedis, abductor digiti minimi pedis, lumbricals pedis, plantar interossei and dorsal interossei pedis. Concerning the great toe extensors (Figure 2.10 (c)), there are the extensor hallucis longus and extensor hallucis brevis, and for the toes two through five (Figure 2.10 (d)), the extensor digitorum longus, extensor digitorum brevis, dorsal interossei pedis, lumbricals pedis and plantar interossei are the muscles responsible for the MTP extension (Muscolino, 2017).

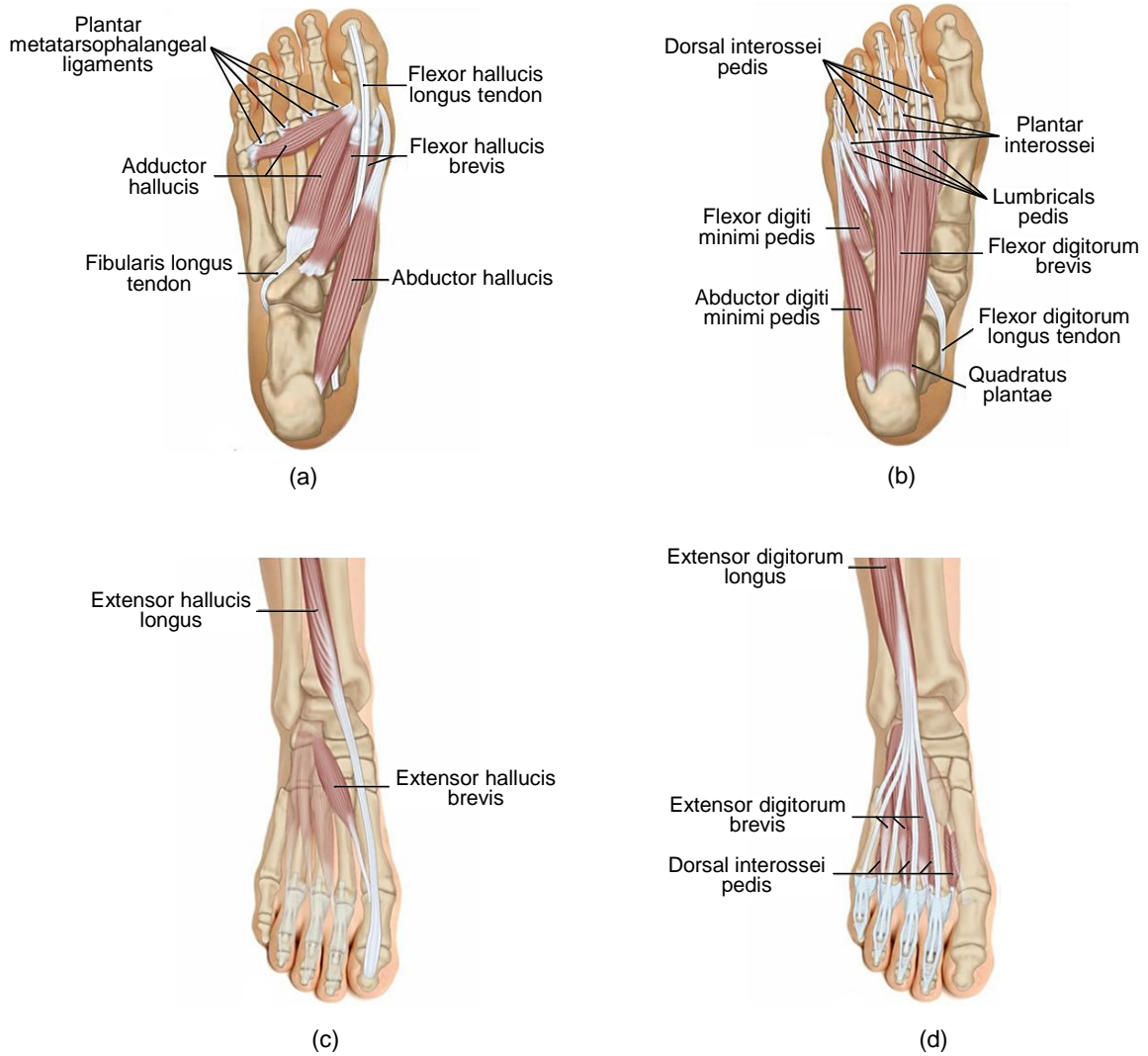


Figure 2.10. (a) Plantar view of the flexors of the big toe; (b) Plantar view of the flexors of toes two through five; (c) Dorsal view of the extensors of the big toe; (d) Dorsal view of the extensors of toes two through five {Adapted from (Muscolino, 2017)}.

The muscles represent one of the main sources of internal forces that influence the biomechanics of movement. Ligaments, tendons, articular capsules, and bone components help to resist, transmit and absorb these internal forces (Meireles, 2007).

It is important to emphasize the foot segment, which plays an important role in the biomechanical function of the lower extremity, providing support and balance during standing, and stabilizing the body during walking. Furthermore, it supports the weight of the complete human body (Moreira, 2009). The muscles present in the ankle and the foot have the function of controlling the actions of the underlying joints, and provide the stability and shock absorption necessary in gait (Neumann, 2010).

2.3. Gait Characterization

The normal gait is a periodic and rhythmic process that promotes a progressive translation of all body, and is characterized by alternated movements of propulsion and retropropulsion, produced by coordinated rotational movements of body segments. These movements guarantee both motion and support to the body, since at least one foot is always in contact with the ground. As the movement occurs, the support of the body is provided by one limb, while the other limb advances itself to a new support site. Then the limbs reverse their roles. For body weight transferring from one limb to the other, both feet are in contact with the ground. These events are repeated by each limb until the person's destination is reached. The gait cycle is considered as a single sequence of these functions by one limb, corresponding to the period between two identical events in the walking process, i.e., from the initial contact of one foot, to the following initial contact of the same foot (Neumann, 2010; Perry, 1992).

The cycle of the human locomotion is divided into two periods for each foot, the stance and swing phases. The stance phase comprises about 58 to 61% of the gait cycle and represents the time when the foot is in contact with the ground. The swing period corresponds to the remaining 39 to 42% of the gait cycle and constitutes the time when the foot is no longer in contact with the ground. The period in which both feet are in contact with the ground is called double-limb support and occurs at the beginning and the end of the stance phase, representing nearly 16 to 22% of the gait cycle. If the locomotion velocity increases, double-limb support time decreases, which makes the running activity a movement without double-limb support (Lakany, 2008; Meireles, 2007).

Considering the initial contact of the right foot with the ground, as the starting and completing event, the gait cycle can be described as the following sequence of events: initial contact, loading response, midstance, terminal stance, preswing, initial swing, midswing and terminal swing. The first five phases correspond to the stance period, and the swing period is constituted by the remaining three ones (Perry, 1992). These phases are briefly described below and are illustrated in Figure 2.11.

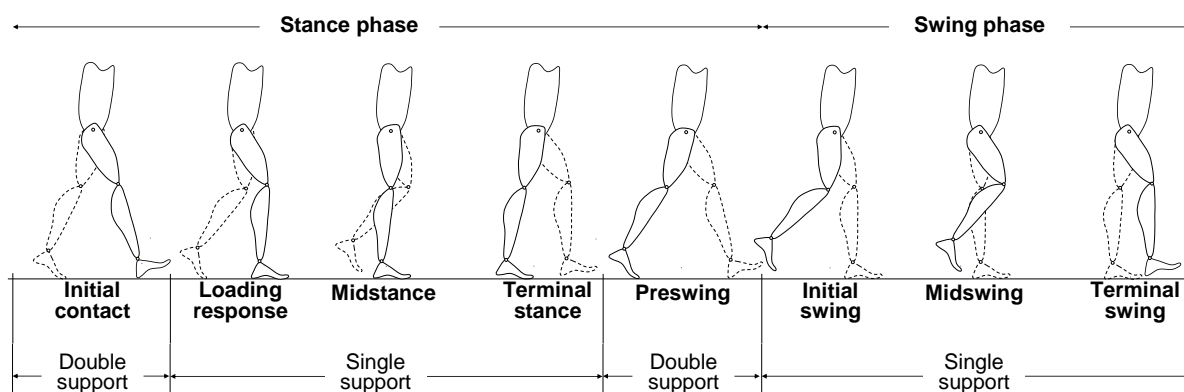


Figure 2.11. Phases of the gait cycle.

Stance Phase

1. *Initial Contact* corresponds to the instant in which the right foot touches the ground. Typically, this initial contact is made by the heel, and it is called *heel contact*.
2. *Loading Response* takes place immediately after the initial contact and comprises 10% of the gait cycle. During this phase, the right foot comes fully in contact with the floor, and the body weight is totally transferred onto the right limb. When the foot becomes planar, the term *foot flat* is applied for that instant of time.
3. *Midstance* refers to the beginning of single support and occurs from 10 to 30% of the gait cycle. This phase begins when the left foot leaves the ground and perdures as the time at which the left foot (swing–period foot) passes the right foot (stance–period foot).
4. *Terminal Stance* occurs between 30 and 50% of the gait cycle. It starts when the heel of the right foot lifts the ground (*heel off*) and ends when the left foot contacts the ground, supporting the body weight.
5. *Preswing* begins when the left foot contacts the ground and finishes when the toe of the right limb makes the terminal contact (*toe off*).

Swing Phase

1. *Initial Swing* occurs from 60 to 75% of the gait cycle. This phase begins when the right foot leaves the ground and perdures until the maximum knee flexion occurs.
2. *Midswing* begins subsequently to maximum knee flexion and ends when the right tibia is in a vertical position. This phase takes place from 75 to 85% and corresponds to the midstance phase of the left foot, being the time at which the two feet are side by side.

3. *Terminal Swing* is the ending phase of the gait cycle, and it corresponds to the deceleration phase. The tibia of the right limb passes beyond perpendicular, and the knee fully extends in preparation for heel contact. At this point, a new gait cycle would begin (Perry, 1992).

For all the lower limbs joints, the magnitude of their movement is proportional to the walking speed. At a typical walking speed, when *heel contact* occurs, the hip is flexed about 30 degrees (Figure 2.12 (a)). With the progression of the body, this joint extends, until the maximum hip extension of about 10 degrees is achieved before *toe off*. Then, the hip starts to flex during *preswing phase*, reaching about 0 degrees of flexion by *toe off* (60% of gait cycle). This joint keeps flexing during the *swing phase*, achieving the maximum flexion (slightly above 30 degrees) right before *heel contact* (Neumann, 2010).

For the knee (Figure 2.12 (b)), the kinematic pattern is a little more complex than for the hip. At *initial contact*, the knee is flexed approximately 5 degrees, and, during the initial 15% of the gait cycle, it flexes continuously an additional 10 to 15 degrees. Then, this joint starts to extend, getting almost fully extended until about *heel off* (between 30% to 40% of the gait cycle). At this stage, the knee starts flexing, achieving around 35 degrees of flexion by the moment of *toe off* (60% of gait cycle). The knee flexion reaches its maximum of approximately 60 degrees in the beginning of *midswing* (75% of gait cycle). In the *mid* and *terminal swing phases*, the knee extends a little below full extension before starting to flex slightly in preparation for *heel contact* (Neumann, 2010).

At the ankle (Figure 2.12 (c)), *heel contact* occurs with a slight plantarflexion, between 0 and 5 degrees. Then, during the *stance phase*, up to 10 degrees of ankle dorsiflexion occurs (from 8% to 45% of the gait cycle). Shortly after *heel off*, the ankle begins to plantarflex, reaching a maximum of 20 degrees of plantarflexion just after *toe off*. In the *swing phase*, the ankle is again dorsiflexed to a neutral position (Neumann, 2010).

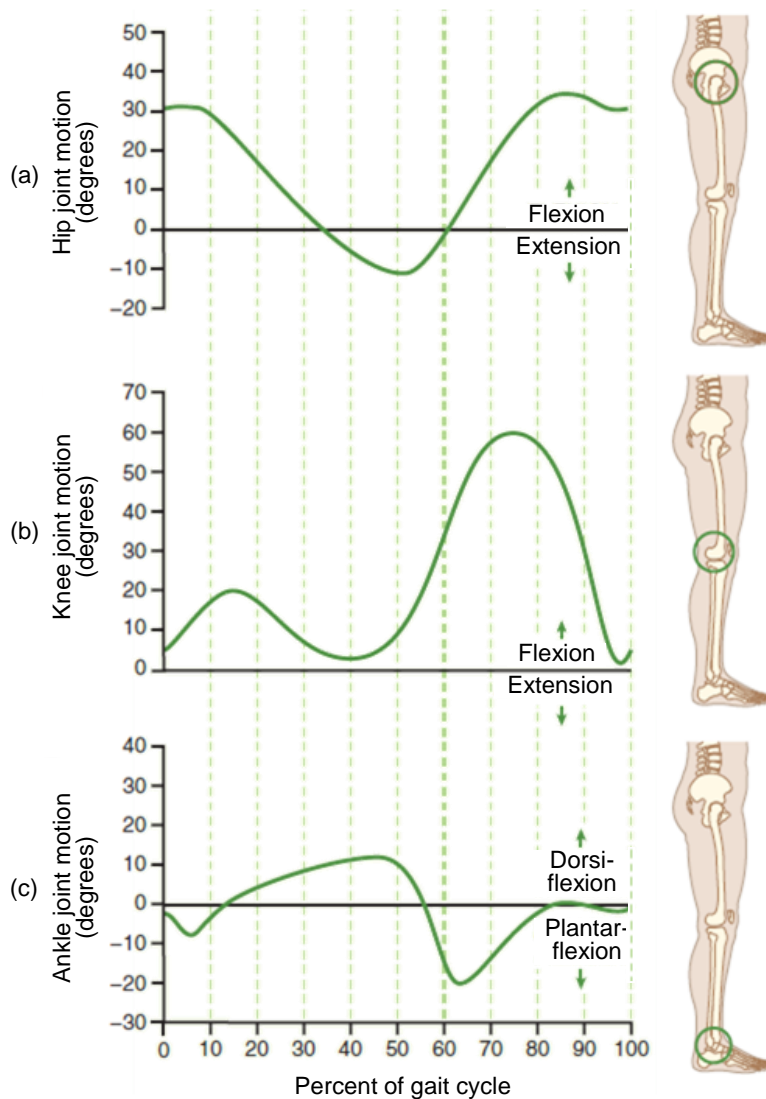


Figure 2.12. Sagittal plane angular rotation of the lower limb joints during a gait cycle. (a) Hip motion; (b) Knee motion; (c) Ankle motion {Adapted from (Neumann, 2010)}.

Overall, for normal walking, approximately 30 degrees of flexion and 10 degrees of extension from the anatomic reference position are needed at the hip; the knee flexes between 2 and 60 degrees; and for the ankle it is required approximately 13 degrees of dorsiflexion and 20 degrees of plantarflexion (Neumann, 2010).

2.4. Summary

In this chapter, a brief description of the biomechanics of the lower limb, in what concerns its movement on the sagittal plane, was presented and analyzed. The use of a uniform terminology associated with the human movement is important, namely in what concerns the three anatomical

reference planes, the anatomical directional terms, and the designation of the movements. Furthermore, the main bones, joints and muscles that allow the normal locomotion of the human body were illustrated. The muscles were organized by functional mover groups of each articulation, specifically for flexion and extension movements. In addition, the normal human gait was described, concerning its main phases, with the aim to understand its sequence of events, and distinguish them in the simulation of the stride period.

Chapter 3 – Multibody Systems Methodologies

In this chapter, the main fundamentals of the formulation for the dynamic analysis of multibody systems are presented. The focus of the dynamic analysis of MBS is to understand the relationship between the motion of the system's constituent components and its underlying causes, such as externally applied forces and moments (Meireles, 2007; Moreira, 2009).

With the purpose of defining the position of each body of a MBS in a 2D context, the multibody formulation is introduced using cartesian coordinates. Furthermore, the formulation of the revolute joints and the guiding constraints is addressed.

It is also summarized how the equations of motion of a MBS can be established, and how to advance the analysis in time, and obtain a solution to the equations of motion. Moreover, as this methodology is susceptible to integration errors, the Baumgarte stabilization method is proposed as a technique to avoid or minimize this phenomenon.

Essentially, the aim of this chapter is to provide the reader with a complete overview of the formulations implemented for dynamic analysis, which follow closely the work of Nikravesh (1988), and are the foundation for all the methodologies presented in the forthcoming chapters.

Finally, the chapter ends with a summary and discussion of the topics covered.

3.1. Multibody Systems Overview

A multibody system can be defined as an assembly of bodies in which some or all of them can move relative to one another. The bodies may be rigid or flexible and are interconnected to each other by kinematic joints that constrain their relative motion, allowing certain degrees-of-freedom (DOF) and constraining others. The bodies are acted upon by forces that can have different sources and different levels of complexity. Under this general concept of MBS, driving and guiding elements for given points of the system components may also be considered, in order to provide prescribed trajectories to the bodies. Figure 3.1 depicts a generic representation of a MBS with its most significant components: bodies, joints and forces elements (Meireles, 2007; Nikravesh, 1988).

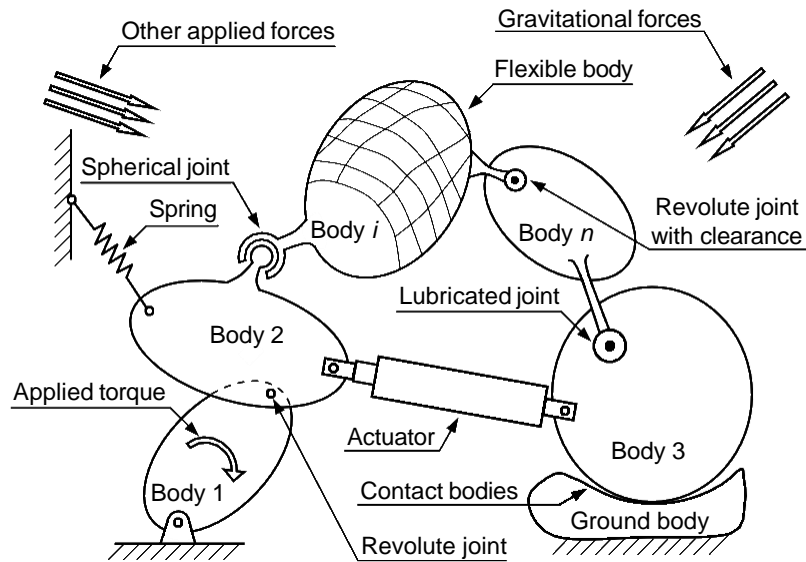


Figure 3.1. Generic representation of a multibody system (Machado et al., 2012).

A body is considered to be rigid when its deformations are assumed to be considerably reduced as they do not affect the global motion of the body, and the distances among its particles do not change during the motion of the global body. The motion of a free rigid body in the two-dimensional space can be fully described by three generalized coordinates associated with the three DOF. On the other hand, a body is said to be flexible, when it has some deformation capacity, so it has three rigid DOF plus the number of generalized coordinates needed to describe the deformations. Although rigid bodies are a representation of reality – because bodies are not totally rigid in nature –, in extensive conventional applications, the bodies have significant stiffness and, consequently, their flexibility can be disregarded, considering the bodies to be perfectly rigid (Machado et al., 2012; Nikraves, 2019).

Multibody systems can differ from very simple to highly complex. Its formulation methodologies, in a generic approach, include two steps: (i) the development of mathematical models of the systems and (ii) the implementation of computational procedures to perform the simulation, analysis and optimization of the global motion produced (Machado et al., 2012).

In order to specify the configuration of a two-dimensional mechanical system, it is necessary to define the coordinates that specify the position of each body. There are different types of coordinates and formalisms that lead to suitable descriptions of multibody systems. In a general perspective, the types of coordinates can be divided into independent and dependent ones. In the first set, the used variables are associated with the DOF of the system. Conversely, the dependent coordinates are further separated in three types: cartesian (or absolute), relative and natural coordinates. The cartesian coordinates are the chosen type to describe the system configuration in this work and will be explained in the present section. The relative coordinates define the position and orientation of a body with respect to a preceding body in

a MBS and can be associated with linear or angular displacements. The natural, also designated as fully cartesian coordinates, involve the employment of only two cartesian coordinates and do not include angular variables (Flores & Lankarani, 2012; Nikravesh, 1988).

The application of cartesian coordinates has the benefit that the formulation of the equations of motion is straightforward and the constraint equations necessary to describe the system restrictions are usually simple to obtain. Additionally, this approach presents low degree of nonlinearity of the resulting equations and a good computational efficiency. With cartesian coordinates, the configurations of the systems are univocally defined. However, the major drawback associated with this type of coordinates formulation is the large number of variables and constraint equations involved (Flores & Lankarani, 2012).

To analyze the movement of a body, it is first necessary to define a nonmoving reference frame, named a global or an inertial frame – denoted as xy –, and a moving frame for each moving body, i , in the system, called a local or a body-fixed frame – denoted as $\xi_i\eta_i$ (Nikravesh, 2019).

In the cartesian coordinates, the vector of generalized coordinates defines the position of each body, and it is usually composed of the location of the CM and the orientation of the body in the system. Therefore, in a 2D problem, a rigid body can be defined by three variables: two coordinates describing the body local system axis position (defined by the global coordinates $\mathbf{r}_i = \{x \ y\}_i^T$) and one angle (θ_i) describing the body orientation with respect to a global coordinate system. The angle that the ξ -axis makes with the x -axis must be measured with respect to the x -axis in the counterclockwise direction. (Nikravesh, 1988, 2019). Regarding this information, the vector of coordinates \mathbf{q}_i that characterizes the position of the body i in the planar context is

$$\mathbf{q}_i = \{x \ y \ \theta\}_i^T \quad (3.1)$$

If a MBS is constituted by n_b rigid bodies, then the number of coordinates needed to characterize the system configuration is $n = 3 \times n_b$. Thus, the vector of generalized coordinates of this MBS system can be written as

$$\mathbf{q} = \{\mathbf{q}_1^T \ \mathbf{q}_2^T \ \mathbf{q}_3^T \ \dots \ \mathbf{q}_{n_b}^T\}^T \quad (3.2)$$

However, the n generalized coordinates of the system are not independent, since there are constraint equations relating them. The number of independent coordinates is called the number of degrees-of-freedom, and represents the minimum number of coordinates required to fully describe the configuration of a system (Flores & Lankarani, 2012; Nikravesh, 1988).

Let \mathbf{s} be a vector defined on a body i , as shown in Figure 3.2. Although this vector rotates and translates with the body movements, its length is constant. The projection of this vector onto the local frame of body i results in two components, namely s_{ξ_i} and s_{η_i} , while the projection of vector \mathbf{s} in the reference frame results in the components s_x and s_y . The local and the global components of the vector \mathbf{s} can be related as

$$\begin{Bmatrix} s_x \\ s_y \end{Bmatrix} = \begin{bmatrix} \cos\theta_i & -\sin\theta_i \\ \sin\theta_i & \cos\theta_i \end{bmatrix} \begin{Bmatrix} s_{\xi_i} \\ s_{\eta_i} \end{Bmatrix} \quad (3.3)$$

and in a compact form by the following equation

$$\mathbf{s} = \mathbf{A}_i \mathbf{s}'_i \quad (3.4)$$

where \mathbf{s} denotes the vector expressed in terms of global coordinates, \mathbf{s}'_i is the vector expressed in the local coordinate system and \mathbf{A}_i represents the planar transformation matrix for body i , which defines the orientation of body-fixed frame, $\xi_i\eta_i$, with respect to the global coordinate system, xy , being given by (Flores & Lankarani, 2012; Nikravesh, 2019)

$$\mathbf{A}_i = \begin{bmatrix} \cos\theta_i & -\sin\theta_i \\ \sin\theta_i & \cos\theta_i \end{bmatrix} \quad (3.5)$$

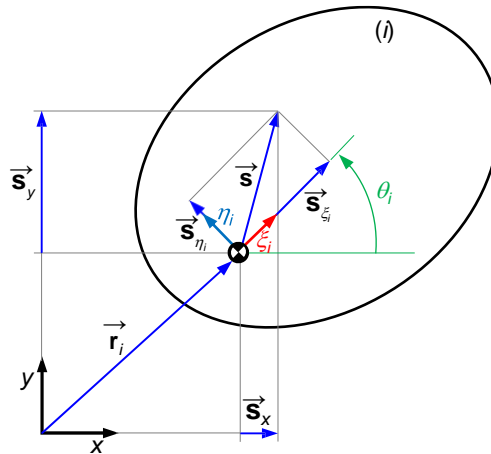


Figure 3.2. Components of a vector attached to a body in global and local systems of coordinates.

Vectors are also used to define the position of points attached to a body, with respect to the origin of the body-fixed coordinate system. Therefore, any point on a body can be located in relation to the inertial frame as well. For instance, a generic point P_i on body i can be defined by knowing the global position of the body CM \mathbf{r}_i and the position vector \mathbf{s}_i^P , that represents the position of point P_i relative to

the body local frame, as depicted in the Figure 3.3. It should be noted that, in further references, \mathbf{s}_i^P signifies the position vector in global coordinates and $\mathbf{s}_i^{\prime P}$ refers to the local components of point P_i ($\mathbf{s}_i^{\prime P} = \{\xi_i^P \ \eta_i^P\}^T$) (Nikravesh, 1988, 2019).

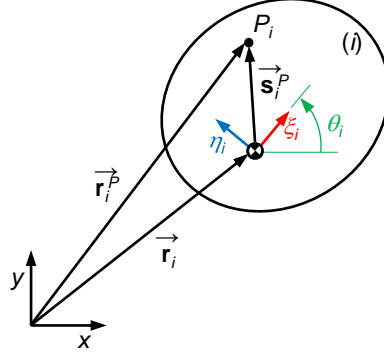


Figure 3.3. Locating point P_i relative to the body-fixed and global coordinate systems.

The local and global coordinates of point P_i can be related by the following equation

$$\mathbf{r}_i^P = \mathbf{r}_i + \mathbf{s}_i^P = \mathbf{r}_i + \mathbf{A}_i \mathbf{s}_i^{\prime P} \quad (3.6)$$

where \mathbf{A}_i is the transformation matrix given by Eq. (3.5).

In the expanded form, Eq. (3.6) can be expressed as (Nikravesh, 1988, 2019)

$$\begin{Bmatrix} x_i^P \\ y_i^P \end{Bmatrix} = \begin{Bmatrix} x_i \\ y_i \end{Bmatrix} + \begin{bmatrix} \cos \theta_i & -\sin \theta_i \\ \sin \theta_i & \cos \theta_i \end{bmatrix} \begin{Bmatrix} \xi_i^P \\ \eta_i^P \end{Bmatrix} \quad (3.7)$$

or, alternatively,

$$x_i^P = x_i + \xi_i^P \cos \theta_i - \eta_i^P \sin \theta_i \quad (3.8)$$

$$y_i^P = y_i + \xi_i^P \sin \theta_i + \eta_i^P \cos \theta_i \quad (3.9)$$

The velocity components of point P_i can be obtained by differentiating Eqs. (3.8) and (3.9) with respect to time, yielding

$$\dot{x}_i^P = \dot{x}_i - (\xi_i^P \sin \theta_i + \eta_i^P \cos \theta_i) \dot{\theta}_i \quad (3.10)$$

$$\dot{y}_i^P = \dot{y}_i + (\xi_i^P \cos \theta_i - \eta_i^P \sin \theta_i) \dot{\theta}_i \quad (3.11)$$

After a second differentiation of Eqs. (3.8) and (3.9) with respect to time, the acceleration equations are obtained as (Nikravesh, 2019)

$$\ddot{x}_i^P = \ddot{x}_i - (\xi_i^P \sin \theta_i + \eta_i^P \cos \theta_i) \ddot{\theta}_i - (\xi_i^P \cos \theta_i - \eta_i^P \sin \theta_i) \dot{\theta}_i^2 \quad (3.12)$$

$$\ddot{y}_i^P = \ddot{y}_i + (\xi_i^P \cos \theta_i - \eta_i^P \sin \theta_i) \ddot{\theta}_i - (\xi_i^P \sin \theta_i + \eta_i^P \cos \theta_i) \dot{\theta}_i^2 \quad (3.13)$$

3.2. Constraints Formulation

A kinematic pair imposes restrictions on the relative motion between the bodies it comprises and, therefore, it reduces the number of DOF of the system. The kinematic relationships between the defined coordinates of a system are called constraint equations. The configuration of the MBS is described by n cartesian coordinates, then a set of m algebraic kinematic independent holonomic constraints¹, Φ , can be written in a compact form as

$$\Phi(\mathbf{q}, t) = 0 \quad (3.14)$$

where \mathbf{q} is the vector of generalized coordinates and t is the time variable (Nikravesh, 1988, 2019).

The evaluation of the velocities and accelerations of the system elements is performed using the velocity and acceleration constraint equations. Differentiating Eq. (3.14) with respect to time, yields the velocity constraint equations,

$$\Phi_{\mathbf{q}} \dot{\mathbf{q}} = -\Phi_t = \mathbf{v} \quad (3.15)$$

where $\Phi_{\mathbf{q}} = \partial\Phi / \partial\mathbf{q}$ is the Jacobian matrix of the constraint equations, $\dot{\mathbf{q}}$ is the vector of generalized velocities, and $\mathbf{v} = -\partial\Phi / \partial t$ is the right-hand side of velocity equations. It should be noticed that only rheonomic constraints², associated with driving or guiding equations, contribute with non-zero entries to the vector \mathbf{v} .

After a second differentiation of the Eq. (3.14) with respect to time, the acceleration constraint equations are obtained as

$$\Phi_{\mathbf{q}} \ddot{\mathbf{q}} = -(\Phi_{\mathbf{q}} \dot{\mathbf{q}})_{\mathbf{q}} \dot{\mathbf{q}} - 2\Phi_{\mathbf{q}t} \dot{\mathbf{q}} - \Phi_{tt} = \boldsymbol{\gamma} \quad (3.16)$$

where $\ddot{\mathbf{q}}$ is acceleration vector and $\boldsymbol{\gamma}$ is the right-hand side vector of the acceleration constraint equations, that is, the vector of quadratic velocity terms, which are exclusively function of velocity, position and time. In the case of scleronomic constraints³, the terms Φ_t in Eq. (3.15) and $\Phi_{\mathbf{q}t}$ and Φ_{tt} in Eq. (3.16) vanish (Flores et al., 2008).

¹ Holonomic constraints are algebraic equations that are expressed as function of the coordinates and, possibly, time (Nikravesh, 1988).

² Rheonomic constraints are holonomic constraints, in which the time appears explicitly (Flores et al., 2008).

³ Scleronomic constraints are holonomic constraints that are not explicitly dependent on time (Flores et al., 2008).

3.2.1. Revolute Joint

A revolute joint constrains the relative translation between two bodies, allowing only the relative rotation. A schematic representation of this type of kinematic joint, connecting two bodies, i and j , is shown in Figure 3.4, where the center of the joint is denoted by the point P . This point can be considered to be two coincident points, each one belonging to a different body: P_i on body i and P_j on body j . Such situation can be expressed as

$$\mathbf{r}_i + \mathbf{s}_i^P - \mathbf{r}_j - \mathbf{s}_j^P = \mathbf{0} \quad (3.17)$$

which establishes the constraint equations for a revolute joint, and is equivalent to

$$\Phi^{(r,2)} \equiv \mathbf{r}_i + \mathbf{A}_i \mathbf{s}_i^{iP} - \mathbf{r}_j - \mathbf{A}_j \mathbf{s}_j^{jP} = \mathbf{0} \quad (3.18)$$

In a more explicit and expanded form, the two constraint equations for a revolute joint can be expressed by

$$\Phi^{(r,1st)} \equiv x_i + \xi_i^P \cos \theta_i - \eta_i^P \sin \theta_i - x_j - \xi_j^P \cos \theta_j + \eta_j^P \sin \theta_j = 0 \quad (3.19)$$

$$\Phi^{(r,2nd)} \equiv y_i + \xi_i^P \sin \theta_i + \eta_i^P \cos \theta_i - y_j - \xi_j^P \sin \theta_j - \eta_j^P \cos \theta_j = 0 \quad (3.20)$$

Therefore, in a 2D context, if two bodies are connected by a revolute joint, the number of DOF of the system is reduced by two (Nikravesh, 1988).

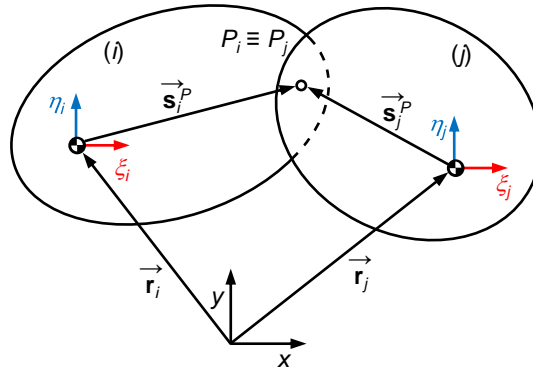


Figure 3.4. Revolute joint connecting bodies i and j (Flores & Lankarani, 2012).

The partial derivative of Eqs. (3.19) and (3.20) with respect to generalized coordinates, \mathbf{q} , i.e., $\Phi_{\mathbf{q}}^{(r,2)}$, provides two rows to the overall Jacobian matrix. Since $\Phi^{(r,2)}$ is a function of only \mathbf{q}_i and \mathbf{q}_j , then $\Phi_{\mathbf{q}}^{(r,2)}$ may have non-zero entries only in the columns associated with the general coordinates of bodies i and j . Hence, the Jacobian matrix is given by

$$\Phi_{\mathbf{q}}^{(r,2)} = \begin{bmatrix} \frac{\partial \Phi^{(r,1st)}}{\partial x_i} & \frac{\partial \Phi^{(r,1st)}}{\partial y_i} & \frac{\partial \Phi^{(r,1st)}}{\partial \theta_i} & \frac{\partial \Phi^{(r,1st)}}{\partial x_j} & \frac{\partial \Phi^{(r,1st)}}{\partial y_j} & \frac{\partial \Phi^{(r,1st)}}{\partial \theta_j} \\ \frac{\partial \Phi^{(r,2nd)}}{\partial x_i} & \frac{\partial \Phi^{(r,2nd)}}{\partial y_i} & \frac{\partial \Phi^{(r,2nd)}}{\partial \theta_i} & \frac{\partial \Phi^{(r,2nd)}}{\partial x_j} & \frac{\partial \Phi^{(r,2nd)}}{\partial y_j} & \frac{\partial \Phi^{(r,2nd)}}{\partial \theta_j} \end{bmatrix} \quad (3.21)$$

generating the corresponding values of the Jacobian terms as follows

$$\Phi_{\mathbf{q}}^{(r,2)} = \begin{bmatrix} 1 & 0 & -\xi_i^P \sin \theta_i - \eta_i^P \cos \theta_i & -1 & 0 & \xi_j^P \sin \theta_j + \eta_j^P \cos \theta_j \\ 0 & 1 & \xi_i^P \cos \theta_i - \eta_i^P \sin \theta_i & 0 & -1 & -\xi_j^P \cos \theta_j + \eta_j^P \sin \theta_j \end{bmatrix} \quad (3.22)$$

Since revolute joints consist in scleronomic constraints, i.e., the revolute joint constraints do not depend explicitly on time, the right-hand side vector of the velocity constraint equations is given by

$$\mathbf{v}^{(r,2)} = -\Phi_t = \mathbf{0} \quad (3.23)$$

In consequence, the right-hand side of the acceleration constraint equations is represented as

$$\gamma^{(r,2)} = -(\Phi_{\mathbf{q}} \dot{\mathbf{q}})_{\mathbf{q}} \quad (3.24)$$

which can be expanded as (Nikravesh, 1988)

$$\gamma^{(r,2)} = \begin{bmatrix} (\xi_i^P \cos \theta_i - \eta_i^P \sin \theta_i) \dot{\theta}_i^2 - (\xi_j^P \cos \theta_j - \eta_j^P \sin \theta_j) \dot{\theta}_j^2 \\ (\xi_i^P \sin \theta_i + \eta_i^P \cos \theta_i) \dot{\theta}_i^2 - (\xi_j^P \sin \theta_j + \eta_j^P \cos \theta_j) \dot{\theta}_j^2 \end{bmatrix} \quad (3.25)$$

3.2.2. Guiding Constraints

The guiding constraints are a type of rheonomic constraints which impose the trajectories of determined points on the bodies, namely the CM, as it is represented in Figure 3.5. For a free body (i) in two-dimensional space, the guiding constraint equations can be written as

$$\Phi^{(g,3)} \equiv \begin{bmatrix} x_i - t_i^x(t) \\ y_i - t_i^y(t) \\ \theta_i - t_i^\theta(t) \end{bmatrix} = \mathbf{0} \quad (3.26)$$

where $t_i^k(t)$, with $k = \{x, y, \theta\}$, represents the trajectory described by the CM of body i (Meireles, 2007).

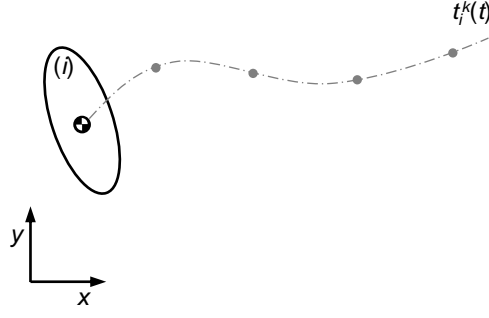


Figure 3.5. Representation of a trajectory described by the CM of a free body.

The contribution of the guiding constraint equations to the Jacobian matrix of the constraints can be evaluated as

$$\Phi_{\mathbf{q}}^{(g,3)} = \begin{bmatrix} \frac{\partial \Phi^{(g,1st)}}{\partial x_i} & \frac{\partial \Phi^{(g,1st)}}{\partial y_i} & \frac{\partial \Phi^{(g,1st)}}{\partial \theta_i} \\ \frac{\partial \Phi^{(g,2nd)}}{\partial x_i} & \frac{\partial \Phi^{(g,2nd)}}{\partial y_i} & \frac{\partial \Phi^{(g,2nd)}}{\partial \theta_i} \\ \frac{\partial \Phi^{(g,3rd)}}{\partial x_i} & \frac{\partial \Phi^{(g,3rd)}}{\partial y_i} & \frac{\partial \Phi^{(g,3rd)}}{\partial \theta_i} \end{bmatrix} \quad (3.27)$$

which can be expressed as

$$\Phi_{\mathbf{q}}^{(g)} = \hat{\mathbf{I}} \quad (3.28)$$

where $\hat{\mathbf{I}}$ is a permuted non-square identity matrix, in which the 1s are present in the columns associated with the independent variables (Flores & Lankarani, 2016; Nikravesh, 1988).

The right-hand side of the velocity and acceleration constraints can be evaluated as follows (Flores & Lankarani, 2016)

$$\mathbf{v}^{(g,3)} = \left\{ \frac{\partial \Phi^{(g,1st)}}{\partial t} \quad \frac{\partial \Phi^{(g,2nd)}}{\partial t} \quad \frac{\partial \Phi^{(g,3rd)}}{\partial t} \right\}^T \quad (3.29)$$

$$\boldsymbol{\gamma}^{(g,3)} = \left\{ \frac{\partial^2 \Phi^{(g,1st)}}{\partial t^2} \quad \frac{\partial^2 \Phi^{(g,2nd)}}{\partial t^2} \quad \frac{\partial^2 \Phi^{(g,3rd)}}{\partial t^2} \right\}^T \quad (3.30)$$

3.3. Description of the Equations of Motion

In order to examine the dynamic response of a constrained MBS, it is first necessary to formulate the equations of motion that govern its behavior. According to Nikravesh's formulation, the equations of motion for constrained MBS of rigid bodies are described as (Nikravesh, 1988)

$$\mathbf{M}\ddot{\mathbf{q}} = \mathbf{g} + \mathbf{g}^{(c)} \quad (3.31)$$

where \mathbf{M} is the global system mass matrix, which is a constant diagonal matrix, containing the mass and moments of inertia of all bodies, $\ddot{\mathbf{q}}$ is the acceleration vector, \mathbf{g} is the generalized force vector that contains all external forces and moments applied on the system – such as those associated with gravitational field and contact events –, and $\mathbf{g}^{(c)}$ is the vector of constraint reaction forces, which can be expressed in terms of the Jacobian matrix of the constraint equations (Φ_q) and the Lagrange multipliers vector (λ) as

$$\mathbf{g}^{(c)} = -\Phi_q^T \lambda \quad (3.32)$$

The λ vector contains m unknown Lagrange multipliers related to the m algebraic kinematic independent holonomic constraints. The Lagrange multipliers are physically associated with the reaction forces and moments produced between the bodies interconnected by kinematic joints (Flores et al., 2008; Nikravesh, 1988). Thus, from the substitution of Eq. (3.32) in Eq. (3.31) yields

$$\mathbf{M}\ddot{\mathbf{q}} + \Phi_q^T \lambda = \mathbf{g} \quad (3.33)$$

It should be noticed that Eq. (3.33) represents a system of n second-order ordinary differential equations with $n + m$ unknowns, corresponding to the generalized acceleration vector, $\ddot{\mathbf{q}}$, and to the vector of the Lagrange multipliers, λ . In dynamic analysis, in order to obtain a unique solution, it is necessary to consider not only the differential equations of motion, but also the constraint equations. Thus, Eq. (3.16) can be appended to Eq. (3.33) and re-written in matrix form as

$$\begin{bmatrix} \mathbf{M} & \Phi_q^T \\ \Phi_q & \mathbf{0} \end{bmatrix} \begin{Bmatrix} \ddot{\mathbf{q}} \\ \lambda \end{Bmatrix} = \begin{Bmatrix} \mathbf{g} \\ \gamma \end{Bmatrix} \quad (3.34)$$

which can be solved for $\ddot{\mathbf{q}}$ and λ using any numerical algorithm for linear equations. In mathematical terms, the simulation of a constrained MBS requires the solution of a set of n differential equations coupled with a set of m algebraic equations, producing a system of $n + m$ differential and algebraic equations (DAE), with $n + m$ unknowns. The equations of motion for MBS are derived from the Newton-Euler formulation in combination with the augmentation method. The Newton-Euler equations represent the translational and rotational motions of bodies, while the augmentation method denotes the process where the algebraic kinematic constraint equations are adjoined to the differential equations of motion, so that the number of unknowns for which the system is being solved is in agreement with the number of system equations. As a consequence, the equations of motion of MBS are formed as a set of differential algebraic equations. The numerical solution of the system of DAE is not straightforward and the most

frequently used numerical integration algorithms are useful in solving ordinary differential equations (ODE). In this context, one of the most applied methods to solve this problem consists in the conversion of the DAE system into a set of ODE (Flores et al., 2008; Flores & Lankarani, 2012; Nikravesh, 1988).

3.4. Resolution of the Equations of Motion

In order to advance the analysis in time, the equations of motion need to be solved and the state variables integrated. In each integration time step, the accelerations vector, $\ddot{\mathbf{q}}$, and the velocities vector, $\dot{\mathbf{q}}$, are integrated, with the objective to obtain, respectively, the system velocities and positions for the next time step. This process is repeated until the final analysis time is reached. As the dynamic analysis of MBS is an initial value problem, it should be noticed that it is required a set of initial conditions, – positions and velocities –, to initiate the dynamic simulation (Flores et al., 2008; Nikravesh, 1988).

A numerical solution to the equations of motion may be obtained by applying, for instance, the direct integration method (DIM), which is a standard numerical integration algorithm, that solves first-order differential equations that take the form

$$\dot{\mathbf{y}} = f(\mathbf{y}, t) \quad (3.35)$$

Therefore, if there are n second-order differential equations of motion, they are converted into $2n$ first-order differential equations, by defining the \mathbf{y} and $\dot{\mathbf{y}}$ vectors, – which contains, respectively, the system positions and velocities and the system velocities and accelerations –, as follows (Flores et al., 2008; Nikravesh, 1988),

$$\mathbf{y} = \begin{Bmatrix} \mathbf{q} \\ \dot{\mathbf{q}} \end{Bmatrix} \quad \text{and} \quad \dot{\mathbf{y}} = \begin{Bmatrix} \dot{\mathbf{q}} \\ \ddot{\mathbf{q}} \end{Bmatrix} \quad (3.36)$$

The process of numeric integration at instant of time t can be represented by the following diagram,

$$\dot{\mathbf{y}}(t) \xrightarrow{\text{integration}} \mathbf{y}(t + \Delta t) \quad (3.37)$$

which means that velocities and accelerations, at instant t , yield positions and velocities, at next time step, $t + \Delta t$, after the integration process (Nikravesh, 1988).

The algorithm for dynamic analysis of MBS based on the DIM of the equations of motion is explained in the flowchart presented in Figure 3.6.

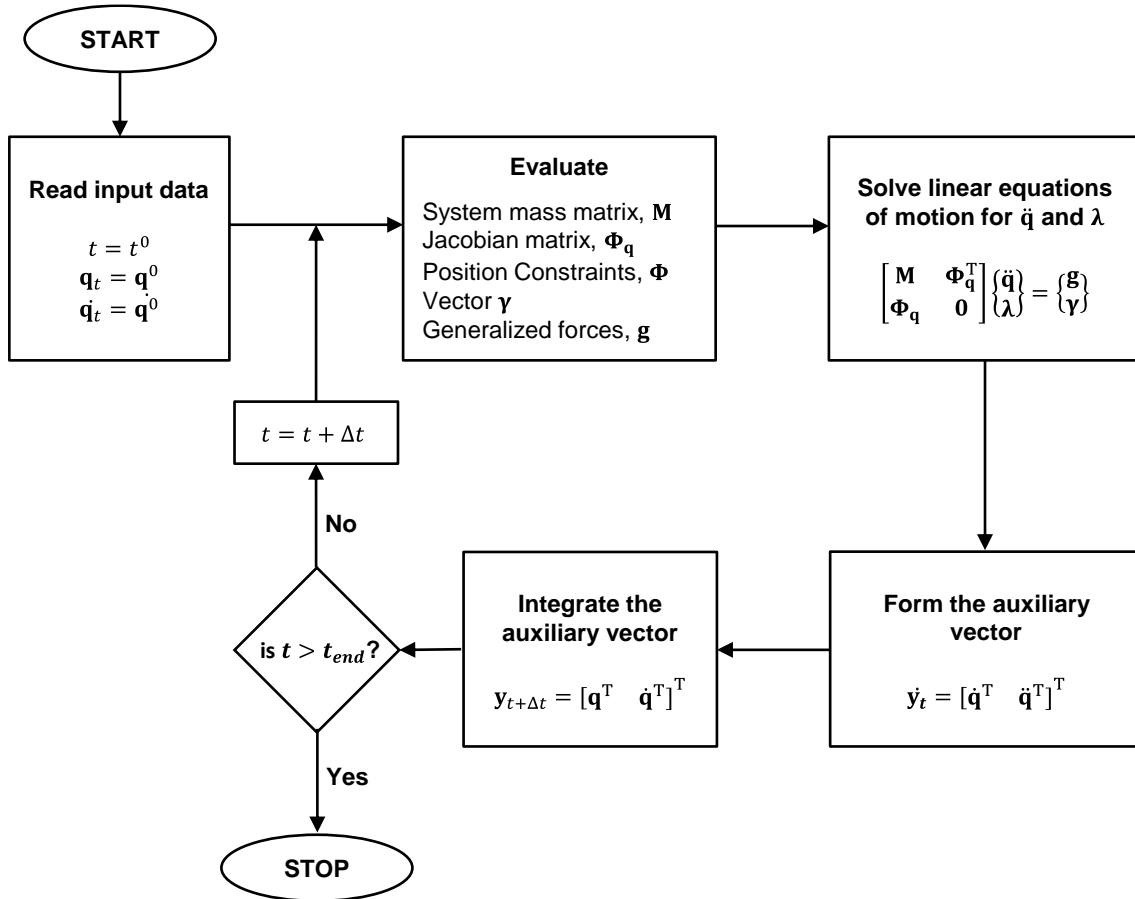


Figure 3.6. Flowchart of computational procedure for dynamic analysis of multibody systems based on the direct integration method {Adapted from (Flores et al., 2008)}.

To initiate the dynamic analysis, at $t = t^0$, the initial conditions of the positions, \mathbf{q}^0 , and of the velocities, $\dot{\mathbf{q}}^0$, are required for initiating the integration process. These values must satisfy the constraint equations defined in Eqs. (3.14) and (3.15). The DIM can be resumed by the following steps:

1. Start at instant t^0 with the given set of initial conditions for positions, \mathbf{q}^0 , and for velocities, $\dot{\mathbf{q}}^0$.
2. Assemble the global mass matrix, \mathbf{M} , evaluate the Jacobian matrix, Φ_q , build the constraint equations, Φ , calculate the right-hand side vector of the accelerations, γ , and determine the vector of generalized forces, \mathbf{g} .
3. Solve the linear system of the equations of motion – Eq. (3.34) – for a constrained MBS in order to obtain, at instant t the accelerations, $\ddot{\mathbf{q}}$, and the Lagrange multipliers, λ .
4. Assemble the vector $\dot{\mathbf{y}}_t$, which contains the generalized velocities, $\dot{\mathbf{q}}$, and accelerations, $\ddot{\mathbf{q}}$, for the instant t .
5. Integrate the $\dot{\mathbf{q}}$ and $\ddot{\mathbf{q}}$ vectors for time step $t + \Delta t$ and obtain the new positions and velocities.

6. Increment time. If the current time is smaller than the final time, go to step 2 and continue with the procedure for a new time step, until the final time of analysis is reached. Otherwise stop the dynamic analysis.

The most used numerical integration methods, employed to solve the initial-value problem, are the Runge–Kutta methods. The DIM of the equations of motion is susceptible to integration errors because the position and velocity constraints equations – Eqs. (3.14) and (3.15) respectively – are only satisfied at the initial instant of time, t^0 , as they do not explicitly appear in the system of the equations of motion – Eq. (3.34). In fact, only the second derivatives of the constraint equations will be satisfied at every integration step. In the initial few time steps, the constraint violations are usually small and negligible. However, as the time is incremented, the error in computed values for kinematic parameters is accumulated, due to the finite precision of the numerical methodologies, and constraint violations increase, being more evident with stiff systems⁴. Consequently, unacceptable results are generated, which requires the implementation of a constraint stabilization technique to avoid or minimize this phenomenon, especially for more prolonged simulations (Flores et al., 2008, 2011).

Several methods to avoid or minimize this phenomenon have been suggested and tested, and the most commonly applied among them is the Baumgarte stabilization method (BSM), due to its simplicity and easiness for computational implementation (Baumgarte, 1972). The BSM is used to keep the errors associated with constraint violations under control and its principle is to damp out the acceleration constraint violations by feeding back the position and velocity of constraint violations, as it is represented in Figure 3.7.

⁴ A system is considered to be stiff if it contains rapidly and slowly varying components, and the natural frequencies of the system are widely spread. The stiffness can be produced by the physical characteristics of the multibody system, such as components with large differences in their masses, stiffness and/or damping. It should be noticed that, in order to capture the fast components of the response and keep the numerical error within the limits, a smaller time step would be required to obtain an accurate solution, which may be prohibitive or unrealistic in terms of computer resources (Flores et al., 2008; Nikravesh, 1988).

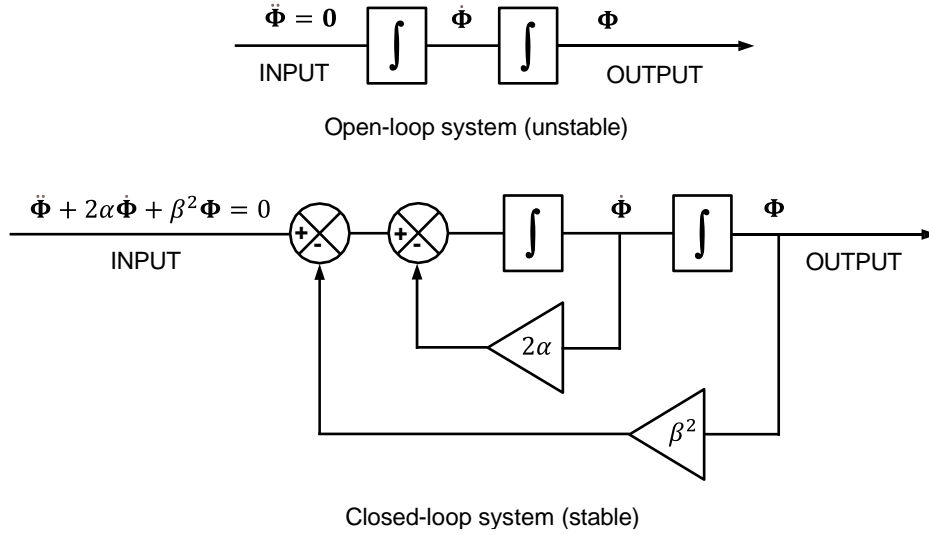


Figure 3.7. Open-loop (without the application of BSM) and closed-loop (with the application of BSM) control systems.

This method allows the existence of a slight violation of constraints before the manifestation of the corrective action, in order to force the violation to vanish. The objective of the BSM is to replace the differential Eq. (3.16) by the following expression,

$$\ddot{\Phi} + 2\alpha\dot{\Phi} + \beta^2\Phi = 0 \quad (3.38)$$

that is a differential equation for a closed-loop system in terms of kinematic constraint equations, in which the terms $2\alpha\dot{\Phi}$ and $\beta^2\Phi$ are the feedback control terms that achieve stability for the differential equation.

As Figure 3.7 shows, in open-loop systems, Φ and $\dot{\Phi}$ do not converge to zero if any perturbation occurs and, consequently, the system is unstable. Thus, applying the BSM, the equations of motion for a system subjected to holonomic constraints are stated in the following form (Flores et al., 2011)

$$\begin{bmatrix} \mathbf{M} & \Phi_q^T \\ \Phi_q & \mathbf{0} \end{bmatrix} \begin{Bmatrix} \ddot{\mathbf{q}} \\ \lambda \end{Bmatrix} = \begin{Bmatrix} \mathbf{g} \\ \gamma - 2\alpha\dot{\Phi} - \beta^2\Phi \end{Bmatrix} \quad (3.39)$$

The selection of the feedback parameters, α and β , depends on several factors, namely, the integrator used and the model of the MBS. This ambiguity in choosing the feedback parameters is the major drawback of Baumgarte's method, which usually involves a trial-and-error procedure, since there is no reliable method for selecting the coefficients α and β . The improper choice of these coefficients can lead to unacceptable results in the multibody system dynamics. In general, if α and β are chosen as positive constants, the stability of the general solution of Eq. (3.39) is guaranteed. Furthermore, when the value of α is equal to the value of β , critical damping is achieved, which usually stabilizes the system response quickly. Baumgarte (1972) indicated that the values of the feedback parameters of $\alpha = \beta = 5$

are a good choice for a MBS made of rigid bodies. However, the parameters α and β should be, in general, equal to one another and typical values of the stabilization parameters range from 1 to 20 (Flores et al., 2008).

3.5. Summary

In this chapter, the main fundamentals of the formulation for the dynamic analysis of multibody systems were presented and discussed. The multibody formulation was introduced and detailed for the type of coordinates adopted – cartesian coordinates – in order to define the position of each body of a MBS in the two-dimensional space. Additionally, the major aspects related to the formulation of the revolute joints and the guiding constraints, for a 2D context, were also reviewed. The formulation follows the work of Nikravesh (1988) and is the supporting structure for all the methodologies and dynamic analysis presented in the forthcoming chapters.

It was also summarized how the equations of motion of a MBS can be established, and how to advance the analysis in time, integrating the state variables, to obtain a numerical solution to the equations of motion. In this context, the computational procedure for dynamic simulation, based on the DIM, was considered. For starting the integration process, it is required a set of initial conditions, for positions and velocities, which must satisfy the positions and velocities constraint equations. From those initial values, the equations of motion are solved for the system accelerations and for Lagrange multipliers. Then, by integration of the velocity and acceleration vectors, the positions and velocities at the next time step are obtained. This procedure is repeated until the final time is reached. This integration process can be performed using, for instance, a Runge–Kutta method. Additionally, it was stated that this methodology is susceptible to integration errors, and the BSM may be applied with the intent of keeping the constraints violation under control.

Chapter 4 – Dynamic Analysis of the Human Gait

The dynamic analysis of the human gait typically requires three distinct types of input data: (i) anthropometric information concerning the anatomical segments dimensions and masses; (ii) kinematic information, regarding trajectories of specific anatomical points of the biomechanical model, used to describe its motion in a unique way; (iii) and kinetic information describing all the external applied forces to the biomechanical model and their respective points of application (Meireles, 2007; Tavares da Silva, 2003).

In this chapter, a description of the developed multibody model, based on the MBS formulation discussed in the previous chapter, is presented. The geometric characteristics of the rigid bodies, the connection between them by ideal revolute joints, the guidings that prescribe the trajectories of the segments, and the introduction of the external forces are described. The constraint equations are also established. The established biomechanical model was implemented in a computational program developed in MATLAB, and the processes involved are described in this chapter.

The bodies' trajectories data were obtained experimentally and, therefore, are prone to errors and uncertainties. In this context, the most common sources of errors that affect the kinematic input data and problems associated with them are also aborded. The required set of initial conditions to initiate the dynamic analysis is prescribed and the consistency of these initial conditions are analyzed in order to be consistent with the kinematic structure of the biomechanical model.

Moreover, three interpolation methods available in MATLAB are compared and discussed for application in the discrete data of the bodies' trajectories and the GRF components.

Furthermore, a solution to the equations of motion is obtained by applying a numerical integration algorithm, namely the MATLAB '*ode45*' solver, and the main characteristics of it are also examined in this chapter. It is also presented a study on the influence of the values of the Baumgarte stabilization parameters on the violation of constraints.

Finally, the computer animation of the biomechanical model developed in MATLAB, for visualization of the human gait, is described, and at the end, a summary of the topics covered in the present chapter is provided.

4.1. Biomechanical Multibody Model Description

This section intends to briefly describe the biomechanical model of the human body – the $\frac{1}{2}$ HAT-leg model, represented in the Figure 4.1 – used in dynamic analysis of the human gait in the sagittal plane.

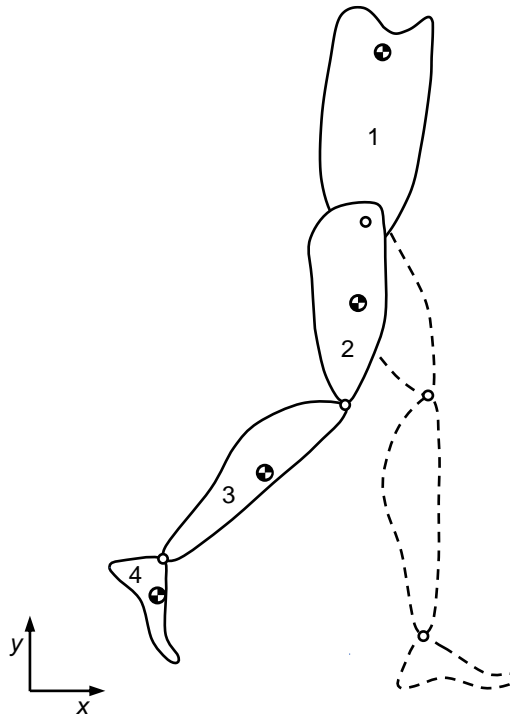


Figure 4.1. $\frac{1}{2}$ HAT-leg model representation.

The model is composed of four rigid bodies, corresponding to the main segments of the right side of the human body – $\frac{1}{2}$ HAT⁵, thigh, leg and foot. In Figure 4.1, the right leg is represented in solid line, while the left leg, which will not be considered, is in dashed line. The model has 12 coordinates ($n = 12$) since it has four movable bodies with three DOF each. These bodies, their anatomical description and the relevant anthropometric information are summarized in Table 4.1. The segments' length, mass, CM location and moment of inertia are representative of a person with 56.70 kg of total body mass, and were obtained from the work of Meireles (2007), which is based on Winter (2005). The bodies are connected by three ideal revolute joints and, consequently, six constraints are added to the system, since each joint removes two DOF from the system. Hence, the $\frac{1}{2}$ HAT-leg multibody system has six DOF, that correspond to three rotations about the revolute joints – one DOF for hip flexion-extension motion, one DOF for knee flexion-extension and one DOF for ankle dorsiflexion-plantarflexion –, plus two translations and one

⁵ HAT is the acronym for *head-arms-trunk*.

rotation of the system. These six DOF are associated with the guiding constraints, according to an initially prescribed kinematics.

Table 4.1. Anthropometric data for the segments of the ½ HAT-leg model (Meireles, 2007; Winter, 2009)

Body	Anatomical description	Length [m]	CM Proximal Location ⁶ [m]	Mass [kg]	Moment of Inertia [kg.m ²]
1	½ right HAT (greater trochanter/mid rib)	0.2575	-0.0355 ⁷	19.2213	1.03923
2	right thigh (greater trochanter/femoral condyles)	0.3141	0.1360	5.67000	0.05836
3	right leg (femoral condyles/medial malleolus)	0.4081	0.1840	2.63655	0.04005
4	right foot (lateral malleolus/head metatarsal II)	0.1221	0.0610	0.82215	0.00273

The global system mass matrix, \mathbf{M} , which is a constant diagonal matrix, containing the mass and moments of inertia of all bodies, can be defined, for the considered model, as follows

$$\mathbf{M} = \text{diag}[m_1 \quad m_1 \quad I_1 \quad m_2 \quad m_2 \quad I_2 \quad m_3 \quad m_3 \quad I_3 \quad m_4 \quad m_4 \quad I_4] \quad (4.1)$$

In order to perform a dynamic analysis of a MBS, the cartesian coordinates of the CM of each body are grouped in column vector \mathbf{q} , the generalized coordinates vector, which defines, in a unique way, the configuration of the system at any instant of time. For the ½ HAT-leg model this vector is organized as follows

$$\mathbf{q} = \{x_1 \quad y_1 \quad \theta_1 \quad x_2 \quad y_2 \quad \theta_2 \quad x_3 \quad y_3 \quad \theta_3 \quad x_4 \quad y_4 \quad \theta_4\}^T \quad (4.2)$$

Each rigid body i has a local reference frame attached to it, with its origin located at the CM of the body. The ξ_i is aligned with the segment, while the η_i is perpendicular to the segment's extension, as depicted in Figure 4.2. Figure 4.2 also shows the representation of the orientation of each segment with respect to the global reference frame.

⁶ The CM proximal location refers to the distance from the segment's CM to the proximal end of that segment (Winter, 2009).

⁷ The CM of the ½ right HAT is located 0.0355 m above its proximal end, which leads to a negative value of CM proximal location (Meireles, 2007).

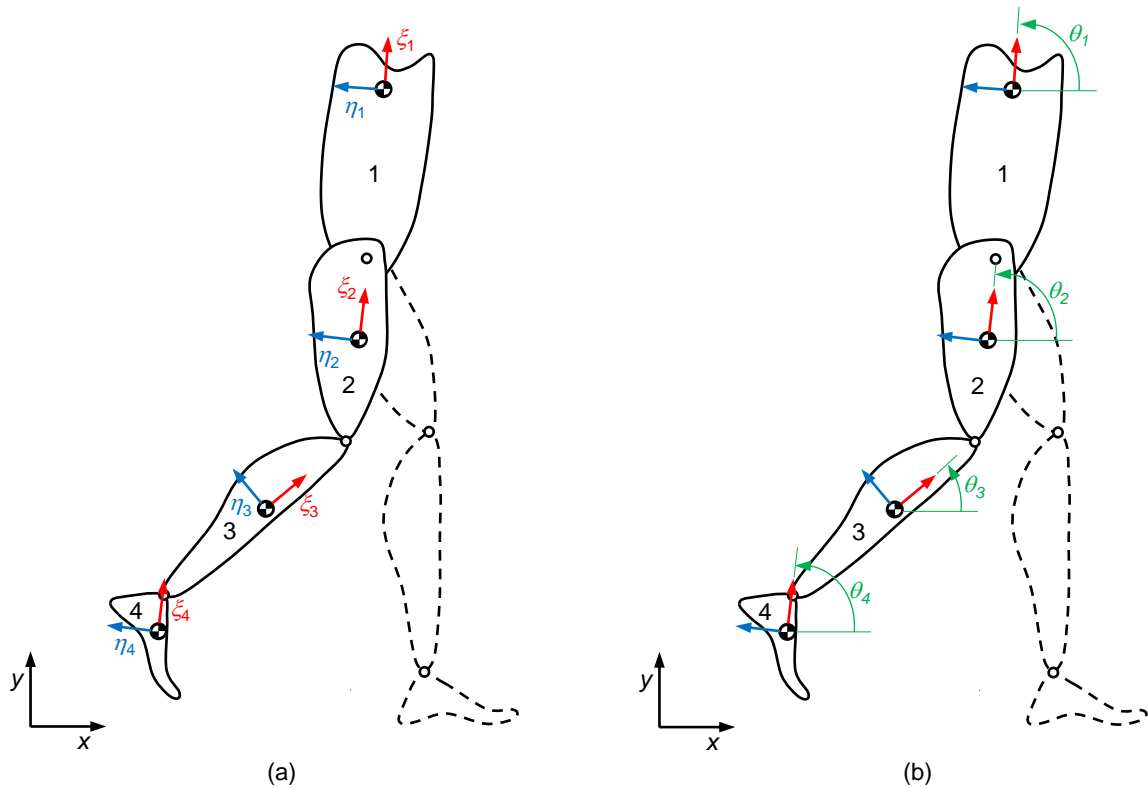


Figure 4.2. (a) Representation of the local reference frames on the $\frac{1}{2}$ HAT-leg model; (b) Representation of the orientation of each segment with respect to the global coordinate system.

This model was developed within a MATLAB computer code, using the multibody formulation with cartesian coordinates, described in the previous chapter. This numeric simulator was the computational framework that supports all the analyses performed in this work.

4.2. Kinematic Constraints Formulation

The constraints imposed by revolute joints are geometric constraints that can be described as two coincident points, each one belonging to a different body. The center of the joint, which constrains two bodies, i and j , is denoted by the point P – where the points P_i and P_j are coincident. The local coordinates of the point P on bodies i and j are those used by Meireles (2007) and are represented in Table 4.2.

Table 4.2. Body numbers i and j and local coordinates of the point P (Flores, 2010)

Joint (P)	Body i	Body j	ξ_i^P [m]	η_i^P [m]	ξ_j^P [m]	η_j^P [m]
Hip	1	2	-0.294065	0.000000	0.136005	0.000000
Knee	2	3	-0.178095	0.000000	0.176707	0.000000
Ankle	3	4	-0.231393	0.000000	0.061050	0.000000

The constraint equations of the revolute joints follow the formulation of Nikravesh (1988) and can be formulated for the $\frac{1}{2}$ HAT-leg model as follows.

For the revolute joint that links body 1 to body 2:

$$\phi_1 \equiv x_1 + \xi_1^P \cos \theta_1 - \eta_1^P \sin \theta_1 - x_2 - \xi_2^P \cos \theta_2 + \eta_2^P \sin \theta_2 = 0 \quad (4.3)$$

$$\phi_2 \equiv y_1 + \xi_1^P \sin \theta_1 + \eta_1^P \cos \theta_1 - y_2 - \xi_2^P \sin \theta_2 - \eta_2^P \cos \theta_2 = 0 \quad (4.4)$$

For the revolute joint that links body 2 to body 3:

$$\phi_3 \equiv x_2 + \xi_2^P \cos \theta_2 - \eta_2^P \sin \theta_2 - x_3 - \xi_3^P \cos \theta_3 + \eta_3^P \sin \theta_3 = 0 \quad (4.5)$$

$$\phi_4 \equiv y_2 + \xi_2^P \sin \theta_2 + \eta_2^P \cos \theta_2 - y_3 - \xi_3^P \sin \theta_3 - \eta_3^P \cos \theta_3 = 0 \quad (4.6)$$

For the revolute joint that links body 3 to body 4:

$$\phi_5 \equiv x_3 + \xi_3^P \cos \theta_3 - \eta_3^P \sin \theta_3 - x_4 - \xi_4^P \cos \theta_4 + \eta_4^P \sin \theta_4 = 0 \quad (4.7)$$

$$\phi_6 \equiv y_3 + \xi_3^P \sin \theta_3 + \eta_3^P \cos \theta_3 - y_4 - \xi_4^P \sin \theta_4 - \eta_4^P \cos \theta_4 = 0 \quad (4.8)$$

In addition to these geometric constraints, the kinematic constraints associated with the guidings can also be considered. The guiding constraints are associated with the known trajectories of the bodies' CM, which can be obtained by experimental data acquisition.

For the $\frac{1}{2}$ HAT-leg model, the guided coordinates are those associated with the translation movement of body 1 (x_1 and y_1), and the rotation of all bodies ($\theta_1, \theta_2, \theta_3, \theta_4$), which were obtained experimentally (Flores, 2010; Meireles, 2007). A text file containing the discrete data of the variation of these coordinates over time is used as input. Table 4.3 shows part of these data, where the cartesian coordinates' variation with time is presented.

Table 4.3. Guiding constraints input (Flores, 2010)

Time [s]	x_1 [m]	y_1 [m]	θ_1 [rad]	θ_2 [rad]	θ_3 [rad]	θ_4 [rad]
0.0000	0.4726600	1.0799700	1.4852700	1.4433900	0.694640	1.49400
0.0290	0.5123842	1.0821876	1.5044679	1.5463198	0.645770	1.40499
0.0580	0.5506321	1.0884829	1.5152255	1.6637434	0.652280	1.43580
...
0.8990	1.7436797	1.0833713	1.3890785	1.2806636	0.941990	2.01053
0.9280	1.7911596	1.0795297	1.4136488	1.3078647	0.844440	1.79696
0.9570	1.8355846	1.0776201	1.4475594	1.3618779	0.753260	1.58027

Since the data collected experimentally of the trajectories of the bodies' CM are discrete, typically, the coordinates are interpolated along time. In this work, this procedure was executed by employing akima splines interpolation⁸.

Therefore, the guiding constraint equations for the $\frac{1}{2}$ HAT-leg model can be written as

$$\phi_7 \equiv x_1 - t_1^x(t) = 0 \quad (4.9)$$

$$\phi_8 \equiv y_1 - t_1^y(t) = 0 \quad (4.10)$$

$$\phi_9 \equiv \theta_1 - t_1^\theta(t) = 0 \quad (4.11)$$

$$\phi_{10} \equiv \theta_2 - t_2^\theta(t) = 0 \quad (4.12)$$

$$\phi_{11} \equiv \theta_3 - t_3^\theta(t) = 0 \quad (4.13)$$

$$\phi_{12} \equiv \theta_4 - t_4^\theta(t) = 0 \quad (4.14)$$

where $t_i^k(t)$, with $k = \{x, y, \theta\}$, represents the trajectory described by the CM of body i .

4.3. Initial Conditions and Kinematic Consistency

In order to initiate the dynamic analysis, at $t = t^0$, it has to be provided the initial conditions of the positions, \mathbf{q}^0 , and of the velocities, $\dot{\mathbf{q}}^0$, for every rigid body in the system. The set of initial conditions was the applied one in the work of Meireles (2007) and is showed in Table 4.4.

⁸ Akima splines interpolation refers to modified Akima piecewise cubic Hermite interpolation (MATLAB function named 'makima'). Further information about this and other interpolation methods can be found in section 4.5.1, "Polynomial Interpolation of the Experimental Data".

Table 4.4. Initial conditions of the positions and of the velocities for every rigid body in the system (Flores, 2010)

Body (<i>i</i>)	x_i^0 [m]	y_i^0 [m]	θ_i^0 [rad]	\dot{x}_i^0 [m/s]	\dot{y}_i^0 [m/s]	$\dot{\theta}_i^0$ [rad/s]
1	0.47266	1.07997	1.48527	1.38137	0.05727	0.73275
2	0.43026	0.65208	1.44339	2.05470	-0.01989	3.39980
3	0.27187	0.36231	0.69464	2.42049	0.18498	-2.07573
4	0.08941	0.15333	1.49400	1.87062	0.57264	-3.98255

The initial conditions values must satisfy the position and velocity constraint equations, defined in Eqs. (3.14) and (3.15), in order to be consistent with the kinematic structure of the biomechanical model.

The kinematic data were obtained through an experimental process that involves the acquisition and reconstruction of the three-dimensional human motion. As illustrated in Figure 4.3, the acquisition process of the kinematic input data leads to errors in the evaluation of the distances between anatomical points. Marker movement in relation to the underlying bone is caused by skin displacement and deformation which, together with the fact that anatomical joints are not perfect mechanical joints, originate kinematic inconsistency. Thus, this motion produces a violation of the kinematic constraints of the biomechanical model and is regarded as one of the most critical sources of error in dynamic analysis (Meireles, 2007; Tavares da Silva & Ambrósio, 2002).

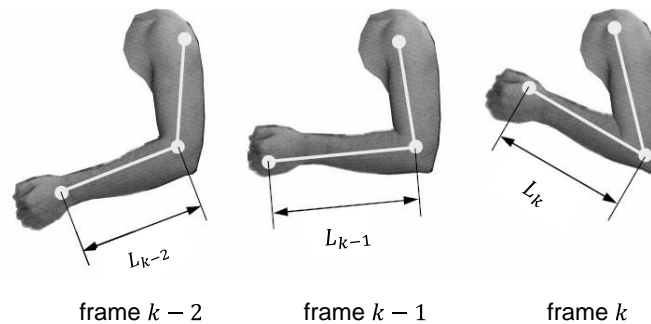


Figure 4.3. Non-constant distances between anatomical points from frame-to-frame, during the digitalization process ($L_{k-2} \neq L_{k-1} \neq L_k$) {Adapted from (Tavares da Silva, 2003)}.

To obtain a kinematically consistent input data, it is necessary to calculate a new set of cartesian coordinates of the anatomical points to ensure that the kinematic constraints are satisfied and that the distances between anatomical points remain constant throughout the analysis. In this context, it is usual to perform a previous kinematic analysis of the system positions, which Meireles (2007) had already done in his work, and which leads to a well-defined set of initial positions. This procedure goes, firstly, through using the initially non-consistent data to calculate average lengths of the rigid bodies between the

anatomical points, which are used to define the dimensions of the rigid bodies of the biomechanical model. In a second step, the filtered displacement data are used to calculate the intersegmental angles, and the position analysis is performed using these angles. Consequently, the previous kinematic analysis (illustrated in Figure 4.4) produces a new set of positions for the anatomical points, which are consistent with the kinematic structure of the biomechanical model (Alonso et al., 2007; Meireles, 2007; Tavares da Silva, 2003).

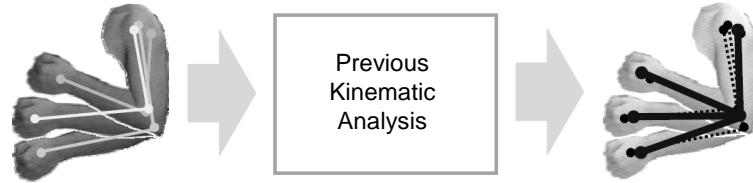


Figure 4.4. Representation of the previous kinematic analysis of the system positions {Adapted from (Meireles, 2007)}.

Once the consistent positions are established, the initial velocities of the consistent points can be obtained using direct spline differentiation. The trajectories defined by the guiding constraints were interpolated with akima splines⁹ and then, the right-hand side vector of the velocity equations, \mathbf{v} , was obtained by differentiation. Then, the yielding linear equation can be solved by any numerical algorithm. Consequently, the constraint violations at the initial time were imposed to be zero, by respecting the formulation $\dot{\Phi}^0 = 0$, that can be rewritten as,

$$0 \equiv \Phi_{\mathbf{q}} \dot{\mathbf{q}}^0 = \mathbf{v} \quad (4.15)$$

This approach assumes that the differentiation of kinematic consistent positions leads to kinematic consistent velocities. Thus, the new initial velocities of the bodies are registered on Table 4.5.

Table 4.5. Initial velocities of the bodies after the correction

Body (i)	\dot{x}_i^0 [m/s]	\dot{y}_i^0 [m/s]	$\dot{\theta}_i^0$ [rad/s]
1	1.39435745077261	0.00462284482757772	0.768965404860839
2	2.06032120913890	-0.0711425036655352	3.26653678206197
3	2.38407732408711	0.158938491420052	-2.23922425553936
4	1.79589883494986	0.576755883456152	-4.21409035268033

⁹ Akima splines interpolation refers to modified Akima piecewise cubic Hermite interpolation (MATLAB function named 'makima'). Further information about this and other interpolation methods can be found in section 4.5.1, "Polynomial Interpolation of the Experimental Data".

Furthermore, in biomechanical analyses, the motion capture system used for the data acquisition process introduces high-frequency low-amplitude noise in the acquired displacement data. This noise is inherent to the signal acquisition and the digitalization process and may also occur due to the vibrational motion of markers placed on the skin. When the raw displacement signals are differentiated, in order to obtain velocities and accelerations, this noise is amplified, which could originate significant errors in dynamic analysis. To avoid this phenomenon, it is necessary to filter the displacement signal prior to differentiation, to obtain noiseless velocities and accelerations. This process was already considered in the work of Meireles (2007) and, in this context, a low-pass Butterworth 2nd order filter with zero-phase lag was used, which has a frequency response curve that does not affect signals with a frequency lower than a selected cut-off frequency, but attenuates signals with frequencies higher than the cut-off frequency, as illustrated in Figure 4.5 (Alonso et al., 2007; Meireles, 2007).

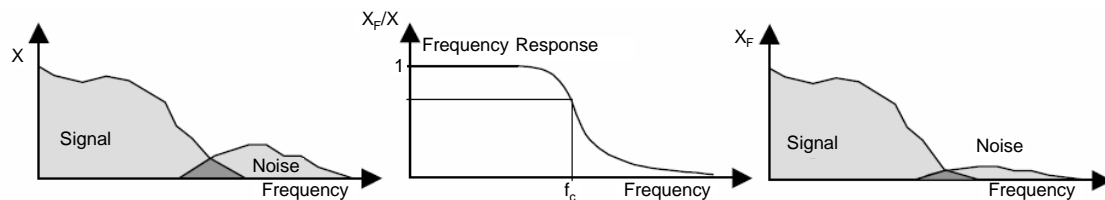


Figure 4.5. Filtering procedure using the Butterworth 2nd order, low pass filter: (a) the raw signal; (b) the frequency response curve of the filter; (c) the filtered signal {Adapted from (Tavares da Silva, 2003)}.

The selection of the cut-off frequency is not a simple process, since the use of a very high frequency, may lead to a significant part of the noise remaining with the filtered signal, and the application of a too low cut-off frequency, may attenuate too much the signal and, consequently, lose important information. The cut-off frequency typically ranges from 2 to 6 Hz, depending on cadence of the motion and the position of the anatomical landmarks. Faster movements need higher cut-off frequencies than slow movements. To estimate the amount of noise in a signal and then identify the suitable cut-off frequency, a procedure designated Residual Analysis is commonly used (Meireles, 2007; Tavares da Silva, 2003). Further information about this procedure can be found in Tavares da Silva (2003) and in Winter (2009).

4.4. External Applied Forces

The forces that are present in a biomechanical system can come from internal or external sources. Internal forces come from muscle activity, ligaments, or from friction in the muscle and joints. Conversely, external forces come from external loads, from active or passive sources (e.g., wind resistance), or from

the ground. In human gait, the main external forces acting in the body are the GRF, the inertia, and the gravitational force (Meireles, 2007).

At this point, only the force associated with gravitational field and the GRF will be considered. The gravitational force is present in all bodies, while the reaction external force, generated by the interaction between the foot and the ground during the stance period, acts only on the right foot segment (body 4). The force value and its point of application (P) vary with time. In the plane of progression, reaction forces are considered positive to the right and upward directions. The discrete data of the magnitude of the longitudinal (f_x) and vertical (f_y) components of the GRF over time, as well as the variation of the global coordinates of its point of application ($r_4^P = (x_4^P, y_4^P)$), are given as an input by a text file. Table 4.6 shows part of these data, which was also used by Meireles (2007).

Table 4.6. Ground reaction force input (Flores, 2010)

Time [s]	f_x [N]	f_y [N]	x_4^P [m]	y_4^P [m]
0.0000	0.0000	0.0000	0.0000	0.0000
0.0290	0.0000	0.0000	0.0000	0.0000
...
0.4060	-4.2000	87.1000	1.2440	0.0000
0.4350	-74.0000	192.6000	1.2910	0.0000
...
0.8990	115.6000	530.3000	1.4630	0.0000
0.9280	105.2000	377.3000	1.4700	0.0000
0.9570	65.7000	190.1000	1.4780	0.0000

According to the variation of the GRF and its point of application shown in Table 4.6, it is possible to represent the sequence of movements and the force evolution over the stride period and relate it to the gait cycle phases, as represented in the Figure 4.6.

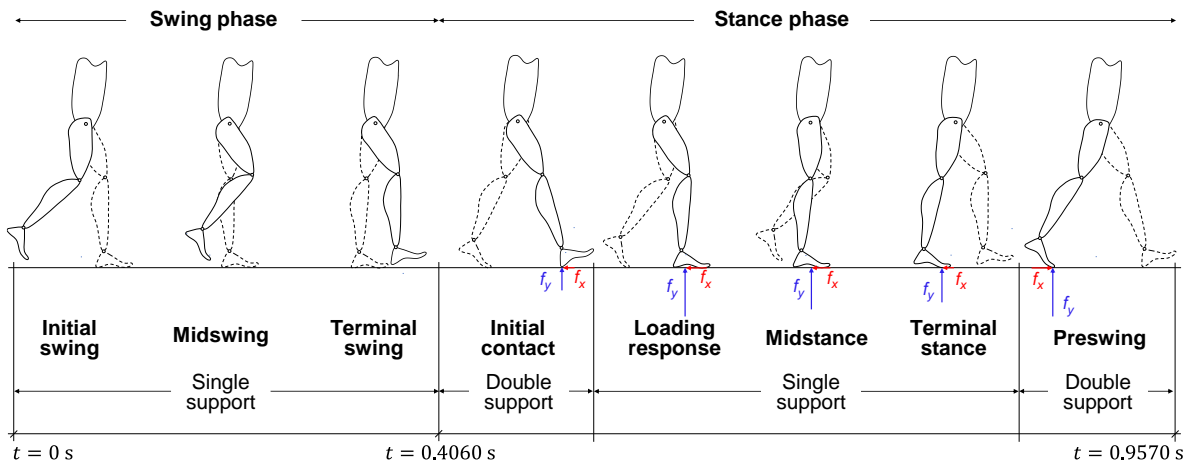


Figure 4.6. Representation of the gait cycle with the evolution of the GRF components over the stride period.

These input data represent a time period of 0.9570 s, which is related to a complete gait cycle of normal cadence. The first time period, [0.0, 0.4060] s corresponds to the swing period, where the GRF is null, and the second, [0.4060, 0.9570] s corresponds to the stance period.

The components of the applied GRF and the associated moment (n_{gr}) are transferred to the CM of the foot, as depicted in Figure 4.7.

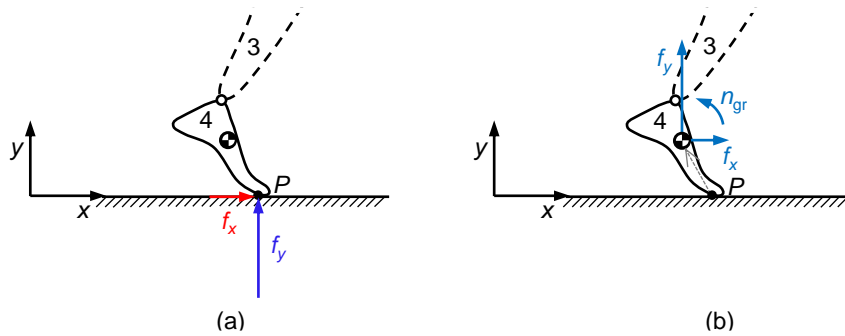


Figure 4.7. (a) Components of GRF and its point of application; (b) The transferred forces and moments to the foot's CM.

Thus, for the $\frac{1}{2}$ HAT-leg model, the generalized force vector, \mathbf{g} , which contains all external forces and moments applied on the system (GRF and gravitational force) can be defined as,

$$\mathbf{g} = \begin{pmatrix} 0 \\ -m_1 g \\ 0 \\ 0 \\ -m_2 g \\ 0 \\ 0 \\ -m_3 g \\ 0 \\ f_x \\ f_y - m_4 g \\ n_{gr} \end{pmatrix} \quad (4.16)$$

The measurement of the GRF is commonly performed using force platforms, which return typically discrete data that needs to be interpolated along time. In this work, this procedure was executed by employing akima splines interpolation¹⁰.

4.5. Results and Discussion

In this section, the main outcomes of the application of the ½ HAT-leg model to the simulation of human gait within a MATLAB code are analyzed and commented. The interpolation of the discrete data of the bodies' trajectories and the GRF components is compared using three interpolation methods. The choice of the ODE solver in MATLAB and its main characteristics are also analyzed. Furthermore, a study on the influence of the values of the Baumgarte stabilization parameters on the violation of constraints is also presented. Lastly, the computer animation of the biomechanical model developed in MATLAB, for visualization of the human gait, is described.

¹⁰ Akima splines interpolation refers to modified Akima piecewise cubic Hermite interpolation (MATLAB function named 'makima'). Further information about this and other interpolation methods can be found in section 4.5.1, "Polynomial Interpolation of the Experimental Data".

4.5.1. Polynomial Interpolation of the Experimental Data

Since the trajectory of the bodies' CM is obtained experimentally and, thus, represented by discrete data, in general, the coordinates need to be interpolated along time, in order to generate the mathematical expressions that represent the guiding constraint equations. In addition, the GRF data are obtained using force platforms and, also needs to be interpolated.

The interpolation process intends to estimate the values that lie between known data points and involves the construction of a function that matches the given data values. The type of interpolation method to use is conditioned by the characteristics of the data being fit, the required smoothness of the curve, speed considerations, among other factors. The main interpolation methods that can be employed in the MATLAB software are the cubic spline interpolation (*'spline'*), the piecewise cubic Hermite interpolation (*'pchip'*) and the modified Akima piecewise cubic Hermite interpolation (*'makima'*).

Each interpolation method differs on how the slopes of the interpolant are computed, leading to different behaviors, when the underlying data have flat areas or accentuated undulations. A comparison between these interpolation methods, concerning the MATLAB outputs, is presented in what follows.

The curves obtained from the interpolation of the guiding data, which exhibit the variation of the constrained coordinates with time, are presented in Figure 4.8. The zones with accentuated curvature were zoomed in, in two of the acquired graphs.

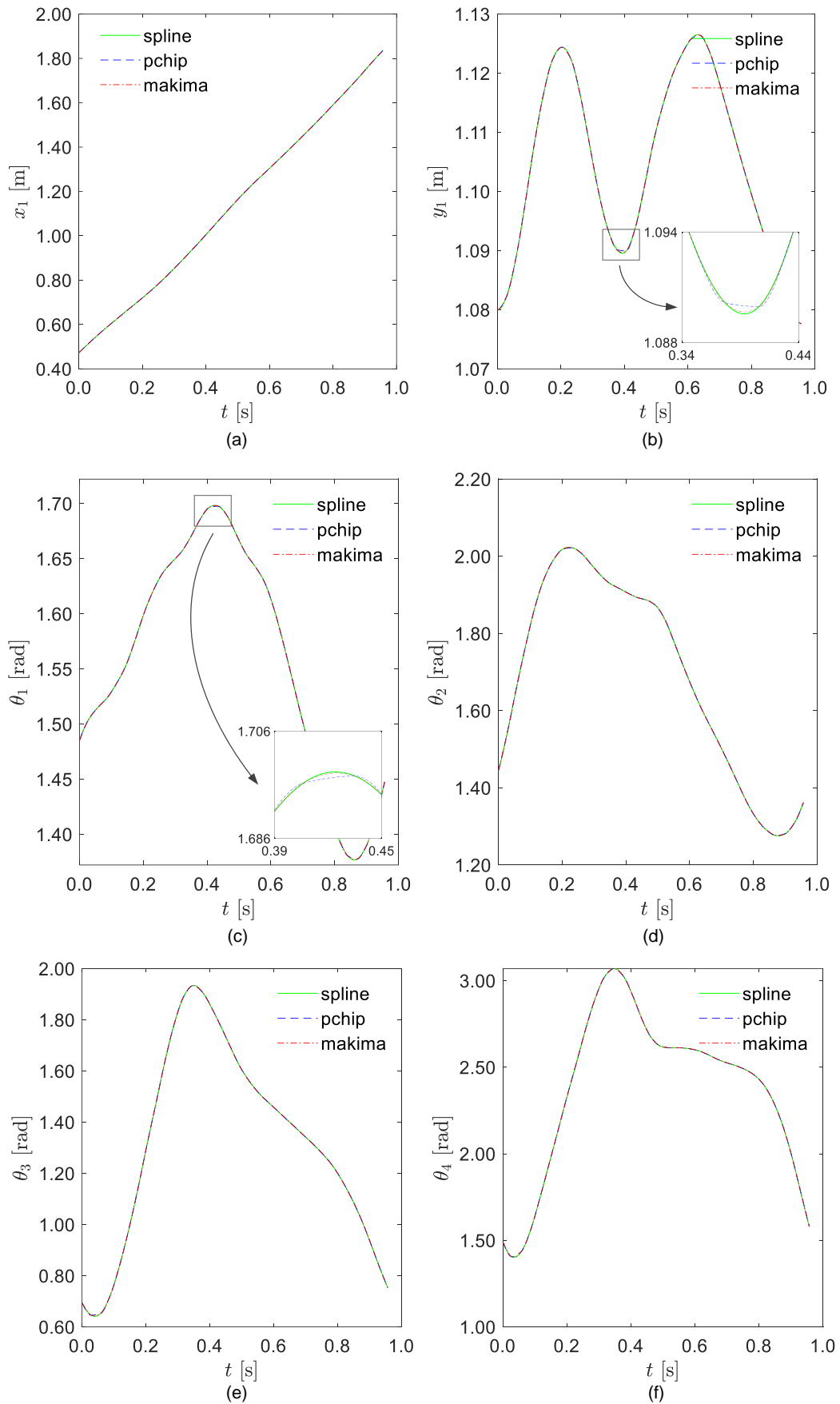


Figure 4.8. Interpolating curves of guiding data. The zone of accentuated curvature was zoomed in, in two of the graphs. The curves represent the trajectory described by the CM of the body 1 – (a) x -coordinate and (b) y -coordinate – and the variation of the orientation of the four bodies with time – (c) body 1, (d) body 2, (e) body 3, and (f) body 4.

It is possible to visualize that in the curved zones, the *'pchip'* method reduces the undulation, making those regions flatter.

Moreover, the data from the GRF file was also interpolated, and the resultant curves are presented in the Figure 4.9. A zoom was made in the regions where an abrupt variation of the variable under analysis was noticed.

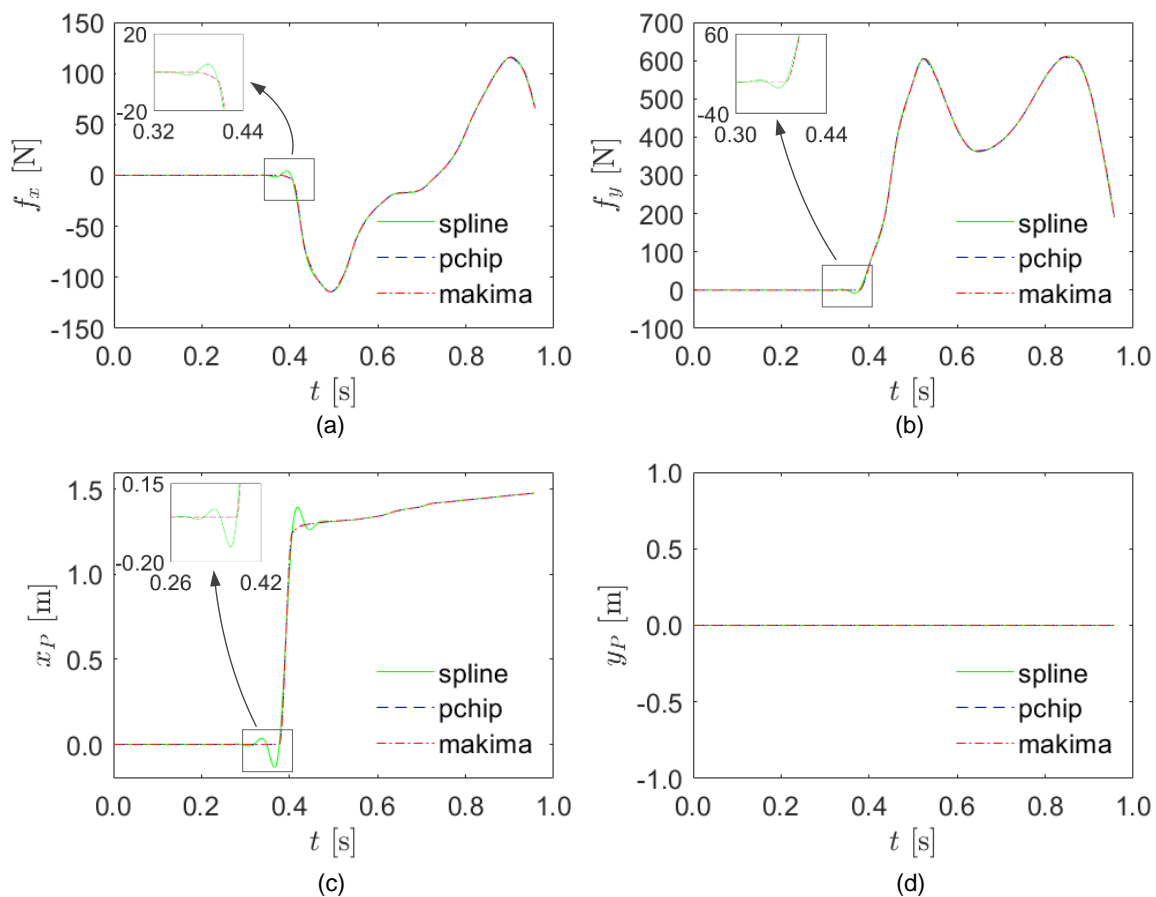


Figure 4.9. Interpolating curves of GRF data. The regions where an abrupt variation of the variable under analysis is noticed were zoomed in. (a) Longitudinal GRF evolution; (b) Vertical GRF evolution; (c) Evolution of x -coordinate of the point of application of the GRF; (d) Evolution of y -coordinate of the point of application of the GRF.

In these graphs, when the data have sudden changes, the *'spline'* interpolation method creates overshoots in the interpolating curve. These oscillations coincide with the instance of the foot-ground contact transition, i.e., when the components of GRF, f_x and f_y , are no longer zero.

In summary, regarding the graphs' outcomes, when the underlying data have oscillations, *'spline'* and *'makima'* describe the movement between points better than *'pchip'*, which is aggressively flattened near local extrema. Furthermore, *'pchip'* and *'makima'* have similar capacity to avoid overshoots and can accurately connect the flat regions. Therefore, according to the results present in Figure 4.8 and Figure 4.9, it can be concluded that *'makima'* produces better results than *'spline'* and *'pchip'*. Compared with

the *'spline'* algorithm, the *'makima'* method produces less undulations and is better suited to deal with quick changes in data. In comparison with *'pchip'*, the *'makima'* algorithm does not flatten as considerably and is, therefore, still able to deal with oscillatory data. With the *'makima'* method, the curves are smoother between points, and the regions of abrupt variation remain stable.

Additionally, the performance of these three interpolation methods can be evaluated through the simulation time. The mean of the simulation time for each interpolation method was calculated from the execution of six simulations for each. This information is resumed in Table 4.7.

Table 4.7. Simulation time for each interpolation method

	<i>'spline'</i>	<i>'pchip'</i>	<i>'makima'</i>
Simulation time (mean)	1.1172 s	3.0339 s	2.1693 s

As reported in Table 4.7, the *'spline'* method is less expensive in terms of computational time. Conversely, *'pchip'* is the interpolation method that requires more time to be executed.

To conclude, as *'makima'* reveals better results in terms of the outputs of the graphs, and the simulation time is not too high when this is the chosen method for interpolating the guiding and the GRF data, this can be considered the greatest interpolation method between the three presented.

4.5.2. Integration Algorithm for the Resolution of the Equations of Motion

In each integration time step, the accelerations vector, $\ddot{\mathbf{q}}$, and the velocities vector, $\dot{\mathbf{q}}$, are integrated, in order to obtain, respectively, the system velocities and positions for the next time step. This process is repeated until the final analysis time is reached.

A frequently used integration algorithm is the Runge-Kutta, which is an explicit algorithm that can be considered as a revised form of Taylor algorithms. As an explicit algorithm, Runge-Kutta method evaluates $y_{i+1} \equiv y(t_{i+1})$ as a function of t_i and $y_i \equiv y(t_i)$ in one step (Nikraves, 2019).

The choice of the size of the integration time step may be ambiguous, since a too large step size may cause erroneous results, and a step size too small may generate accurate results, however, increases the computational time. The size of the time step should be adjusted based on the natural frequencies of a system, which can be understood as the changing rate of the model's variables – for higher frequencies, i.e., for quickly changing events, the step size must be smaller, while for more stable variables (smaller frequencies), a bigger step size may be considered. A variable time step integrator, such as *'ode45'* in

MATLAB, is highly recommended to avoid the difficulties associated with the selection of a proper one. The *'ode45'* will automatically adjust the time step size during the course of a simulation based on the predicted highest frequency of the system (Nikravesh, 2019).

In fact, in the simulation of human gait, there are events that may require a smaller step size to be accurately characterized – such as when the contact between the foot and the ground initiates and, consequently, the model variables change rapidly –, and there are other circumstances in which a bigger step size is desirable – for example in the swing phase of the gait cycle, when the variables are more stable. If a constant step size was used, two situations could occur: on the one hand, if the step size was too big, the simulation would be faster, however, there would be a loss in accuracy; on the other hand, if a too little step size was applied, the simulation would be very long and highly computationally consuming. Therefore, the use of a variable time step solver is advantageous, in the sense that it adjusts the applied time step, according to the events that occur during the simulation of the biomechanical model.

The *'ode45'* is a versatile solver for ordinary differential equations and it is the first MATLAB solver that should be tested for most problems. However, for stiff problems or when it is required high accuracy, there are other ODE solvers that may be better suited to the problem (MathWorks, 2022a; Shampine & Reichelt, 1997).

The *'ode45'* solver is based on a Runge-Kutta integrator of 4th order with 5 stages. Solving initial value problems involves a step-by-step process (iterative process), which uses the initial condition, y_0 , as well as a period of time (time span) over which the answer is to be obtained, (t_0, t_f) . At the first time step, the initial condition provides the necessary information that allows the integration to proceed. At each time step, t_i , the solver applies a particular algorithm to the results of previous step, and the solution $y(t_i)$ is approximated by a number y_i . Since no numerical algorithm is capable of finding $y(t_i)$ exactly, the quantity $\varepsilon_i = |y(t_i) - y_i|$ is defined to represent the total error at $t = t_i$. The total error consists of two components: a truncation error, which depends on the nature of the numerical algorithm used in computing y_i , and a roundoff error, due to the finite word length in a computer. At the end of the simulation, the ODE solver returns a vector of time steps $t = [t_0, t_1, t_2, \dots, t_f]$, as well as the corresponding solution at each step $y = [y_0, y_1, y_2, \dots, y_f]$ (Dunn et al., 2005; MathWorks, 2022a; Nikravesh, 2019).

4.5.3. Baumgarte Stabilization Method

The numerical solutions of the equations of motion of constrained multibody systems often become unstable, and the constraint equations are violated due to the integration truncation errors that are added to the solutions over time. To overcome this numerical difficulty, the Baumgarte method is the most commonly applied technique. However, the choice of the feedback parameters usually involves a trial-and-error procedure.

With the objective of selecting the most appropriate parameters for this simulation, the influence of the values of the Baumgarte parameters in the violation of constraints will be analyzed.

Prior to studying the influence of the value of the feedback parameters on the constraints violation, it is convenient to analyze the global results of the dynamic simulation of one coordinate with and without considering the Baumgarte constraint stabilization method. Figure 4.10 shows the angle of the foot segment (body 4), when the equations of motion are solved with and without constraints violation stabilization.

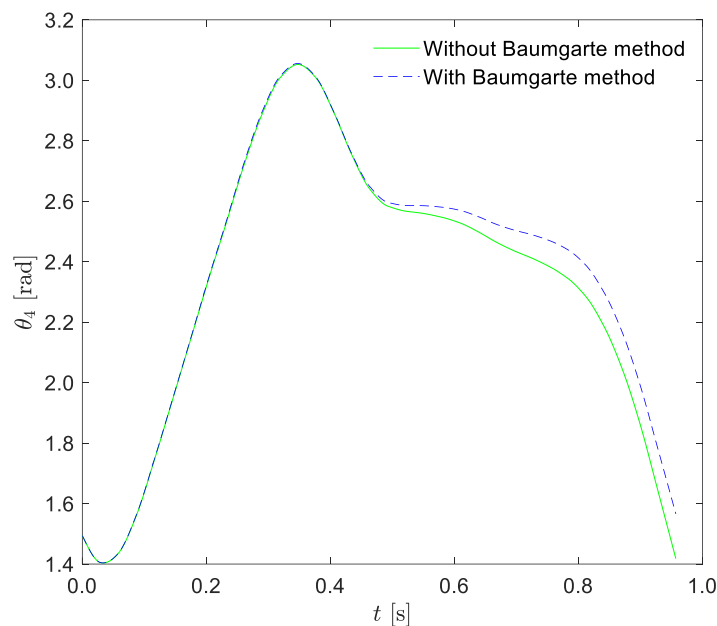


Figure 4.10. Error of the angle of the body 4 obtained with ($\alpha = 5$; $\beta = 5$) and without constraints violation stabilization.

From this outcome, it is possible to visualize that the angle of the body 4 has a small divergence, reaching an unwanted position, when there is no control on the violation of the constraints.

The effect of the values of the Baumgarte parameters was studied from the error of the position constraint equations and the error of the velocity constraint equations. The graphs presented in the Figure 4.11 show the variation of the position constraints with time for different values of α and β . In Figure

4.12, it is presented the graphs associated with the variation of the velocity constraints along time, for various values of the feedback parameters.

In the cases that the parameters α and β are equal to each other, the critical damping is reached, and after a transient phase, the first and second derivatives reach almost zero, stabilizing the system response. The violation that still exists is negligible and, consequently, the constraint equations, and not only their second derivatives – the acceleration constraint equations –, are satisfied at any given time. When the feedback parameters are different from each other, the stabilization of the response of the system takes more time, and there are oscillations around the zero value. For equal and high values of α and β , the violations are eliminated more quickly, because the applied penalization is higher. However, if the values of α and β were too high with respect to the size of the time step, the simulation might become unstable. Then, the established value for these parameters for this simulation is 20, due to its general good damping behavior and stabilization speed.

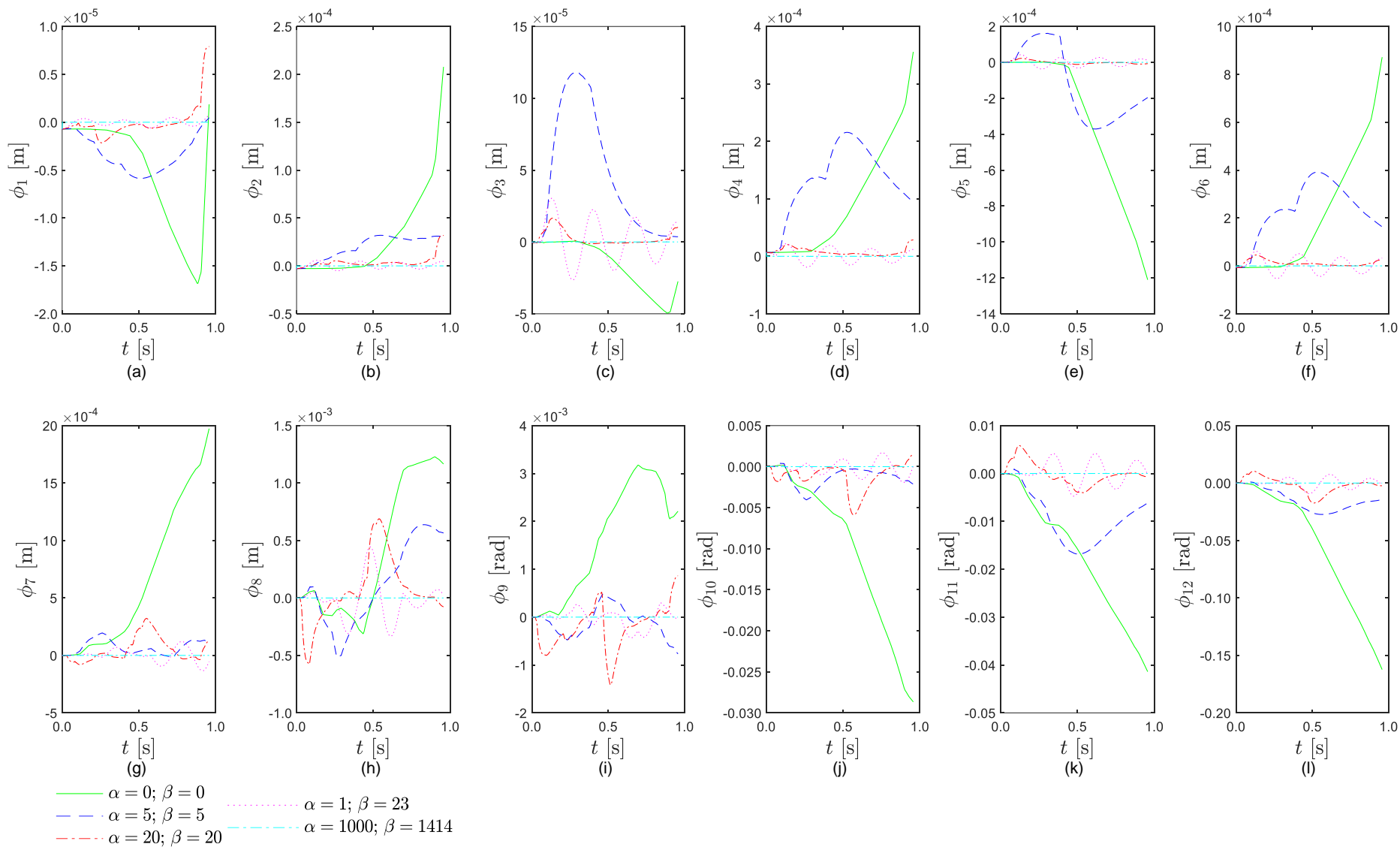


Figure 4.11. Influence of the values of the Baumgarte parameters on the error of the position constraint equations. The graphs (a) to (f) show the variation of the position constraints associated with the revolute joints with time; The graphs (g) to (l) show the variation of the position constraints associated with the guidings with time.

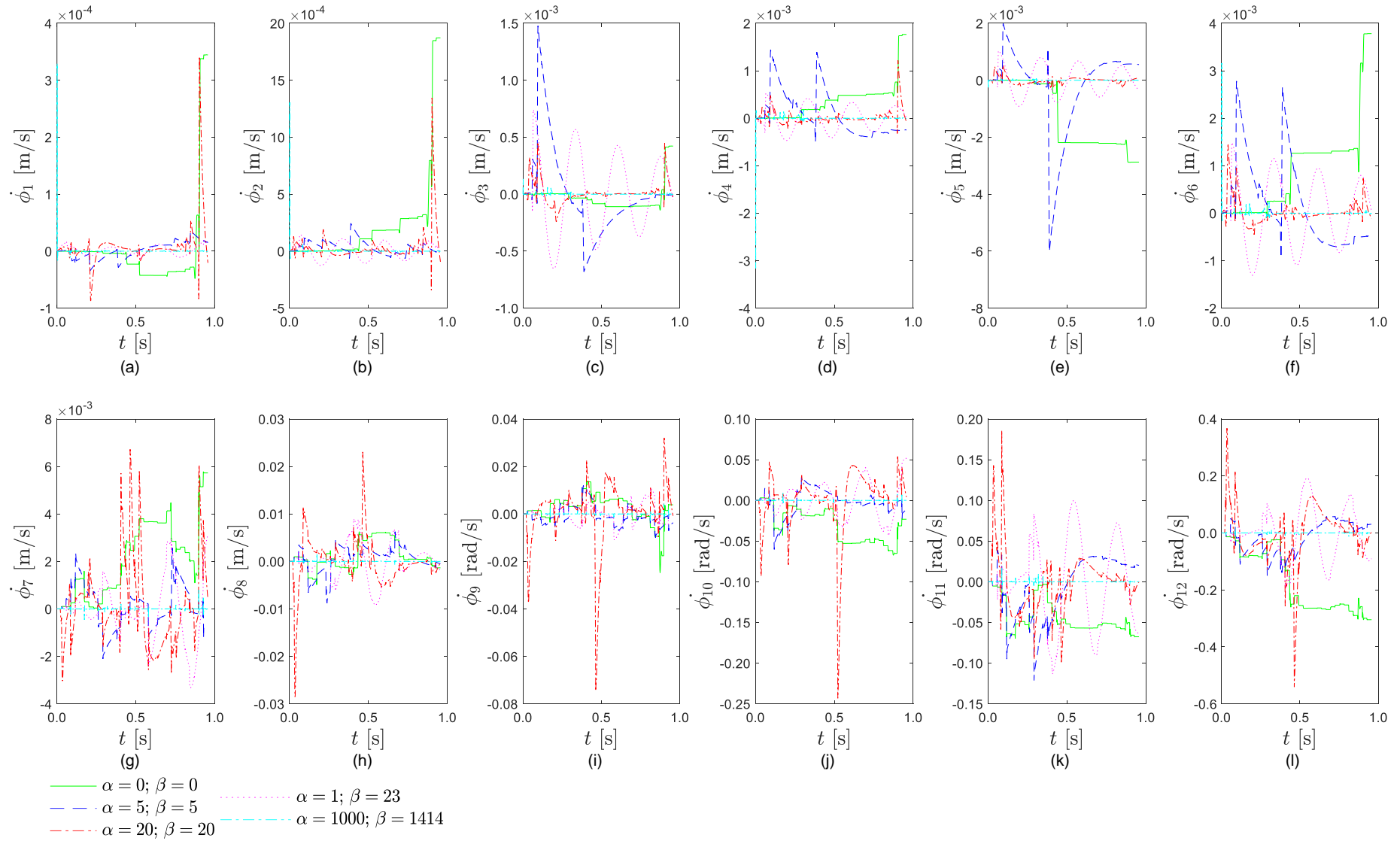


Figure 4.12. Influence of the values of the Baumgarte parameters on the error of the velocity constraint equations. The graphs (a) to (f) show the variation of the velocity constraints associated with the revolute joints with time; The graphs (g) to (l) show the variation of the velocity constraints associated with the guidings with time.

4.5.4. Motion Visualization

In order to complement the dynamic analysis of the $\frac{1}{2}$ HAT-leg multibody model, an animation of the prescribed movement was performed in MATLAB. It represents the normal human stride period, initiating with the swing phase of the gait cycle. In Figure 4.13, it is presented the initial position of the $\frac{1}{2}$ HAT-leg model.

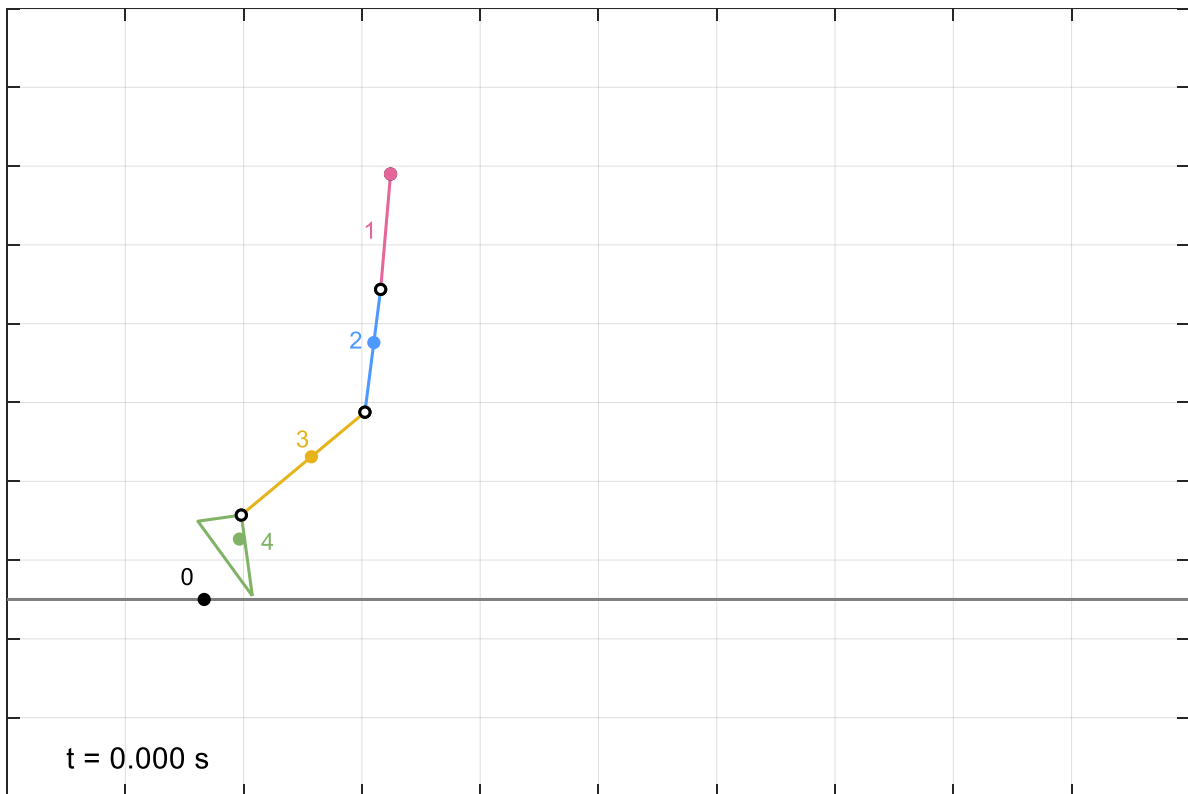


Figure 4.13. Initial position of the $\frac{1}{2}$ HAT-leg model in the MATLAB simulation.

The model constructed for performing the animation is composed by four bodies that form the right leg and HAT under analysis. These bodies were depicted by basic elements – the $\frac{1}{2}$ HAT, the thigh and the leg were represented as straight lines, while the foot was represented as a triangle. The CM of each body was depicted as a point of the same color of the respective body. It should be noticed that, only for viewing purposes, the proximal end of the $\frac{1}{2}$ HAT segment (body 1) was considered to be coincident with its CM. Furthermore, the revolute joints and the number of each anatomical segment were also represented.

On the stride animation, it is possible to visualize the intersegmental motion of the $\frac{1}{2}$ HAT-leg multibody model, the intensity of the prescribed GRF components, acting on the foot (body 4), and the trajectory of the CM of body 1, showing that guiding.

Due to the impossibility of showing the animation on paper format, an image was created with a few consecutive frames of it, taken with intervals of 0.1595 s, in order to give the perception of the gait motion and to distinguish the different phases within the stride period. This image is presented in Figure 4.14.

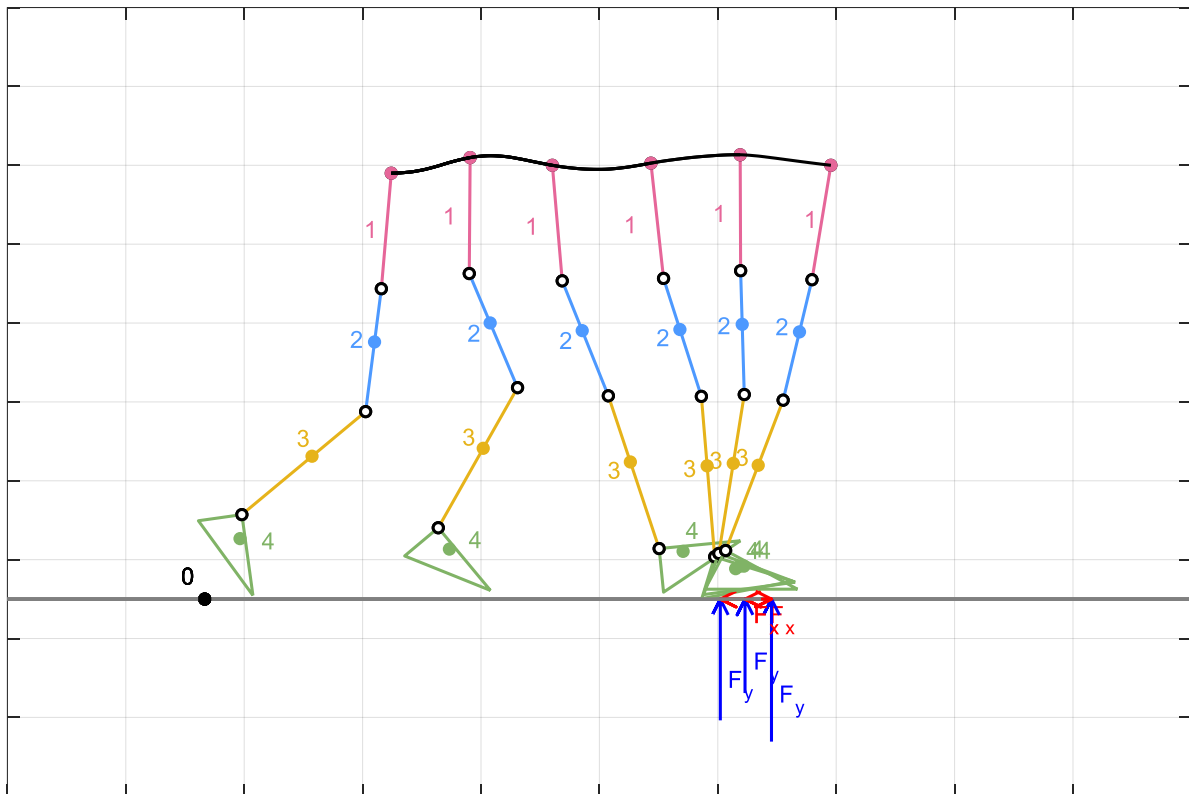


Figure 4.14. The gait cycle representation performed with the $\frac{1}{2}$ HAT-leg model in MATLAB.

4.6. Summary

In this chapter, a description of the developed multibody model was presented, namely the geometric characteristics of the rigid bodies, the connection between them by ideal revolute joints, the guidings that prescribe the motion of the bodies, and the introduction of the external forces, which in this case are the gravitational force, acting in all bodies, and the GRF, acting on body 4. The constraint equations were established and explicitly presented. All topics addressed in this chapter were implemented in a computational program developed in MATLAB.

The numerical aspects of the biomechanical model were also approached. The required set of initial conditions to initiate the dynamic analysis was prescribed and the consistency of these initial

conditions were also analyzed in order to be coherent with the kinematic structure of the biomechanical model.

Since the body's trajectory of CM and the GRF components are obtained experimentally, these discrete data were interpolated along time. In this context, three different interpolation methods were presented and compared in terms of the graphs' outcomes and the necessary simulation time.

Furthermore, a numerical solution to the equations of motion may be obtained by applying a numerical integration algorithm, as it is a dynamic problem and, therefore, it progresses with time. In the MATLAB simulation, the used integration algorithm was the '*ode45*' and the main aspects about it were covered in this chapter.

A study on the influence of the values of the Baumgarte stabilization parameters on the violation of constraints was also presented. It was concluded that the values of α and β should be equal to one another, to achieve critical damping, in order to stabilize the system response quickly. In general, for higher values of these parameters, the violations will be eliminated more quickly, because the applied penalization is higher.

Finally, the animation of the $\frac{1}{2}$ HAT-leg model developed in MATLAB was described and discussed.

Chapter 5 – Modeling of Foot-Ground Interaction

Over the last decades, there has been a growing interest in the research on contact-impact modeling and analysis in multibody dynamics (Flores, 2022). Nevertheless, it remains a difficult task to accurately model the contact mechanics when the geometric and material properties are of complex natures, such as in the case of the human foot-ground interaction.

In this chapter, the main aspects related to the modeling and simulation of contact problems under the framework of MBS are presented, and two application examples, in the context of the foot-ground interaction analysis, are described in detail and discussed. First, the fundamental aspects of the classical problem of contact mechanics are generically approached, and the methodologies that deal with contact detection and contact resolution are introduced.

It is known that the foot is the major interacting part of the human system with the surrounding environment and, therefore, contact models that describe the human foot-ground interaction are of extreme importance in biomechanical dynamic simulations (Brown & McPhee, 2018). Thus, to accurately replicate the human motion during the analysis of biomechanical multibody systems, the simulations must consider realistic representations of the foot and appropriate numerical descriptions of its interaction with the ground (Barbosa, 2017; Güler et al., 1998; Máca & Valášek, 2011; Millard et al., 2009; Millard & Kecskeméthy, 2015; Moreira et al., 2009).

In this sense, two application examples are shown in which the foot-ground interaction is studied. First, a simple leg motion is simulated with the intention of validating the methodologies of contact geometry definition and contact detection. This simulation consists of a simple drop test in which the motion of the model is generated by the action of the gravitational force.

Once the methodologies of contact geometry definition, contact detection and the application of the contact forces through constitutive laws, have been validated, the foundations for the transition to a more complex model are established, in order to validate the entire methodology of foot-ground contact analysis. Therefore, the second application example is presented, in which a multibody model of the right side of human body is used to simulate the human gait. With the purpose of correctly determining the contact forces, an optimization process is implemented to obtain the most suitable values for the geometric and contact parameters of the proposed model, and the results obtained from computational and experimental analyses are compared, with the aim of validating the proposed approach.

5.1. Generalities on Contact Problems

Contact-impact events are complex phenomena as the modeling process is strongly dependent on several factors, such as the geometry of the contacting surfaces, the local physical properties, and the numerical description of the interaction between the contacting bodies. In a simple way, the contact-impact event occurs when two or more bodies that are initially separated, collide (Flores, 2022; Flores & Lankarani, 2016; Moreira et al., 2009).

A contact problem in multibody dynamics involves the consideration of three main steps, namely: (i) the definition of the geometric properties of the contacting surfaces, (ii) the development of a contact detection methodology, (iii) the evaluation of the contact forces resulting from the collision (Flores, 2022; Flores & Lankarani, 2016; Moreira et al., 2009). The contact detection is an important task in the contact modeling process, and it is related to the verification of whether the surfaces are in contact, as the relative penetration of the bodies is allowed. The complexity of the contacting surfaces, the number of potential contact zones, and the contact kinematics influence the accuracy and efficiency of the contact detection procedure. This is one of the most time-consuming tasks, independently of the solver employed to simulate the physics of the contact process (Flores, 2022; Flores & Lankarani, 2016). As a general classification, the available methods to model the interaction between two colliding bodies can be divided into “contact force” based approaches – also referred as continuous or regularized methods –, and techniques based on “geometrical constraints” – considered non-smooth or piecewise formulations. The first method assumes that the bodies are locally deformable and the transition from non-contact to contact situations is established by a continuous function, yielding in simple and efficient solutions. Conversely, the second method considers truly rigid contacting bodies and establishes the interaction between the bodies, using kinematic unilateral constraints, to compute contact impulses or forces to prevent interpenetration from occurring (Febrer-Nafria et al., 2018; Flores, 2022; Flores & Lankarani, 2016).

Contact-impact events have a significant influence on the dynamic response of multibody systems, due to vibration, load propagation, deformations at the contact zone, energy dissipation, among other features that can limit the system operation (Flores, 2022; Skrinjar et al., 2018). In particular, the dynamic simulation of human motion is conditioned by the foot-ground contact forces, in the measure that the response of muscles, ligaments and articular reaction forces and moments is affected by them (Shourijeh & McPhee, 2015).

In this work, regularized contact force models are utilized, for which the local deformations and the contact forces are considered as continuous events and introduced into the equations of motion of the multibody systems as external generalized forces.

5.2. Contact Detection Methodology

A critical task in the contact modeling process in multibody dynamics is to verify whether the potential contact points are in contact or not. For this purpose, the relative penetration between the bodies that are potentially in contact is defined by the minimum distance between the contacting surfaces. Figure 5.1 illustrates three different scenarios between two generic contacting bodies, i and j , where the relative penetration¹¹, δ , assumes three distinct values, which allows the identification of situations of contact or non-contact – positive values of δ represent a non-contact situation, while negative values denote a contact condition; the change in sign of δ indicates a transition from non-contact to contact, or vice-versa (Flores, 2022).

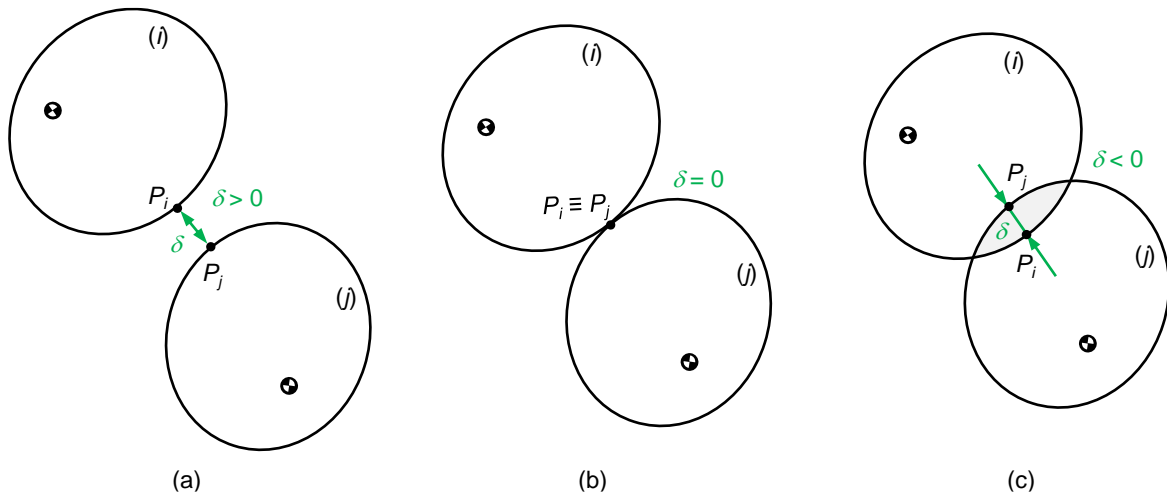


Figure 5.1. (a) Non-contact situation; $\delta > 0$; (b) Instant of the beginning or ending of contact; $\delta = 0$; (c) Contact situation, $\delta < 0$.

The generalized contact kinematics between two planar rigid bodies is described below. Figure 5.2 depicts two generic bodies, i and j , in the situation of non-contact that are moving with absolute velocities $\dot{\mathbf{r}}_i$ and $\dot{\mathbf{r}}_j$, respectively. The potential contact points present on each body are represented by P_i and P_j (Flores, 2022; Machado et al., 2012).

¹¹ Also named relative indentation, deformation or pseudo-penetration (Flores, 2022; Flores & Lankarani, 2016).

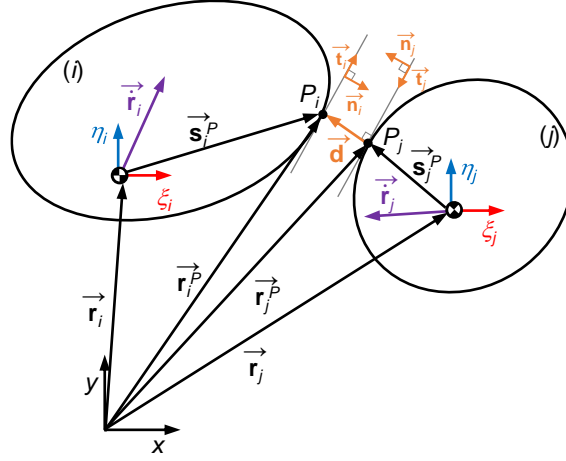


Figure 5.2. Representation of the contact between two generic bodies.

The vector that connects the two potential contact points, P_i and P_j , is a distance function that can be written as

$$\mathbf{d} = \mathbf{r}_j^P - \mathbf{r}_i^P \quad (5.1)$$

where \mathbf{r}_i^P and \mathbf{r}_j^P are the global positions of the points P_i and P_j , described in global coordinates with respect to the inertial reference frame

$$\mathbf{r}_k^P = \mathbf{r}_k + \mathbf{s}_k^P = \mathbf{r}_k + \mathbf{A}_k \mathbf{s}_k^{iP} \quad (k = \{i, j\}) \quad (5.2)$$

in which \mathbf{r}_i and \mathbf{r}_j represent the global position vectors of bodies i and j , while \mathbf{s}_i^{iP} and \mathbf{s}_j^{jP} are the local components of the contact points with respect to local coordinate systems, and \mathbf{A}_i and \mathbf{A}_j denote the rotational transformation matrices (Flores, 2022; Machado et al., 2012).

A normal vector to the plane of collision can be determined as

$$\mathbf{n} = \frac{\mathbf{d}}{d} \quad (5.3)$$

in which the magnitude of the vector \mathbf{d} is given by

$$d = \delta = \sqrt{\mathbf{d}^T \mathbf{d}} \quad (5.4)$$

The tangential vector \mathbf{t} can be obtained by a rotation of the vector \mathbf{n} in the counter-clockwise direction by 90 degrees. Moreover, \mathbf{n}_i and \mathbf{n}_j can be understood as the normal vectors belonging to the bodies i and j , respectively, and \mathbf{t}_i and \mathbf{t}_j are the tangential vectors of the bodies i and j , respectively (Flores, 2022).

The contact points must be recognized as those that correspond to maximum relative penetration, which is measured along the normal direction. Therefore, to find the potential contact points P_i and P_j

of the two colliding bodies, a set of conditions need to be satisfied: (i) the points P_i and P_j must belong to the contacting surfaces of the bodies i and j , respectively, (ii) the distance between the points P_i and P_j , given by Eq. (5.1), must correspond to the minimum distance, (iii) the vector \mathbf{d} and the normal vector \mathbf{n}_i have to be collinear, (iv) the normal vectors \mathbf{n}_i and \mathbf{n}_j must also be collinear. The conditions (iii) and (iv) can be defined as two cross products as

$$\mathbf{d} \times \mathbf{n}_i = \mathbf{0} \quad (5.5)$$

$$\mathbf{n}_i \times \mathbf{n}_j = \mathbf{0} \quad (5.6)$$

The search for the contact points must be performed at each time step of the resolution of the equations of motion of the MBS under analysis. Subsequently, the value of relative deformation can be evaluated using Eq. (5.4) (Flores, 2022; Machado et al., 2012).

The velocities of the contact points expressed with respect to the global reference frame are obtained by differentiating Eq. (5.2) with respect to time, yielding

$$\dot{\mathbf{r}}_k^P = \dot{\mathbf{r}}_k + \dot{\mathbf{A}}_k \mathbf{s}_k^P \quad (k = \{i, j\}) \quad (5.7)$$

The scalar normal, v_n , and tangential, v_t , contact velocities are obtained by projecting the relative velocity of the contact points, $\dot{\mathbf{r}}_i^P$ and $\dot{\mathbf{r}}_j^P$, onto the normal and tangential directions of the contacting surfaces, and are given by

$$v_n = \dot{\delta} = (\dot{\mathbf{r}}_j^P - \dot{\mathbf{r}}_i^P)^T \mathbf{n} \quad (5.8)$$

$$v_t = (\dot{\mathbf{r}}_j^P - \dot{\mathbf{r}}_i^P)^T \mathbf{t} \quad (5.9)$$

The normal relative contact velocity between the contact points – penetration velocity – establishes whether the colliding bodies are approaching or separating. Positive values of v_n denote that the bodies are approaching, which corresponds to the compression phase, while negative values of v_n indicate that the bodies are separating, which corresponds to the restitution phase. On the other hand, the tangential relative contact velocity defines whether the contacting bodies are sliding or sticking, which are important aspects in the friction analysis in multibody dynamics (Flores, 2022; Machado et al., 2012).

The computational efficiency and accuracy of contact detection process strongly depends on the complexity of the colliding surfaces, the number of potential contacting points, and the kinematics of the bodies. It should be noticed that the contact detection phase requires, generally, a great computational effort due to the iterative nature of the numerical procedure utilized (Flores, 2022).

5.3. Contact Resolution Approach

In the framework of multibody systems, the resolution of a contact problem involves two main steps – the contact forces evaluation and the introduction of those forces into the equations of motion as external generalized forces (in vector \mathbf{g}). The components of contact forces that act at the contact points, and the associated moments, are transferred to the CM of the colliding bodies, as shown in Figure 5.3 (Flores, 2022).

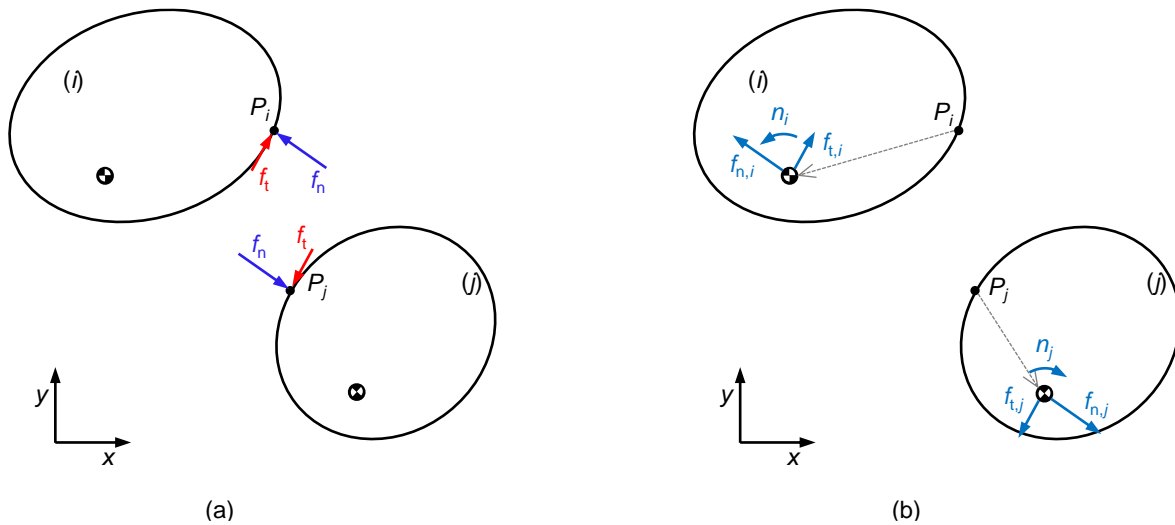


Figure 5.3. (a) Components of contact forces and respective points of application; (b) The transferred forces and moments to the bodies' CM.

When regularized contact force models are utilized, the contact forces are evaluated using appropriate constitutive laws, for which the local deformations and the forces are considered as continuous events. The processes of storage and dissipation of energy during the contact period are usually modeled using spring and damper elements. For most of the typical applications in the context of MBS, the normal and tangential components of contact force are calculated from adaptations to Hertz's contact theory (Hertz, 1881) and to Coulomb's law (Coulomb, 1785), respectively (Flores, 2022; Flores & Lankarani, 2016).

Regarding the evaluation of normal contact forces, Hooke's law is the simplest and oldest contact model, and it is characterized by a linear spring element, which represents the contacting surfaces elasticity. This linear contact model can be expressed as

$$f_n = k\delta \quad (5.10)$$

where k is the spring stiffness associated with the geometric and material characteristics of the contacting bodies, and δ represents the relative penetration between the colliding surfaces. A major disadvantage of

this approach is that it does not take into account the energy dissipated during the contact event (Flores, 2022; Flores & Lankarani, 2016).

Additionally, one of the most popular contact force models is the one proposed by Hertz (Hertz, 1881), which considers a nonlinear relation between force and pseudo-penetration, as

$$f_n = k\delta^n \quad (5.11)$$

where n is the nonlinear exponent factor, which is determined based on the material and geometrical properties of the local region of the bodies in contact, and is typically equal to $3/2$. Similarly to Hooke's law, the nonlinear Hertz contact force model does not allow prediction of the energy dissipated during the contact process (Flores, 2022; Flores & Lankarani, 2016; Hertz, 1881; Rodrigues da Silva et al., 2022; Skrinjar et al., 2018).

One of the first contact force model that accounts for the energy dissipation during contact events is the Kelvin-Voigt model, which is modeled as a linear spring and a linear damper arranged in parallel, and can be expressed as

$$f_n = k\delta + D\dot{\delta} \quad (5.12)$$

where the parameter D represents the damping coefficient and $\dot{\delta}$ is the normal component of the relative contact velocity. The first parcel on the right-hand side is the elastic force component, and the second parcel refers to the dissipative force term. This contact model has some limitations, namely the fact that it does not represent the nonlinearity of the whole contact process; the presence of contact forces when the penetration is null, due to the damping term; and the production of negative forces at the end of contact, which is not appropriate from a physical point of view, since the colliding bodies cannot attract each other (Flores, 2022; Flores & Lankarani, 2016; Skrinjar et al., 2018).

In addition, with the intention of overcoming the limitation of not representing the energy loss during the contact process, associated with pure elastic contact force models, other models were developed as an extension to the Hertz contact law to comprise energy dissipation in the form of internal damping (Flores, 2022; Flores & Lankarani, 2016).

The contact model proposed by Hunt and Crossley (Hunt & Crossley, 1975) is based on Hertz's approach, including a nonlinear spring, with the addition of a nonlinear viscoelastic element (damper), arranged in parallel. It can be written as

$$f_n = k\delta^n \left[1 + \frac{3(1-c_r)}{2} \frac{\dot{\delta}}{\dot{\delta}^{(-)}} \right] \quad (5.13)$$

where the first term represents the nonlinear elastic Hertz's law and the second term is the dissipative parcel, in which c_r is the coefficient of restitution and $\dot{\delta}^{(-)}$ represents the normal contact velocity at the initial instant of impact (Flores, 2022; Flores & Lankarani, 2016; Hertz, 1881; Rodrigues da Silva et al., 2022; Skrinjar et al., 2018).

Additionally, the nonlinear Lankarani and Nikravesh contact force model (Lankarani & Nikravesh, 1990) is one of the most popular approaches to model contact events under the context of multibody dynamics. It is an adaptation of the Hertzian contact theory (Hertz, 1881) and it is based on the damping approach by Hunt and Crossley (Hunt & Crossley, 1975), accounting for the kinetic energy lost due to the internal damping (Flores, 2022; Flores & Lankarani, 2016; Rodrigues da Silva et al., 2022; Skrinjar et al., 2018). It can be written as

$$f_n = k\delta^n \left[1 + \frac{3(1-c_r^2)}{4} \frac{\dot{\delta}}{\dot{\delta}^{(-)}} \right] \quad (5.14)$$

More recently, Ambrósio and Pombo (2018) proposed a new contact model for evaluating the normal contact force, which can be expressed as

$$f_n = \begin{cases} k\delta^n c_r & \text{if } \dot{\delta} \leq -v_{0,n} \\ k\delta^n [c_r + (1-c_r)(3R^2 - 2R^3)] & \text{if } -v_{0,n} < \dot{\delta} < v_{0,n} \\ k\delta^n & \text{if } \dot{\delta} \geq v_{0,n} \end{cases} \quad (5.15)$$

in which

$$R = \frac{\dot{\delta} + v_{0,n}}{2v_{0,n}} \quad (5.16)$$

where $v_{0,n}$ is the penetration velocity tolerance. This constitutive law is based on the Hertz contact model (Hertz, 1881), in which the energy dissipation is considered. In this viscoelastic contact model, the coefficient of restitution is employed to distinguish between the contact force during the compression and restitution phases, and a tolerance velocity is included to smooth the contact force discontinuity in the transition between both phases. Therefore, when $\dot{\delta}$ is greater than, or equal to $v_{0,n}$, it is considered that the bodies are approaching, which corresponds to the compression phase. On the other hand, if $\dot{\delta}$ is less than, or equal to $-v_{0,n}$, it indicates that the bodies are separating, corresponding to the restitution phase. When $\dot{\delta}$ takes place between $-v_{0,n}$ and $v_{0,n}$, a transition function is employed, in which the R factor equals 0 when $\dot{\delta}$ approaches $-v_{0,n}$, and is equal to 1 when $\dot{\delta}$ gets closer to $v_{0,n}$ (Ambrósio & Pombo, 2018; Marques et al., 2020).

A contact-impact event encompasses not only the generation of normal contact forces, but also the production of tangential forces, called friction forces, which act in the opposite direction of the local relative velocity. The most commonly applied tangential force model is the Coulomb friction law (Coulomb, 1785), which can be expressed as

$$f_t = \mu f_n \operatorname{sgn}(v_t) \quad (5.17)$$

with

$$\operatorname{sgn}(v_t) = \begin{cases} -1 & \text{if } v_t < 0 \\ 1 & \text{if } v_t > 0 \end{cases} \quad (5.18)$$

where μ expresses the Coulomb coefficient of friction, f_n denotes the normal contact force, and v_t is the tangential relative velocity. In the recent decades, this model has been subjected to modifications and improvements, in order to avoid the discontinuity present at null relative tangential velocity and to obtain a continuous friction force (Brown, 2017; Flores, 2022; Flores et al., 2006).

Recently, a smoothed Coulomb friction law was implemented in the work of Miller et al. (2012), for evaluating the tangential contact force. It can be written as

$$f_t = -\mu f_n \tanh\left(\frac{v_t}{v_0}\right) \quad (5.19)$$

in which v_0 is a tolerance velocity to smooth friction transition (Miller et al., 2012).

Moreover, in this work, a different constitutive law is proposed for the tangential contact force evaluation, which includes a smoothed Coulomb friction law (Coulomb, 1785), utilized in the work of Miller et al. (2012), and the addition of a viscous friction component (Moreira, 2009). Hence, the global friction force can be evaluated as

$$f_t = -\mu_c f_n \tanh\left(\frac{v_t}{v_{0,t}}\right) - \mu_d v_t \quad (5.20)$$

where μ_c represent the Coulomb friction coefficient, μ_d expresses the viscous friction coefficient and $v_{0,t}$ is a tolerance velocity to smooth friction transition. The viscous friction component is considered to take into account the presence of a lubricated surface, and is characterized by a linear increase in friction with respect to velocity (Brown, 2017; Moreira, 2009).

5.4. Application Example 1: Leg Drop Motion

In this section, a simple leg motion is simulated with the intention of validating the methodologies of contact geometry definition and contact detection. The simulation consists of a simple drop test in which the gravitational force is the only external force applied to the model (Moreira, 2009).

Biomechanical Model Description

For this purpose, the biomechanical model represented in Figure 5.4 – the leg-foot model – is used. This model was developed within a MATLAB computer code, using the multibody formulation with cartesian coordinates, described in Chapter 3.

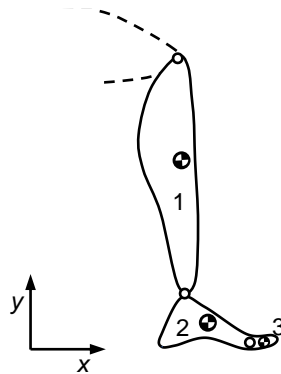


Figure 5.4. Leg-foot model representation.

A brief description of the leg-foot model is provided as follows: the model is composed of three rigid bodies – leg, main foot part and toes, from the right side of the human body – and the generalized coordinates vector, \mathbf{q} , is defined by nine coordinates ($n = 9$) since the model has three movable bodies with three DOF each. These bodies, their anatomical description and their masses and moments of inertia are summarized in Table 5.1. The data are representative of a male of 1.70 m and 70 kg, and were obtained from the work of Moreira (2009). The bodies are connected by three revolute joints and, consequently, six constraints are added to the system, since each joint removes two DOF from the system. Furthermore, for simplification, the metatarsophalangeal joints are considered to be fixed, adding one constraint to the system and, consequently, removing one DOF. Therefore, the leg-foot MBS has a total of two DOF, that correspond to two rotations about revolute joints – one DOF for knee flexion-extension and one DOF for ankle dorsiflexion-plantarflexion.

Table 5.1. Mass and moment of inertia of each segment of the leg-foot model (Moreira, 2009)

Body	Anatomical description	Mass [kg]	Moment of Inertia [kg.m ²]
1	right leg	4.760	8.230×10 ⁶
2	right main foot part	1.330	2.250×10 ⁶
3	right toes	0.350	0.471×10 ⁶

Each rigid body i has a local reference frame attached to it, with its origin located at the CM of the body. The ξ_i is aligned with the segment, while the η_i is perpendicular to the segment's extension, as depicted in Figure 5.5.

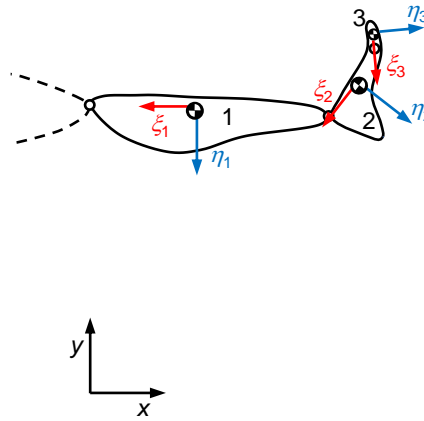


Figure 5.5. Representation of the local reference frames on the leg-foot model in the initial position.

The local coordinates of each revolute joint (denoted by the point P) on the constrained bodies i and j are defined in Table 5.2.

Table 5.2. Body numbers i and j and local coordinates of each revolute joint (point P)

Joint (P)	Body i	Body j	ξ_i^P [m]	η_i^P [m]	ξ_j^P [m]	η_j^P [m]
Knee	0	1	0	0	0.176707	0
Ankle	1	2	-0.231393	0	0.041378	0
MTP joints	2	3	-0.114014	0	0.027200	0

The constraints equations of the revolute joints follow the formulation of Nikravesh (1988) and can be formulated for the leg-foot model as follows.

For the knee joint:

$$\phi_1 \equiv x_1 + \xi_1^P \cos \theta_1 - \eta_1^P \sin \theta_1 = 0 \quad (5.21)$$

$$\phi_2 \equiv y_1 + \xi_1^P \sin \theta_1 + \eta_1^P \cos \theta_1 - y_1^0 = 0 \quad (5.22)$$

For the ankle joint:

$$\phi_3 \equiv x_1 + \xi_1^P \cos \theta_1 - \eta_1^P \sin \theta_1 - x_2 - \xi_2^P \cos \theta_2 + \eta_2^P \sin \theta_2 = 0 \quad (5.23)$$

$$\phi_4 \equiv y_1 + \xi_1^P \sin \theta_1 + \eta_1^P \cos \theta_1 - y_2 - \xi_2^P \sin \theta_2 - \eta_2^P \cos \theta_2 = 0 \quad (5.24)$$

For the metatarsophalangeal joints:

$$\phi_5 \equiv x_2 + \xi_2^P \cos \theta_2 - \eta_2^P \sin \theta_2 - x_3 - \xi_3^P \cos \theta_3 + \eta_3^P \sin \theta_3 = 0 \quad (5.25)$$

$$\phi_6 \equiv y_2 + \xi_2^P \sin \theta_2 + \eta_2^P \cos \theta_2 - y_3 - \xi_3^P \sin \theta_3 - \eta_3^P \cos \theta_3 = 0 \quad (5.26)$$

In addition to these geometric constraints, it is defined another one for the fixed MTP joints:

$$\phi_7 \equiv \theta_3 - \theta_2 - (\theta_3^0 - \theta_2^0) = 0 \quad (5.27)$$

The simulation starts with the leg in a horizontal position with zero velocity. The set of initial conditions for the positions, \mathbf{q}^0 , and for the velocities, $\dot{\mathbf{q}}^0$, for every rigid body in the system is shown in Table 5.3. The initial arrangement of the segments of the biomechanical model is depicted in Figure 5.5

Table 5.3. Initial conditions of the positions and of the velocities for every rigid body in the system

Body (<i>i</i>)	x_i^0 [m]	y_i^0 [m]	θ_i^0 [rad]	\dot{x}_i^0 [m/s]	\dot{y}_i^0 [m/s]	$\dot{\theta}_i^0$ [rad/s]
1	0.176707	0.4847	π	0	0	0
2	0.4285	0.5207	4.19694	0	0	0
3	0.4847	0.6471	$\frac{3\pi}{2}$	0	0	0

When using geometrically ideal joints, the admissible range of motion prescribed for the human articulations – described in Section 2.1 – can be easily violated since no additional constraints are introduced for preventing those joints from achieving physically unacceptable positions. A joint resistance moment is introduced in the leg-foot model to prevent the occurrence of unfeasible positions of the ankle joint and to simulate the muscle passive behavior, introducing some energy dissipation at the joint level. The joint resistance moment is modeled using a viscous torsional damper – dissipative term, $m^{(d)}$, – and a nonlinear torsional spring – motion-limiting or penalty term, $m^{(p)}$, – positioned at the ankle joint, which is depicted in Figure 5.6, and can be described as

$$m^{(r)} = m^{(d)} + m^{(p)} \quad (5.28)$$

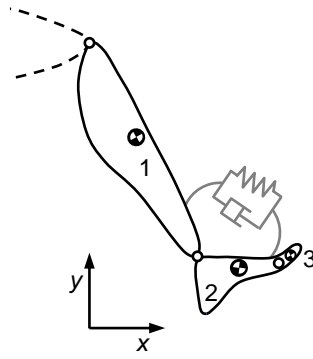


Figure 5.6. Joint resistance moment modeled using a system of nonlinear spring and damper.

The dissipative term is responsible for simulating the passive action of muscles, allowing some energy dissipation at the ankle joint. Its action intends to resist the motion of the joint and can be calculated as

$$m^{(d)} = -j\dot{\beta} \quad (5.29)$$

where $\dot{\beta}$ is the relative angular velocity vector between the bodies 1 and 2, and j is the damping coefficient (Tavares da Silva, 2003; Tavares da Silva et al., 1997).

The motion-limiting term defines a moment that has a nonlinear behavior, which is null during normal joint rotation, and increases rapidly from zero to a maximum value, whenever an unacceptable ankle position is detected (Tavares da Silva, 2003; Tavares da Silva et al., 1997). This behavior is illustrated in the Figure 5.7.

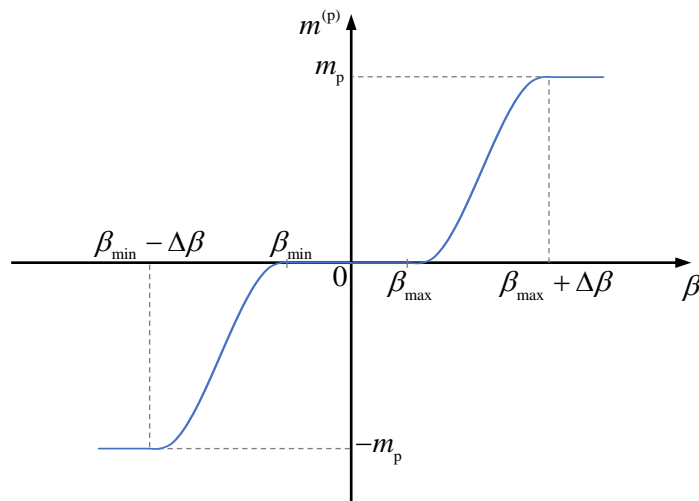


Figure 5.7. Nonlinear behavior of the joint motion-limiting moment.

In order to define the area of feasible motion, wherein the foot can move without displacement of the leg, it is defined a local frame centered in the ankle joint and rigidly attached to the leg. This frame is defined using the unit vectors \mathbf{v}_i and \mathbf{v}_{i2} . Furthermore, a unit vector \mathbf{v}_j positioned in the ankle joint and rigidly attached to the main foot part is also established. This vector defined on the foot moves in relation to the frame present in the leg, and consequently, it is possible to calculate the angle of rotation between the two (Figure 5.8). In the neutral position, the angle (β) will be zero, i.e., \mathbf{v}_j and \mathbf{v}_i will be coincident.

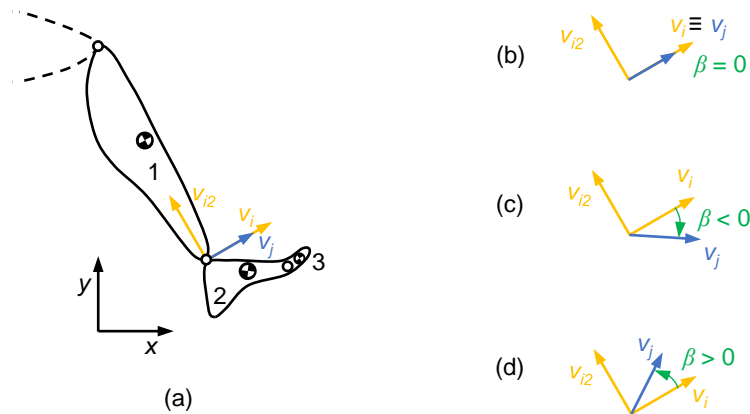


Figure 5.8. (a) Representation of the leg's frame (\mathbf{v}_i , \mathbf{v}_{i2}) and the foot's vector (\mathbf{v}_j); (b) Vectors configuration in neutral position of the ankle; (c) Vectors configuration in plantarflexion of the ankle; (d) Vectors configuration in dorsiflexion of the ankle.

If the registered angle (β) exceeds the ankle range of motion, i.e., the maximum allowable angle of that joint (β_{\min} for plantarflexion and β_{\max} for dorsiflexion), then an unacceptable position is occurring, and a motion-limiting moment is applied (Tavares da Silva, 2003; Tavares da Silva et al., 1997). This penalty moment can be formulated as follows

$$m^{(p)} = \begin{cases} -m_p & \text{if } \beta \leq \beta_{\min} - \Delta\beta \\ -m_p \left[3 \left(\frac{\beta - \beta_{\min}}{\Delta\beta} \right)^2 - 2 \left(\frac{\beta - \beta_{\min}}{\Delta\beta} \right)^3 \right] & \text{if } \beta_{\min} - \Delta\beta < \beta < \beta_{\min} \\ 0 & \text{if } \beta_{\min} \leq \beta \leq \beta_{\max} \\ m_p \left[3 \left(\frac{\beta - \beta_{\max}}{\Delta\beta} \right)^2 - 2 \left(\frac{\beta - \beta_{\max}}{\Delta\beta} \right)^3 \right] & \text{if } \beta_{\max} < \beta < \beta_{\max} + \Delta\beta \\ m_p & \text{if } \beta \geq \beta_{\max} + \Delta\beta \end{cases} \quad (5.30)$$

Table 5.4 displays the ankle joint resistance data adopted in this work. The joint range of motion is obtained from Table 2.1 (Tavares da Silva, 2003; Tavares da Silva et al., 1997).

Table 5.4. Joint resistance data (Tavares da Silva, 2003; Tavares da Silva et al., 1997)

Joint	β_{\min} [°]	β_{\max} [°]	$\Delta\beta$ [°]	m_p [N.m]	j [N.m.s]
Ankle	-35.0	20.0	11.5	226.0	0.1

The simulation consists of a simple drop test originated only by the gravitational force applied to the model. When contact between the foot and the level ground is detected, the contact forces generated using a continuous force model are also applied to the main foot part (Moreira, 2009).

As a result of the application of these forces, for the leg-foot model, the generalized force vector, \mathbf{g} , which contains all external forces and moments applied on the system (gravitational force, $-m\mathbf{g}$, joint resistance moment, $m^{(r)}$, ground reaction force, f_n and f_t , and ground reaction moment, n_{gr}) can be defined as

$$\mathbf{g} = \begin{Bmatrix} 0 \\ -m_1 g \\ m^{(r)} \\ f_t \\ f_n - m_2 g \\ n_{gr} - m^{(r)} \\ 0 \\ -m_3 g \\ 0 \end{Bmatrix} \quad (5.31)$$

Foot-Ground Contact Model

In this study, for this example of application, the geometric description of the foot is made, in a first and simpler approach, by two points of contact (Figure 5.9 (a)), followed by the definition of two circles in a second and more realistic approach (Figure 5.9 (b)).

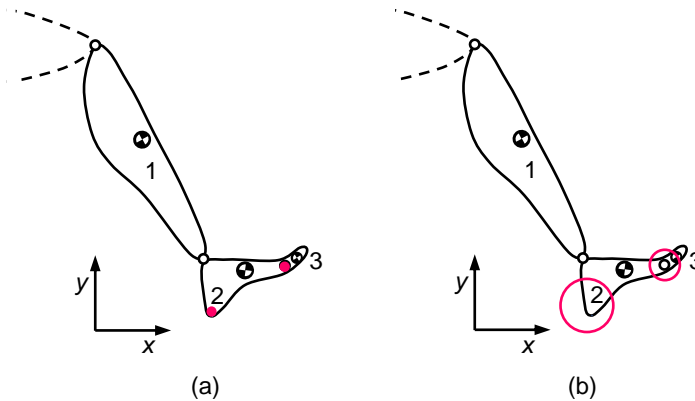


Figure 5.9. Representation of the contact geometry adopted in (a) the first approach (two points); and in (b) the second approach (two circles).

The two contact points are positioned at the heel and at the MTP joints of the foot, as seen in Figure 5.9 (a). The local coordinates of each contact point (denoted by P_1 and P_2) on the main foot part, body 2, as well as the contact parameters – namely the nonlinear exponent factor, n , the contact stiffness, k , the coefficient of restitution, c_r , the friction coefficient, μ , and the tolerance velocity, v_0 , – are defined in Table 5.5.

Table 5.5. Contact parameters and local coordinates of contact points (P_1 and P_2) on the main foot part (body 2)

	Heel (P_1)	MTP joints (P_2)
ξ_2^P [m]	0.050953	-0.114014
η_2^P [m]	0.093458	0.0
n [-]	3/2	3/2
k [N/m ^{3/2}]	40000	40000
c_r [-]	0.7	0.7
μ [-]	0.8	0.8
v_0 [m/s]	0.01	0.01

The interaction between the foot and the ground is performed by evaluating, at each time step, the potential contacts between the defined points and the ground, as the relative penetration of the bodies is allowed. As the contact is defined simply by contact points, and the ground is considered to be flat and leveled, the pseudo-penetration, δ , for each contact point, can be understood as the opposite of the y -global coordinate of that point (denoted by the generic point P), i.e.,

$$\delta = -y^P \quad (5.32)$$

If a negative value of y^P is registered, then δ has a positive value, and it can be assumed that there is contact between the foot and the ground.

The constitutive laws associated with the normal and tangential forces developed during the contact are a function of the geometrical and material properties of the foot and the ground, the inter-penetration between the foot and the ground and the relative contact velocities in both normal and tangential directions (Flores & Lankarani, 2016).

Regarding the normal contact force evaluation, the nonlinear Lankarani and Nikravesh contact model (Lankarani & Nikravesh, 1990), presented on Eq. (5.14), was used. The evaluation of tangential contact force is performed with a smoothed Coulomb friction law (Coulomb, 1785), implemented in the work of Miller et al. (2012), which is expressed in Eq. (5.19).

The number of points, their locations, the contact parameters, and the continuous force models to be used can be adjusted by the user. It should be noticed that the definition of these properties must take into consideration the anatomy and the biomechanics of the foot, i.e., the contact geometry must be defined according to the most relevant foot areas for human locomotion.

Regarding the geometry of the foot, the second approach involved the definition of two circles positioned at the heel and MTP joints of the right foot, as seen in Figure 5.9 (b). The local coordinates of the circles' centers (denoted by C_1 and C_2) on the main foot part, body 2, their radius, r , as well as the contact parameters – namely the nonlinear exponent factor, n , the contact stiffness, k , the coefficient of restitution, c_r , the Coulomb friction coefficient, μ_c , the viscous friction coefficient, μ_d , and the tolerance velocities, v_0 , – are defined in Table 5.6.

Table 5.6. Contact and geometric parameters of contact circles

	Heel (C_1)	MTP joints (C_2)
ξ_2^C [m]	0.058346	-0.114014
η_2^C [m]	0.080407	0.0
r [m]	0.030	0.015
n [-]	3/2	3/2
k [N/m ^{3/2}]	40000	40000
c_r [-]	0.2	0.2
μ_c [-]	0.8	0.8
μ_d [N.s/m]	3	3
$v_{0,n}$ [m/s]	0.01	0.01
$v_{0,t}$ [m/s]	0.01	0.01

As the contact is defined by contact circles, and the ground is considered to be flat and leveled, the relative penetration of the circles into the plane of ground, δ , for each contact circle, can be understood as the difference between the radius of the circle and the y -global coordinate of that circle center (denoted by the generic point C), i.e.,

$$\delta = r - y^C \quad (5.33)$$

If a positive value of δ is registered, then it can be assumed that there is contact between the foot and the ground.

In this approach, the normal contact force is evaluated using the contact model proposed by Ambrósio and Pombo (2018), described in Eq. (5.15). For the tangential contact force evaluation, the implemented constitutive law includes a smoothed Coulomb friction law (Coulomb, 1785), utilized in the work of Miller et al. (2012), and the addition of a viscous friction component (Moreira, 2009). This constitutive law is presented in Eq. (5.20).

Simulation Results and Discussion

Figure 5.10 shows the normal and tangential GRF curves for each circle separately and the total registered for the main foot segment. These graphs reveal a peak at about 0.3 s, which is when the foot first touches the ground, registering the maximum magnitude for both normal and tangential components of GRF.

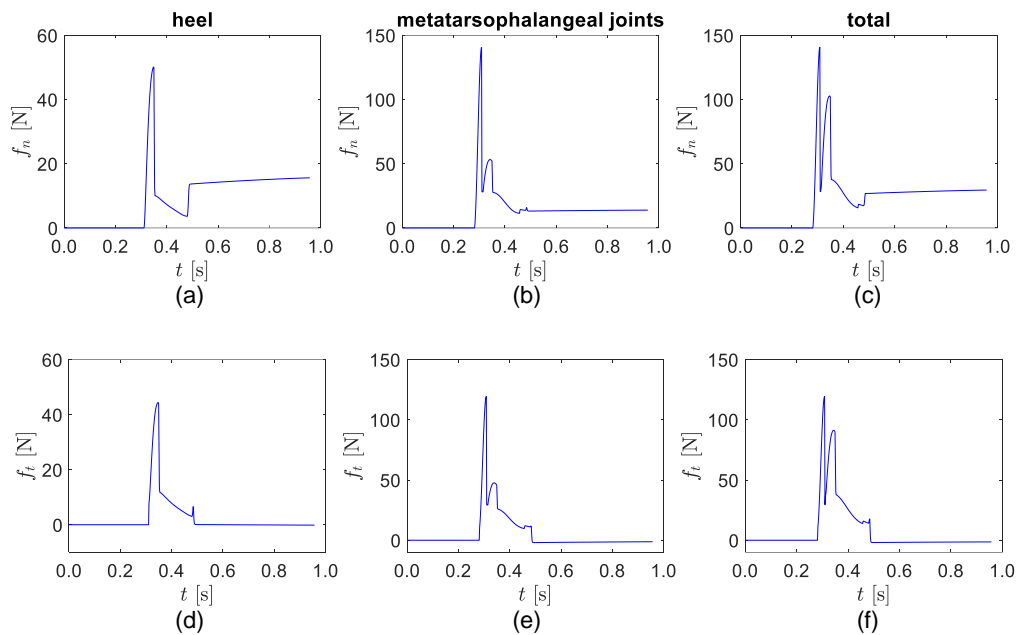


Figure 5.10. (a) Normal GRF for the circle located at the heel; (b) Normal GRF for the circle located at the MTP joints; (c) Total normal GRF registered for the foot; (d) Tangential GRF for the circle located at the heel; (e) Tangential GRF for the circle located at the MTP joints; (f) Total tangential GRF registered for the foot.

As no similar study of the GRF was found in the literature, it is not possible to compare the magnitude and shape of the curves and validate the results. However, from the graphs of the Figure 5.10, the methodologies of contact geometry definition, contact detection and the application of the contact forces through constitutive laws, are verified, and the foundations were established for the transition to a more complex model, in order to validate the entire methodology of foot-ground contact analysis.

As a complement to the dynamic analysis performed with the foot-leg multibody model, an animation of the executed motion was implemented in MATLAB. It represents a simple leg movement, initiated with the leg in the horizontal position, which is dropped by the action of the gravitational force. In Figure 5.11, it is presented the initial position of the leg-foot model in the MATLAB environment.

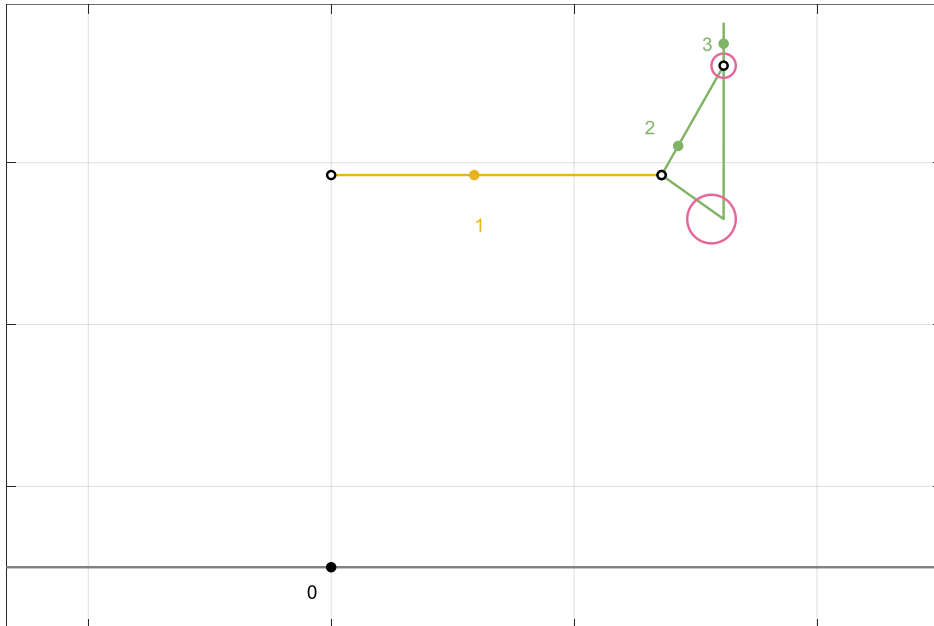


Figure 5.11. Initial position of the leg-foot model in the MATLAB simulation.

The model that was built for performing the animation is composed of three bodies that form the right leg under analysis. These bodies were depicted by basic elements – the leg and the toes were represented as straight lines, while the main foot part was represented as a triangle. The CM of each body was depicted as a point of the same color of the respective body. Furthermore, the revolute joints and the number of each anatomical segment were also represented.

On the MATLAB animation, it is possible to visualize the intersegmental motion of the leg-foot multibody model, and the contact circles that define the contact between the foot and the ground (which is represented as a horizontal straight line).

Due to the impossibility of showing the animation on paper format, an image was created with a few consecutive frames of it, taken with intervals of 0.1196 s, in order to give the perception of the motion under analysis and to observe the foot-ground contact. This image is presented in the Figure 5.12.

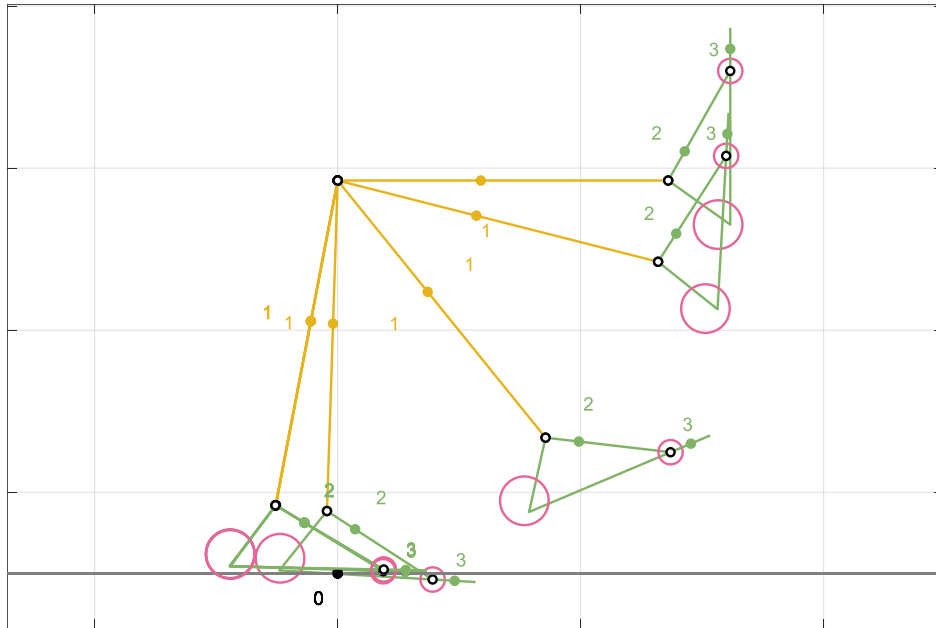


Figure 5.12. The simple leg motion representation performed with the leg-foot model in MATLAB.

5.5. Application Example 2: Human Gait Analysis

This section presents a study of the interaction between the foot and the level ground during human gait. For this application example, the $\frac{1}{2}$ HAT-leg multibody model is used, and the behavior of the system is achieved based on a dynamic analysis, employing experimental data to establish the required prescribed kinematic guide elements. Additionally, the contact interaction between the foot and the ground is modeled applying continuous approaches for the normal and tangential contact forces, and the contact detection method is based on simple geometries, namely circles and a plane.

Biomechanical Model Description

For this purpose, the biomechanical model presented in Section 4.1 – the $\frac{1}{2}$ HAT-leg model – is used, with some modifications regarding the geometry of the foot. Instead of being represented by a single segment, the foot is now constituted by two parts – the main foot part and the toes –, similar to what happened in Section 5.4. The actual biomechanical model, with its segments arranged in the initial position, is represented in Figure 5.13, where the local frames of each rigid body are visible.

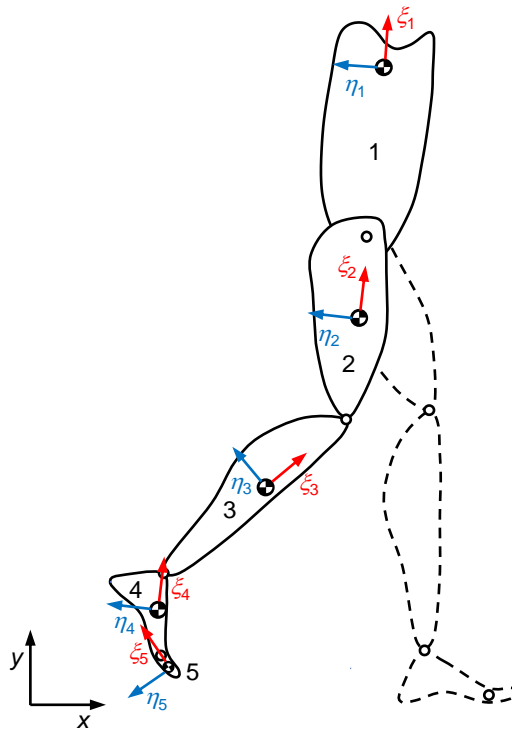


Figure 5.13. $\frac{1}{2}$ HAT-leg model representation in the initial position, and depiction of the local reference frames.

The model is composed of five rigid bodies – $\frac{1}{2}$ HAT, thigh, leg, main foot part and toes, from the right side of the human body – and the generalized coordinates vector, \mathbf{q} , is defined by 15 coordinates ($n = 15$). The bodies are connected by four revolute joints and, consequently, eight constraints are added to the system, since each joint removes two DOF from the system. Additionally, for simplification, the MTP joints are considered to be fixed, adding one constraint to the system and, consequently, removing one DOF. Thus, this $\frac{1}{2}$ HAT-leg multibody system has a total of six DOF, which correspond to three rotations about revolute joints – one DOF for hip flexion-extension motion, one DOF for knee flexion-extension and one DOF for ankle dorsiflexion-plantarflexion –, plus two translations and one rotation of the system.

This model, as well as the others used throughout this dissertation, was developed within a MATLAB computer code, using the multibody formulation with cartesian coordinates, which is described in Chapter 3.

Foot-Ground Contact Model

In this application example, the contact between the foot and the ground is geometrically defined by circles, defining the foot plantar surface, and a plane, representing the ground. As the contact is defined by contact circles, and the ground is considered to be flat and leveled, the interpenetration, δ , for

each contact circle, can be understood as the difference between the radius of the circle and the y -global coordinate of that circle center, as demonstrated in Eq. (5.33). The contact is detected if a positive value of δ is verified. In what concerns the considered continuous contact models, for the normal contact force, the model proposed by Ambrósio and Pombo (2018) is employed, which is described in Eq. (5.15), and the tangential force is evaluated through the model of Eq. (5.20).

In a first approach, different scenarios were tested, varying the number of circles, as well as their location and radius, through manual adjustment of these parameters. Several attempts were made, trying to approximate the simulated GRF curves to the experimental ones – presented in Figure 4.9.

The contact parameters – namely the nonlinear exponent factor, n , the contact stiffness, k , the coefficient of restitution, c_r , the Coulomb friction coefficient, μ_c , the viscous friction coefficient, μ_d , and the tolerance velocities, v_0 , – are defined in Table 5.7, and were not subject to any variation for the present approach.

Table 5.7. Contact parameters for the considered contact circles

n [-]	k [N/m ^{3/2}]	c_r [-]	μ_c [-]	μ_d [N.s/m]	$v_{0,n}$ [m/s]	$v_{0,t}$ [m/s]
3/2	40000	0.2	0.5	3	0.01	0.01

The number of circles was varied between two and nine, and the best acquired results for each considered number of circles are demonstrated in Table 5.8. In this table, the arrangement of the defined circles is depicted too. The results are shown in the form of graphs regarding the normal contact force, the tangential contact force, and the position of the COP. In these graphs, the results from simulations are compared with the ones obtained through the experimental analysis. It should be noticed that the shaded regions presented in the graphs of normal and tangential forces indicate a deviation from the experimental data of $\pm 20\%$ ¹² of the maximum value registered from the experimental analysis, and the shaded region presented in the COP position graph represent a bound of ± 5 cm¹³ in relation to the experimental data.

¹² This value was defined based on the one used by some found studies (Esposito & Miller, 2018; Lopes et al., 2016; Miller et al., 2012; Miller & Hamill, 2015; Neptune et al., 2000), in which the shaded area was defined by ± 2 standard deviations around the mean of the experimental data. According to Esposito and Miller (2018), a 10% distribution width is a reasonable estimate of the variance between human subjects, and hence, a $\pm 2 \times 10\%$ deviation was used to define the shaded region (Dorschky et al., 2019; Esposito & Miller, 2018).

¹³ In the case of the COP position, an area defined by ± 5 cm around the experimental data was defined, because in this situation, the definition of a percentage has no meaning in terms of physics, as it depends on the location of the origin of the global reference frame.

Table 5.8. Number of circles, their arrangement, and the obtained results

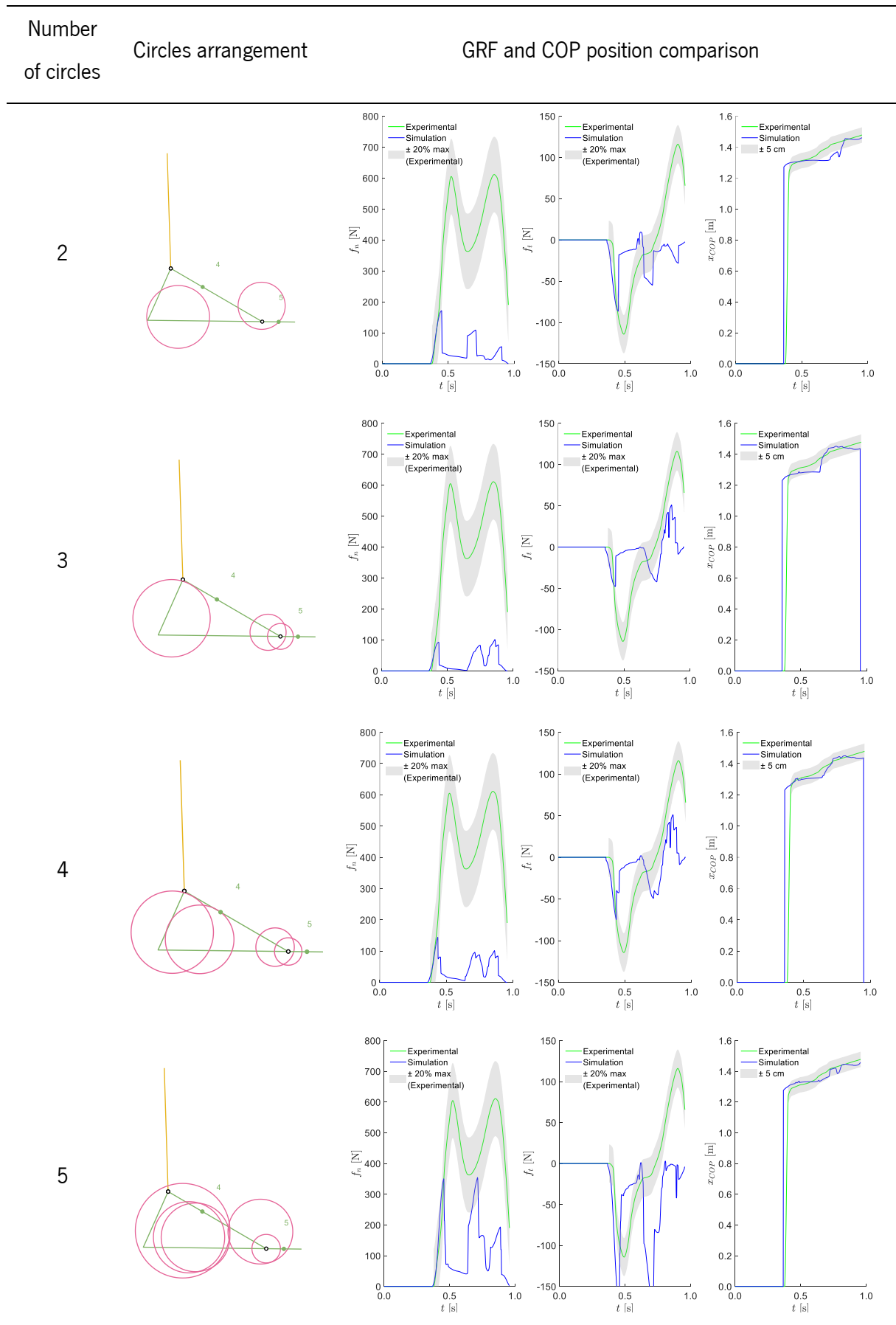
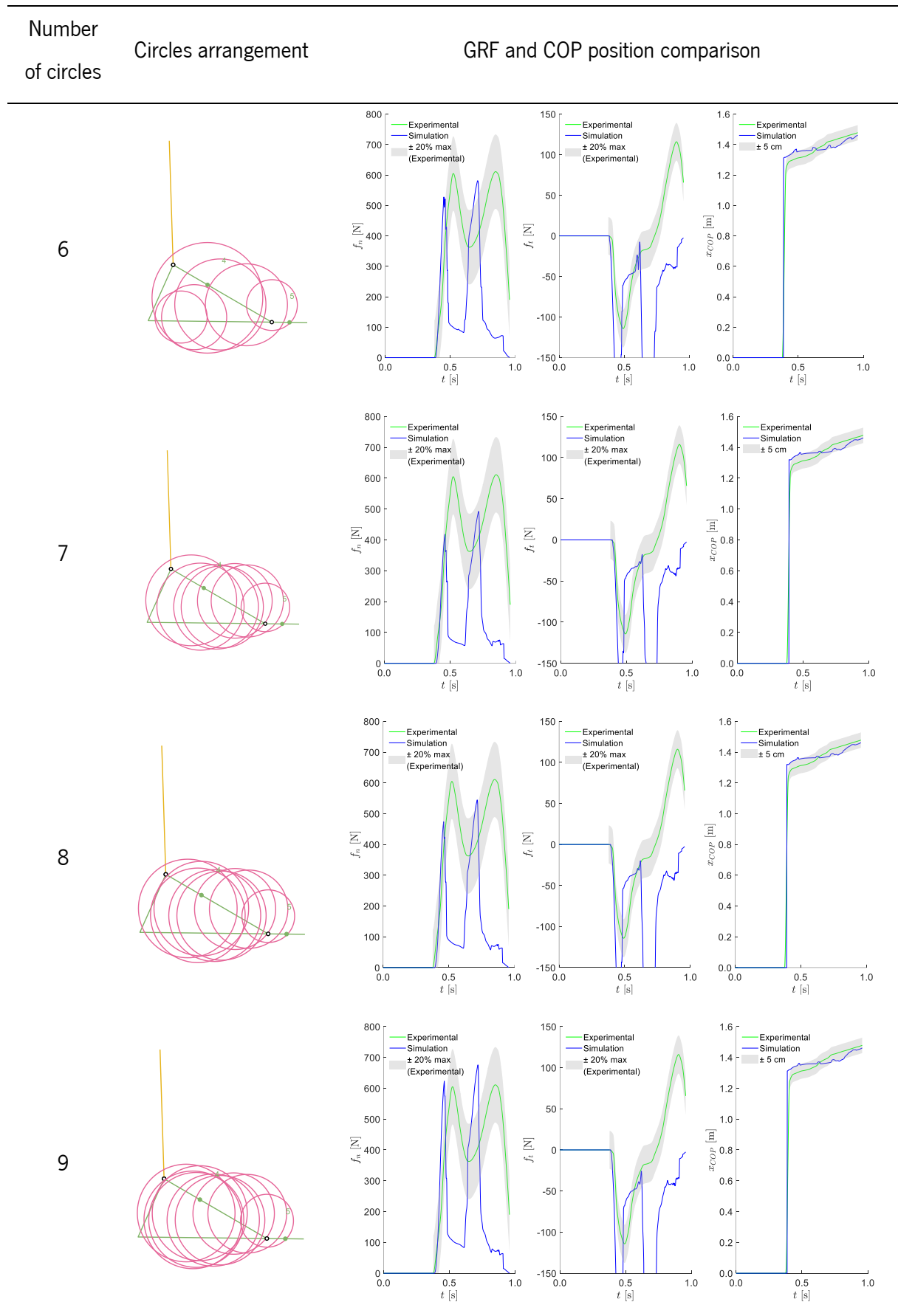


Table 5.8. (Continued)



For any number of circles, the results obtained from the simulations are very different from the experimental ones. The adopted methodology was based on a trial-and-error approach, which is characterized by performing repeatedly, varied attempts until reaching the best solution. However, this approach is uncertain since parameter adjustment becomes complex. In this sense, with the purpose of correctly determining the contact forces, an optimization process was implemented to obtain the most suitable values for the geometric and contact parameters of the proposed model.

Optimization Problem

The optimization methods aim to find a solution that minimizes a prescribed objective function, subjected to a certain number of restrictions. An optimization algorithm is a procedure which is executed iteratively by comparing various solutions until an optimum solution is found (MathWorks, 2022c; Tavares da Silva, 2003). In mathematical terms, a general optimization problem can be stated as

$$\min f(\mathbf{x}) \quad (5.34)$$

subjected to

$$\begin{aligned} G_i(\mathbf{x}) &= 0 & (i = 1, \dots, m_e) \\ G_i(\mathbf{x}) &\leq 0 & (i = m_e + 1, \dots, m) \\ x_j^l &\leq x_j \leq x_j^u & (j = 1, \dots, n) \end{aligned} \quad (5.35)$$

where \mathbf{x} is the vector of design parameters or optimization variables – $\mathbf{x} = \{x_1, x_2, \dots, x_n\}$ –, each one of them bounded between x_j^l and x_j^u , and $f(\mathbf{x})$ is the objective function to be minimized, which can be subjected to equality and inequality constraints evaluated at \mathbf{x} . The optimal solution from among the set of candidate solutions, \mathbf{x}^* , is constituted by the parameters that minimize the objective function, fulfilling the restrictions imposed. Optimization problem formulation constitutes an efficient method for solving large-scale problems that cannot be easily addressed by other techniques, or when highly iterative processes are needed (El-Halwagi, 2006; MathWorks, 2022c; Tavares da Silva, 2003).

In this work, the objective is to approximate the curves from the simulations to those obtained by experimental analysis. The optimization problem is solved using the MATLAB *'fmincon'*, which is a gradient-based method. This method applies a gradient descent algorithm to iteratively find a local minimum of the objective function. First, the algorithm calculates the gradient (slope) of the function at the current point, i.e., the first-order derivative. Then, the algorithm iteratively determines the next point,

using the gradient at the current position, scaled by a learning rate¹⁴. The obtained value is subtracted from the current position, taking a step in the opposite direction of the gradient, in order to minimize the function. This process is repeated until the maximum number of iterations is reached or until the step size is smaller than the step tolerance – which is set to the default value 1×10^{-10} . The MATLAB *'fmincon'* also requires the definition of a starting point – an initial guess – from which the optimization algorithm will start the iterative process (Kwiatkowski, 2021; MathWorks, 2022b; Yadav, 2021).

Simulation Results and Discussion

As mentioned previously, with the objective of minimizing the difference between the simulation results and the experimental data, an optimization process is implemented. Therefore, the optimization process intends to find the best values for the geometric and contact parameters of the proposed model that minimize the prescribed objective function. The results presented below are focused on the use of 3 circles to define the foot geometry, however other situations were tested, namely for 2 and 4 circles.

First, it is important to mention that a new reference frame – $\xi'_4 \eta'_4$ (Figure 5.14) – was created in the foot to more easily define the parameters related to coordinates of the circles' center and their lower and upper limits.

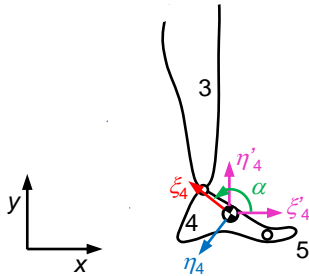


Figure 5.14. New reference frame created in the foot.

Table 5.9 presents the parameters that are not optimized, i.e., those that are included as predefined values. These values are the same for all considered circles and are valid for all simulations performed from this point onwards.

Table 5.9. Contact parameters for the considered contact circles

n [-]	μ_d [N.s/m]	$v_{0,n}$ [m/s]	$v_{0,t}$ [m/s]
3/2	3	0.01	0.01

¹⁴ The learning rate is a scaling factor utilized to adjust the step size at each iteration (Kwiatkowski, 2021).

This optimization process is intended to find the best values for the position of the center of each circle, and for the radius, contact stiffness, coefficient of restitution and Coulomb friction coefficient assigned to each circle. On Table 5.10, the initial guess vector, x_0 , which contains an initial value for each parameter to optimize, as well as the lower and upper limits, lb and ub respectively, defined for each one, are shown. It should be noticed that the parameters values were normalized between 0 and 1, corresponding, respectively, to the lower and upper limits of the variables.

Table 5.10. Initial guess and lower and upper limits of each parameter for optimization process

	Parameters	x_0	lb	ub
Circle 1	x^1 [m]	-0.04	-0.09	0.0
	y^1 [m]	-0.02	-0.0562	0.02
	r^1 [m]	0.065	0.04	0.11
	k^1 [N/m ^{3/2}]	230000.0	40000.0	400000.0
	c_r^1 [-]	0.94	0.3	0.95
	μ_c^1 [-]	0.11	0.1	0.3
Circle 2	x^2 [m]	0.01	0.0	0.08
	y^2 [m]	0.009	-0.0562	0.02
	r^2 [m]	0.11	0.045	0.115
	k^2 [N/m ^{3/2}]	130000.0	40000.0	400000.0
	c_r^2 [-]	0.94	0.3	0.95
	μ_c^2 [-]	0.11	0.1	0.3
Circle 3	x^3 [m]	0.118	0.08	0.126
	y^3 [m]	-0.063	-0.075	0.0
	r^3 [m]	0.0095	0.005	0.1
	k^3 [N/m ^{3/2}]	100000.0	40000.0	400000.0
	c_r^3 [-]	0.94	0.3	0.95
	μ_c^3 [-]	0.11	0.1	0.3

For this initial guess, the distribution of the contact circles, and the graphs related to the normal and tangential contact forces, as well as to the position of the COP, are depicted in Figure 5.15. The geometry of the foot is defined by three circles, positioned at the heel, the MTP joints and at the middle region of the foot. The obtained simulation curve for the normal force has two evident peaks, which is in agreement with the experimental data. However, these peaks are out of phase when compared with the experimental curve. The simulated tangential force has some divergencies when compared with the experimental one, being lower in magnitude and discordant in shape, around the 0.7 s. The position of the COP follows more strictly the experimental data.

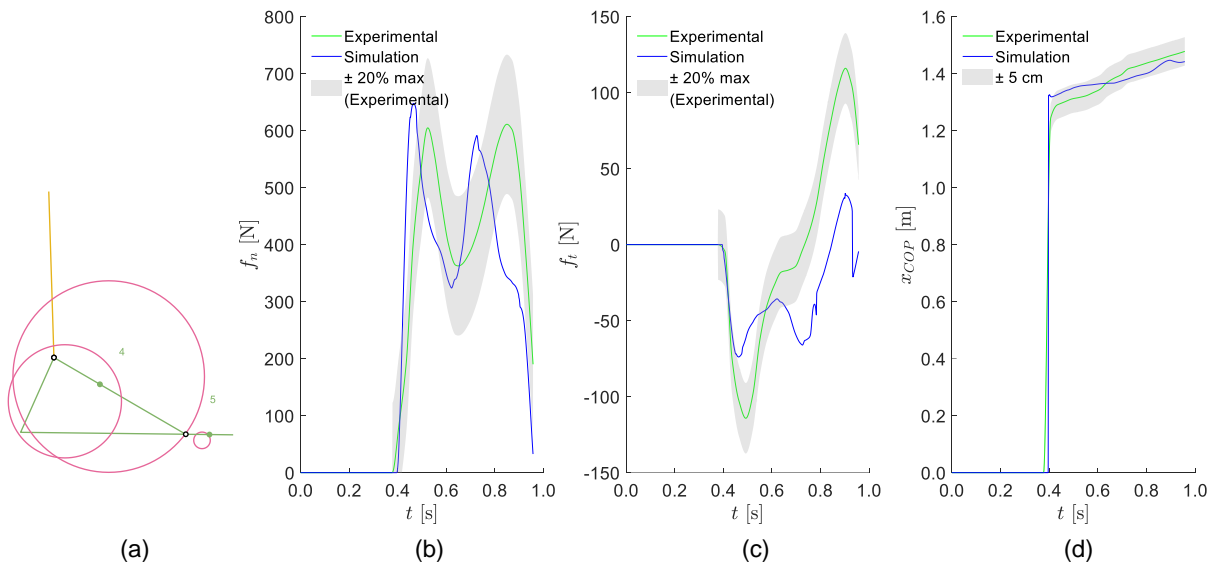


Figure 5.15. Initial guess: (a) Contact circles arrangement; (b) Comparison between the experimental and simulated normal contact force; (c) Comparison between the experimental and simulated tangential contact force; (d) Comparison between the experimental and simulated COP position.

Regarding the objective function, three different approaches were evaluated. The divergency between them is the utilized exponent. For the first case, the function is formulated through the sum of the absolute value of the error of each component under study, i.e., the difference between the simulation and experimental results for the normal force, tangential force and COP location (Eq. (5.36)).

$$J = w_{nc} + \frac{1}{w_{total}} \sum_i \left[\left| w_1 \frac{f_{i,n}^{sim} - f_{i,n}^{exp}}{\max(f_n^{exp})} \right| + \left| w_2 \frac{f_{i,t}^{sim} - f_{i,t}^{exp}}{\max(f_t^{exp})} \right| + \left| w_3 \frac{x_{i,COP}^{sim} - x_{i,COP}^{exp}}{\max(x_{COP}^{exp})} \right| \right] \quad (5.36)$$

The second considered objective function is defined based on the sum of the square differences between the simulation and experimental data, as seen in Eq. (5.37).

$$J = w_{nc} + \frac{1}{w_{total}} \sum_i \left[\left(w_1 \frac{f_{i,n}^{sim} - f_{i,n}^{exp}}{\max(f_n^{exp})} \right)^2 + \left(w_2 \frac{f_{i,t}^{sim} - f_{i,t}^{exp}}{\max(f_t^{exp})} \right)^2 + \left(w_3 \frac{x_{i,COP}^{sim} - x_{i,COP}^{exp}}{\max(x_{COP}^{exp})} \right)^2 \right] \quad (5.37)$$

The third approach is the definition of the objective function based on the sum of the cubed error of each component, as demonstrated in Eq. (5.38).

$$J = w_{nc} + \frac{1}{w_{total}} \sum_i \left[\left| w_1 \frac{f_{i,n}^{sim} - f_{i,n}^{exp}}{\max(f_n^{exp})} \right|^3 + \left| w_2 \frac{f_{i,t}^{sim} - f_{i,t}^{exp}}{\max(f_t^{exp})} \right|^3 + \left| w_3 \frac{x_{i,COP}^{sim} - x_{i,COP}^{exp}}{\max(x_{COP}^{exp})} \right|^3 \right] \quad (5.38)$$

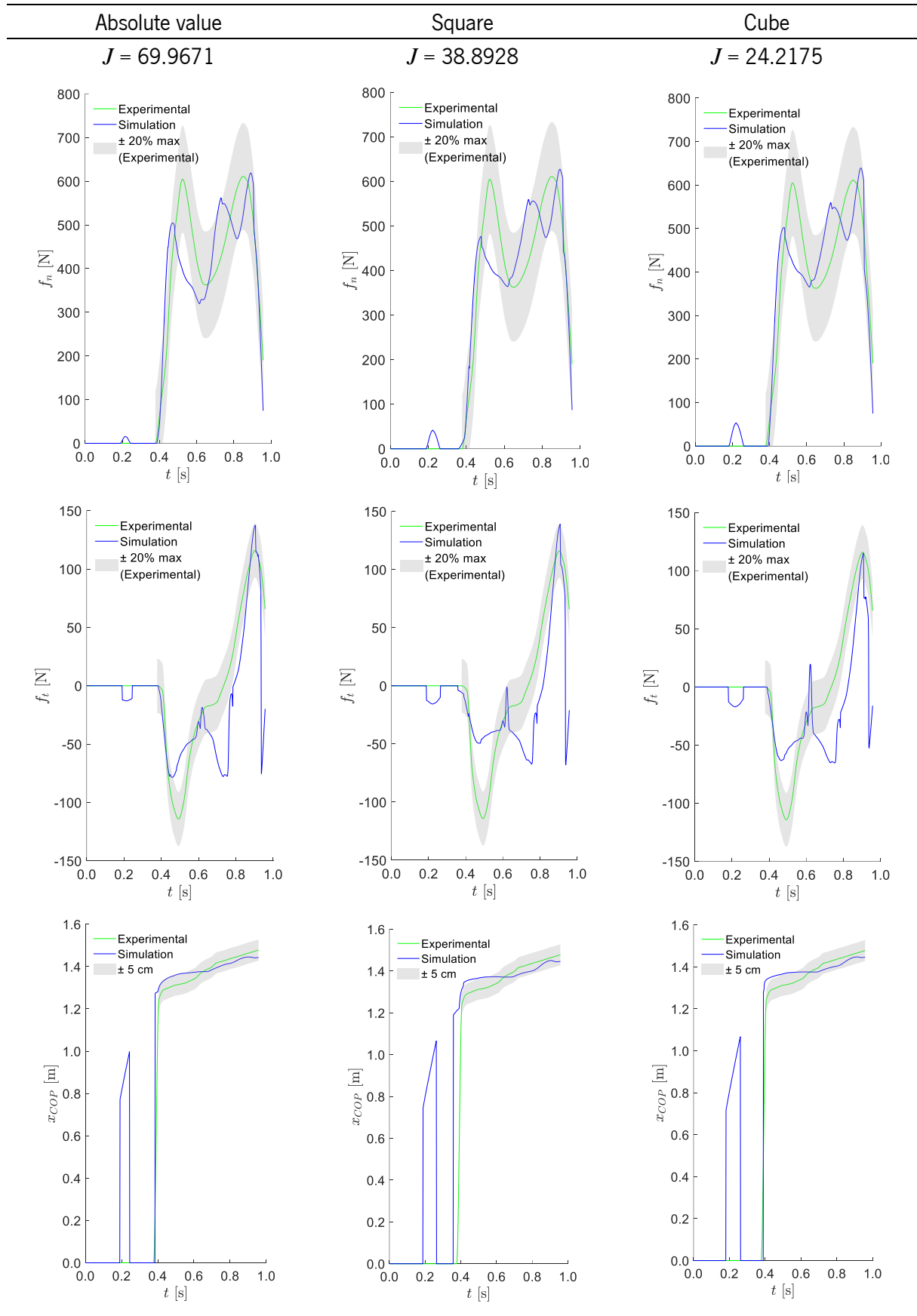
In these expressions, $f_{i,n}$ is the normal contact force, $f_{i,t}$ is the tangential contact force, and x_{COP} is the x -coordinate of the COP, at time step i . The indication *sim* represents the results obtained by the simulations, while *exp* stands for experimental data. Moreover, the differences between the simulation and experimental data for each component are divided by the maximum experimental value registered, with the objective of adjusting the units and making the expression dimensionless. w_1 , w_2 and w_3 are assigned weights for each component, being w_{total} the sum of the other three. Finally, w_{nc} is a weight which aims to penalize the situations that have one or more circles presenting less contact, evaluated through a pseudo-penetration close or equal to zero. For situations where the deformation is very small, w_{nc} will take a high value and, therefore, the objective function value will increase. This weight is calculated by the following expression

$$w_{nc} = \sum_c \frac{\delta_r}{\max(\delta_c) + \delta_0} \quad (5.39)$$

where $\max(\delta_c)$ is the maximum value of pseudo-penetration registered for each circle c , δ_0 is a penetration tolerance (defined as 1×10^{-7} m) and δ_r represents a value below which a greater penalization is applied (defined as 0.01 m).

A study on these three objective functions was performed. For this study, the weights attributed to the normal contact force, to tangential contact force and to the position of the COP were $w_1 = 3$, $w_2 = 1$ and $w_3 = 0.1$, respectively. The results of the performed optimizations, comparing the effects of the exponent used in the objective function (absolute value, square or cube), are represented in Table 5.11, where the graphs of the three components in study are represented, as well as the obtained value of the objective function. The detailed results of the optimal solution for each optimization can be found in the Appendix I (Table I.1).

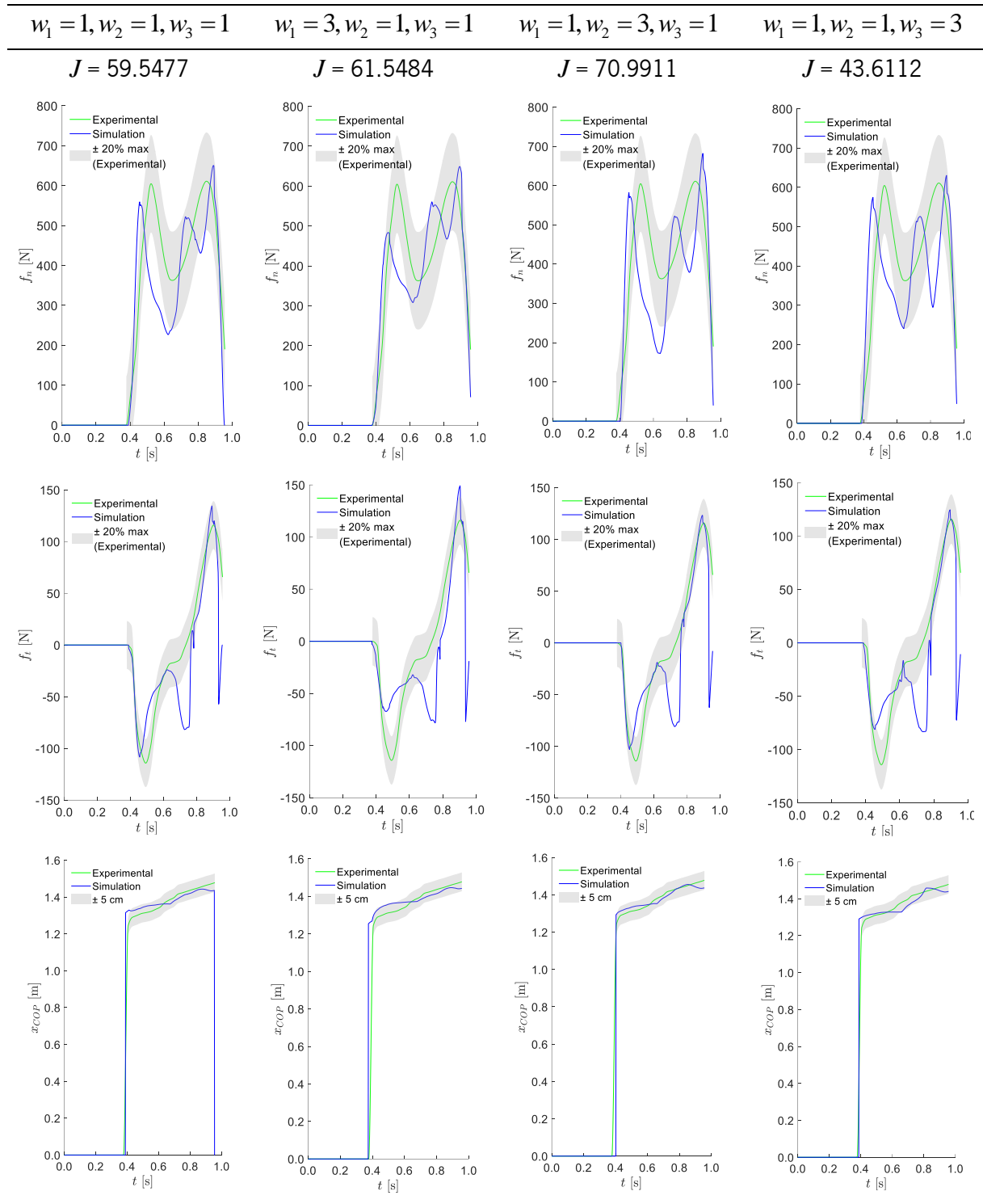
Table 5.11. Comparison between the results obtained from the optimizations performed with three different approaches for the definition of the objective function



From this study, it is possible to conclude that the results are very similar between each other. The normal contact force curve of the simulation analysis had three peaks, which is in disagreement with the experimental data. The simulated tangential force had discrepancies when compared with the experimental curve. The last peak was the one that presented the best fitting in terms of magnitude for the optimizations performed with any of the three objective functions. The first valley of the tangential contact force closely matched the experimental curve, when the objective function defined with the absolute value was employed. Around 0.6 s, this curve presented an undesirable peak for the square and cube approaches. About 0.7 s the simulated curve was discordant in shape for all three approaches. The position of the COP followed more closely the experimental data, showing less error in the first approach (objective function defined with the absolute value). All the results presented contact in the swing phase of the gait cycle, being less evident in the graphs of the first column of the Table 5.11, where the forces had a lower magnitude, and the contact took less time. For the reasons described above, the implemented objective function for the next optimizations were the described in Eq. (5.36), which is formulated through the sum of the absolute value of the error of each component under study, i.e., the absolute value of the difference between the simulation and experimental results for the normal force, tangential force and COP location.

On Table 5.12, a study on the weights applied for each component is shown. Firstly, it was performed an optimization in which equal values for w_1 , w_2 and w_3 were considered. It means that both the normal and tangential forces, as well as the position of the COP, influence the objective function in equal measure. Then, a higher weight was assigned to each component separately, in order to study the influence of attributing more value to each component. The results of the performed optimizations, comparing the simulated and experimental curves of the normal contact force, the tangential contact force and the COP position, are represented, as well as the obtained value of the objective function. The detailed results of the optimal solution for each optimization can be found in the Appendix I (Table I.2).

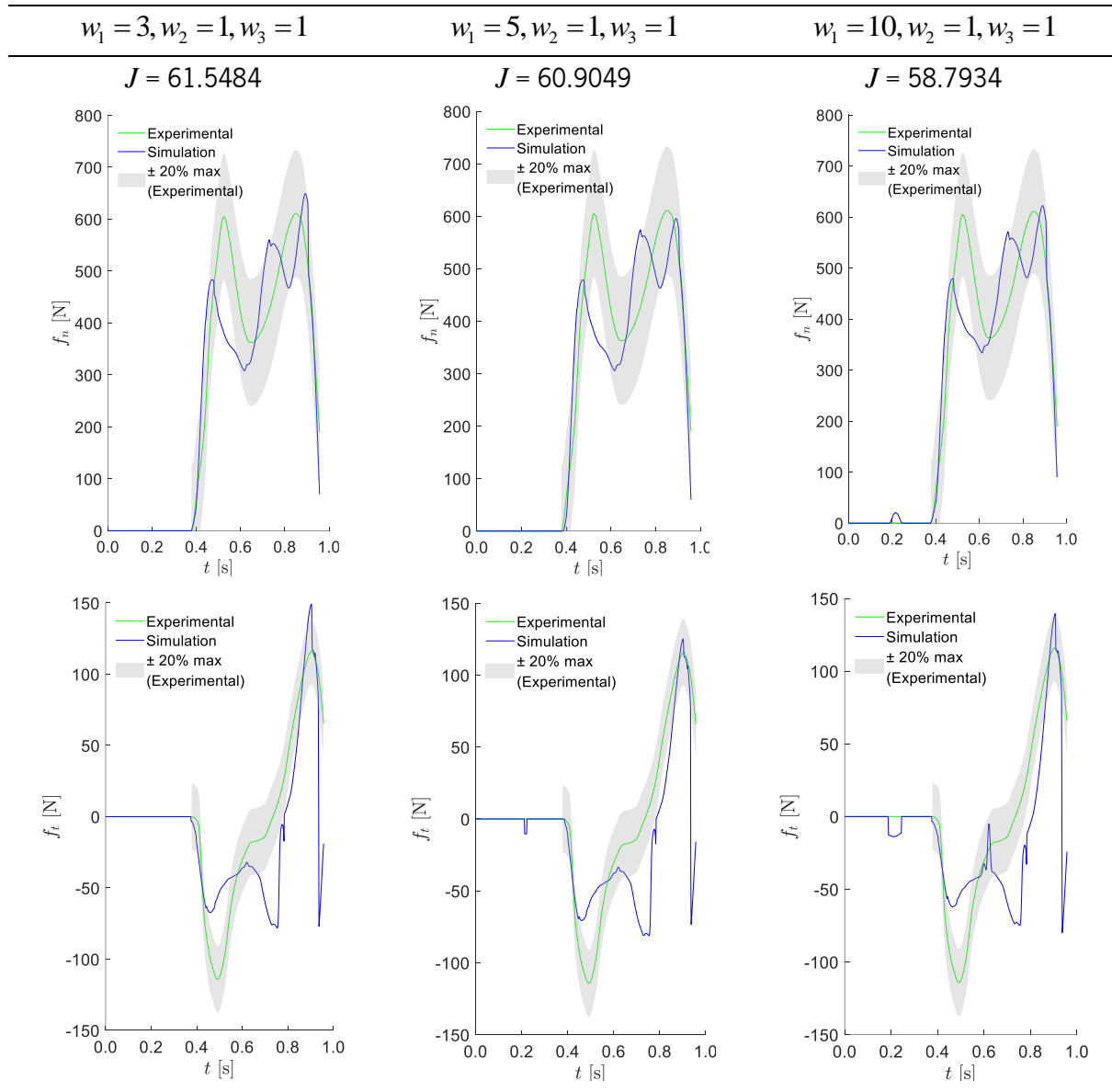
Table 5.12. Comparison between the results obtained from the optimizations performed with different weights for each component



The results show that, in general, a higher weight assigned to a component results in improvements in the respective curve obtained. For the normal contact force, the curves presented in the first, third and fourth columns of Table 5.12 were worse in terms of error established between the simulation and experimental analyses. This can be seen as the portion of the blue curve that falls out of the shaded area. In spite of registering three peaks, when a higher weight for the normal contact force was considered, the simulation curve acted closer to the experimental one, in comparison with the other results of other optimizations performed. The tangential force curve obtained from the simulations was similar for the optimization accomplished with equal values for w_1 , w_2 and w_3 for each component, and for the one that considered a higher value for w_2 . However, the last peak appeared closer to the one presented in the experimental curve for the results of the third column of the table. For the COP position, opposing to what was expected, the simulated curve which seems to follow more strictly the experimental data was the one presented in the third column (for $w_1 = 1, w_2 = 3, w_3 = 1$), rather than when a higher weight was considered for that component. Nevertheless, all the simulated curves for x -position of the COP were consistent with the experimental data.

As the normal contact force is the one that has more relevance in the context of multibody dynamics, a study on the influence of the weight of that component was carried out. The weight assigned to the normal force was subject to a variation between 3, 5 and 10, with the objective of improving the respective curve obtained from the simulation, preferentially removing the extra peak that persisted in the previous results. The results of the performed optimizations, comparing the curves established from the simulation and experimental analysis of the normal and the tangential contact force, are displayed in Table 5.13, as well as the obtained objective function value. The graphs of the position of the COP are not shown, as they were all similar, fitting well with the experimental data. The detailed results of the optimal solution for each optimization can be found in the Appendix I (Table I.3).

Table 5.13. Comparison between the results obtained from the optimizations performed with different weights for normal contact force

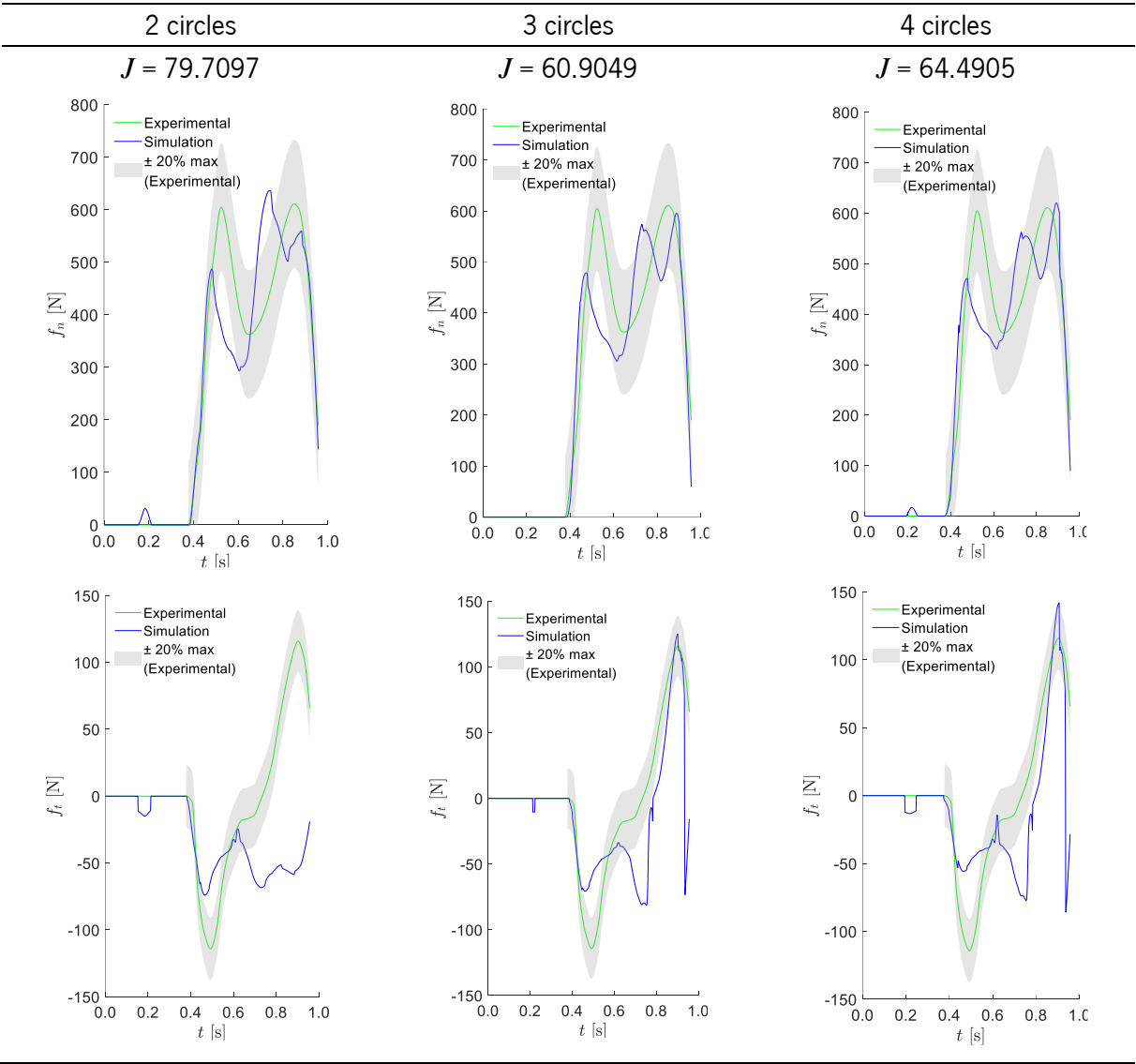


The obtained results were not very different from each other. Regarding the normal contact force, which was the principal object of study in this analysis, it presents three peaks for all performed optimizations, which is in disagreement with the experimental results. In spite of increasing the weight of the normal contact force component, the results did not show this difference significantly, because the objective function accounts for the relative weight instead of the defined absolute weight. For example, an increase of twice from the second to the third column, does not mean that the relative weight has duplicated. The difference in the normal force weight between these two approaches is approximately 13%, in relative terms. In what concerns to the tangential force, its last peak was best fitted in terms of magnitude in the second approach (for $w_1 = 5$). When a weight of 10 was assigned to the normal force,

the tangential curve obtained from the simulation got worse, registering an undesirable peak, around 0.6 s. The results from the second and third columns of the Table 5.13 presented contact in the swing phase of the gait cycle, being more evident with the increasing of w_1 . Moreover, the optimization accomplished with a higher value for w_1 , was more expensive in terms of computational time (see Table I.3 from Appendix I).

Lastly, a study on the number of circles used to define the geometry of the foot surface was carried out. A comparison between the results of optimizations performed with 2, 3 and 4 circles is displayed in Table 5.14. For these optimizations the following weights were used: $w_1 = 5, w_2 = 1, w_3 = 1$. The graphs of the COP position are not shown, as they were all similar, fitting well with the experimental data. The detailed results of the optimal solution for each optimization can be found in the Appendix I (Table I.4).

Table 5.14. Comparison between the results obtained from the optimizations performed with different number of circles



Regarding the study of the number of the circles used to describe the foot plantar surface, the expected would be that for a higher number of circles, the curves obtained in the simulations would be more similar to those of the experimental data. The reason to believe in that is the fact that the optimization algorithm could adjust the circles' size and rearrange them in a position that represented more realistically the foot anatomy, and consequently, provide better results in terms of contact forces. The more circles, the more possibilities there are for creating new configurations with them, in order to describe accurately the foot plantar surface. This was true for the transition between 2 and 3 circles. However, when the fourth circle is added, there are no significant improvements in the normal contact force curve and the tangential one gets worse. The tangential contact force curve, for 2 circles has big discrepancies from the experimental curve in the last peak. Comparing the tangential force between the 3 and 4 circles' approach, the last peak presented the best fitting in terms of magnitude for the results obtained with 3 circles. Moreover, all the results presented contact in the swing phase of the gait cycle, being less evident in the graphs of the second column of the Table 5.14, where the forces had a lower magnitude, and the contact took less time. For the reasons described above, the approach that considers 3 circles to model the foot was the one that presented the best overall results. Concerning the computational time spent with these optimizations, for 4 circles, there was a substantial increase in the optimization time (see Table I.4 from Appendix I).

Despite the number of optimizations performed, with the intent of improving the simulation curves – in particular the one of the normal contact force –, the best acquired graph for that component was the one provided by the initial guess, as it is the only one that only presented two peaks and followed closely the shape of the experimental data.

In this sense, it is desirable to improve the tangential force curve, depicted in Figure 5.15, keeping the simulation curve of the normal force and of the position of the COP. With this objective, a new optimization was done, in which the only parameters that were varied were the coefficients of friction for the three circles. The input data, as well as the obtained results for the optimal solution are described in Appendix I (Table I.5). The final curves of the normal and tangential contact forces, as well as the x -position of the COP are displayed in Figure 5.16.

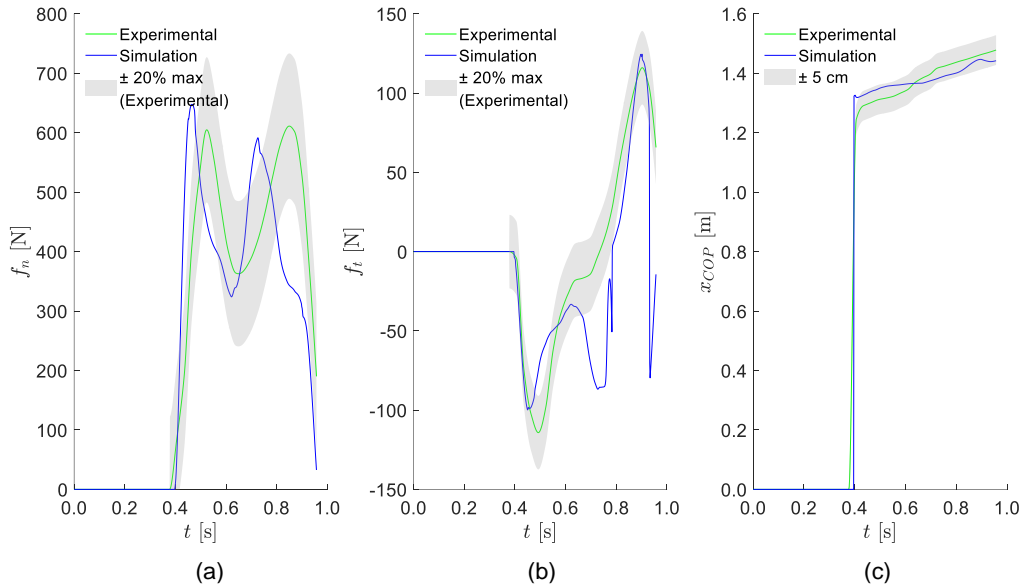


Figure 5.16. Comparison between the experimental data and the results obtained from the optimization of the coefficient of friction, for (a) the normal contact force; (b) the tangential contact force; (c) the COP position.

Although these results are not perfect, they were the best achieved after numerous trials and optimizations. The normal contact force has two evident peaks, in agreement with the experimental data, but they are out of phase compared to the experimental curve. The tangential force has a discordancy in shape, around the 0.7 s, presenting an undesirable valley. The position of the COP follows more strictly the experimental data.

Gradient based algorithms, like the one used – MATLAB ‘*fmincon*’ –, iteratively find the nearest local minimum from the given starting point. There is no method to guarantee that ‘*fmincon*’ finds a global minimum of the objective function. The only approach to mitigate the problem is running the optimization process from various starting points, which can become computationally expensive (Hendricks, 2015). Despite the fact that only one initial guess was specified in this work for performing the optimizations presented in this section, various initial guesses were tested. Nonetheless, only the results of the optimizations with the initial guess described in Table 5.10 were analyzed and presented in this dissertation, otherwise the presentation of the results would be too extensive. This initial guess was reached after several attempts, and was considered to be the best one tested because the optimization process would start from a good approximation for the normal contact force.

It should also be mentioned that tests were made with another optimization algorithm, the genetic algorithm. However, the obtained results in terms of both the value of the objective function and the computational time were not satisfactory, which is the reason why this method was not adopted for the optimization of the foot-ground contact parameters and its results are not presented here.

5.6. Summary

In this chapter, the main aspects related to the modeling and simulation of contact problems in the context of MBS dynamics were presented, and two application examples were described and discussed. First, the fundamental aspects of a generic contact problem were approached, and the methodologies that deal with contact detection and contact resolution were introduced.

In the first application example, a simple leg motion was simulated with the objective of validating the methodologies of contact geometry definition and contact detection. This simulation consisted of a simple drop test in which the motion of the model is generated by the action of the gravitational force. This example validated the methodologies of contact geometry definition, contact detection and the application of the contact forces through constitutive laws.

The second application example was presented for studying the interaction between the foot and the level ground during human gait. After a manual parameter adjustment approach, an optimization process was implemented to obtain the most suitable values for the geometric and contact parameters of the proposed model. All obtained results from optimizations were compared to the ones obtained by experimental analysis, with the intention of validating the proposed approach. Studies were carried out on the formulation of the objective function, on the weights assigned to each component, and particularly on the weight attributed to the normal contact force. An evaluation of the influence of the number of circles was also performed. Lastly, since all the obtained results from the optimizations were not close enough to the experimental data, and the normal force curve obtained from the initial guess was the one that presented a better shape, an attempt was made in order to improve, individually, the tangential force curve, optimizing only the coefficient of friction for each circle.

Chapter 6 – Concluding Remarks

In this final chapter, the general conclusions concerning the development of this dissertation are pointed out. Moreover, in this chapter, some future perspectives and developments that can be conducted in the context of this work are also mentioned, with the aim of further improving the accuracy in reproducing the foot-ground interaction, within the framework of biomechanical multibody systems analysis.

6.1. Conclusions

In this dissertation report, a two-dimensional computational multibody model was developed and implemented in the MATLAB software, in order to analyze the dynamic behavior of the human body and its interaction with the surrounding environment. To achieve these results, the main aspects related to multibody systems formulation were reviewed and discussed in the context of biomechanics of planar motion. In addition, and to understand the expected movements, the fundamental anatomical and biomechanical aspects of the human lower limb were explored. The literature on the foot-ground contact modeling strategies for human motion analysis was revisited in Section 1.3, and a review article concerning this theme was also produced.

In Chapter four, it was intended to perform a dynamic analysis of the human gait, in which kinematic and kinetic data are prescribed, and all DOF are guided. The developed multibody model – $\frac{1}{2}$ HAT-leg model – was described employing cartesian coordinates and it was composed of four rigid bodies, that correspond to the main segments of the right side of the human body, linked by three ideal revolute joints. The consistency of the initial conditions required to begin the dynamic analysis, in particular the initial velocities, were analyzed to verify its conformity with the kinematic structure of the biomechanical model. The constraint equations, relative to the revolute joints and to the bodies' CM trajectories, were established and explicitly presented, and the external applied forces were also specified. Three different interpolation methods – '*spline*', '*pchip*' and '*akima*' – were presented and compared in terms of the outcomes from the graphs and the simulation time. Moreover, the integration algorithm applied to solve the equations of motion in MATLAB was analyzed, and a study on the influence of the values of the

Baumgarte stabilization parameters on the violation of constraints was presented. Lastly, an animation of the $\frac{1}{2}$ HAT-leg model was developed in MATLAB, in order to visualize the prescribed motion.

In Chapter five, contact modeling was considered for the foot-ground interface. First, the main aspects associated with the modeling and simulation of a generic contact problem were introduced, namely the methodologies concerning the detection and resolution of contact events. Furthermore, two application examples were described and discussed. The first one dealt with a simulation of a simple leg motion, generated by the action of the gravitational force. This example validated the methodologies of contact geometry definition, contact detection and the application of the contact forces through constitutive laws. The second application example was presented for studying the interaction between the foot and the level ground during human gait. Following the conclusions of the previous chapter, in this approach, contact circles were used to define the geometry of the plantar surface. After a manual parameter adjustment methodology, an optimization process was implemented to obtain the most suitable values for the geometric and contact parameters of the proposed model. The results obtained from optimizations were compared to those obtained by experimental analysis, with the intention of validating the proposed model. The formulation of the objective function, the weights assigned to each component, in particular the weight attributed to the normal contact force, and the number of circles considered for the foot geometry were studied, and their influences on the results were analyzed. All the obtained results from the optimizations were not sufficient close to the experimental data. Lastly, since the normal force curve obtained from the initial guess was the one that presented a better shape, an attempt was made to improve, individually, the tangential force curve, optimizing only the coefficient of friction for each circle. Although these last results were not perfect in terms of the shape of GRF curves, they were the best achieved after numerous trials and optimizations. The normal contact force had two evident peaks, in agreement with the experimental data, but they were out of phase compared to the experimental curve. The tangential force had a discordancy in shape, around the 0.7 s, presenting an undesirable valley. The position of the COP curve was the one that more rigorously followed the experimental data, in all the simulations performed.

6.2. Future Developments

As a limitation to this study, it is important to mention the restriction of the simulations to the sagittal plane, since the considered biomechanical model was bi-dimensional. Due to this assumption, the movements executed on the frontal and transverse planes were not considered, in particular the effects of eversion-inversion, abduction-adduction and pronation-supination movements of the foot were disregarded. However, the joints present in the human lower limb exhibit motion primarily in the sagittal plane, making it possible to simplify the analysis of the gait process only in this plane. According to Oatis (2009), the fundamental biomechanical principles in a 2D analysis are the same as those in a 3D analysis. Consequently, a simplified 2D representation of a 3D problem may be used to describe a model with less complexity. Nevertheless, in the future, a three-dimensional analysis of the gait and of the interaction between the foot and the ground during this process would be interesting.

Additionally, the following items are proposed, aiming to contribute to the improvement of this work, with regard to the accuracy of the foot-ground interface model:

- Testing other objective functions, to refine the shape of the contact force curves;
- Testing other optimization algorithms, in order to find the global minimum of the objective function;
- Implementing other, possibly more detailed, contact models;
- Defining the foot geometry more accurately, for example with a larger number of contact circles, or using more complex geometries such as ellipses or shapes obtained from scanning procedures.

References

- Abu-Faraj, Z. O., Harris, G. F., Smith, P. A., & Hassani, S. (2015). Human gait and Clinical Movement Analysis. In *Wiley Encyclopedia of Electrical and Electronics Engineering* (2nd ed., pp. 1–34). John Wiley & Sons, Inc. <https://doi.org/10.1002/047134608X.W6606.pub2>
- Abu El Kasem, S. T., Aly, S. M., Kamel, E. M., & Hussein, H. M. (2020). Normal active range of motion of lower extremity joints of the healthy young adults in Cairo, Egypt. *Bulletin of Faculty of Physical Therapy, 25*(2), 7. <https://doi.org/10.1186/s43161-020-00005-9>
- Alonso, F. J., Del Castillo, J. M., & Pintado, P. (2007). Motion data processing and wobbling mass modelling in the inverse dynamics of skeletal models. *Mechanism and Machine Theory, 42*(9), 1153–1169. <https://doi.org/10.1016/j.mechmachtheory.2006.08.006>
- Ambrósio, J., & Pombo, J. (2018). A unified formulation for mechanical joints with and without clearances/bushings and/or stops in the framework of multibody systems. *Multibody System Dynamics, 42*, 317–345. <https://doi.org/10.1007/s11044-018-9613-z>
- Andriacchi, T. P., & Hurwitz, D. E. (1997). Gait biomechanics and the evolution of total joint replacement. *Gait & Posture, 5*(3), 256–264. [https://doi.org/10.1016/S0966-6362\(97\)00013-1](https://doi.org/10.1016/S0966-6362(97)00013-1)
- Arnold, A. S., & Delp, S. L. (2005). Computer modeling of gait abnormalities in cerebral palsy: application to treatment planning. *Theoretical Issues in Ergonomics Science, 6*(3–4), 305–312. <https://doi.org/10.1080/14639220412331329636>
- Baker, R. (2007). The history of gait analysis before the advent of modern computers. *Gait & Posture, 26*(3), 331–342. <https://doi.org/10.1016/j.gaitpost.2006.10.014>
- Barbosa, I. C. J. (2017). Identification of contact properties of the foot in the stance phase of walking. *2017 IEEE 5th Portuguese Meeting on Bioengineering (ENBENG)*, 1–4. <https://doi.org/10.1109/ENBENG.2017.7889464>
- Baumgarte, J. (1972). Stabilization of constraints and integrals of motion in dynamical systems. *Computer Methods in Applied Mechanics and Engineering, 1*(1), 1–16. [https://doi.org/10.1016/0045-7825\(72\)90018-7](https://doi.org/10.1016/0045-7825(72)90018-7)
- Betts, J. G., Desaix, P., Johnson, E., Johnson, J. E., Korol, O., Kruse, D., Poe, B., Wise, J. A., Womble, M., & Young, K. A. (2017). *Anatomy and Physiology*. OpenStax.
- Brodke, D. S., Skinner, S. R., Lamoreux, L. W., Johanson, M. E., Helen, R. St., Moran, S. A., & Ashley, R.

- K. (1989). Effects of Ankle-Foot Orthoses on the Gait of Children. *Journal of Pediatric Orthopaedics*, 9(6), 702–708. <https://doi.org/10.1097/01241398-198911000-00014>
- Brown, P. (2017). *Contact Modelling for Forward Dynamics of Human Motion*. University of Waterloo.
- Brown, P., & McPhee, J. (2018). A 3D ellipsoidal volumetric foot–ground contact model for forward dynamics. *Multibody System Dynamics*, 42(4), 447–467. <https://doi.org/10.1007/s11044-017-9605-4>
- Burgess, D. J., Naughton, G., & Norton, K. I. (2006). Profile of movement demands of national football players in Australia. *Journal of Science and Medicine in Sport*, 9(4), 334–341. <https://doi.org/10.1016/j.jsams.2006.01.005>
- Coelho, J., Ribeiro, F., Dias, B., Lopes, G., & Flores, P. (2021). Trends in the Control of Hexapod Robots: A Survey. *Robotics*, 10(3), 100. <https://doi.org/10.3390/robotics10030100>
- Coulomb, C. A. (1785). The theory of simple machines. *Mémoires de Mathématique et de Physique, Présentés à l'Académie Royale Des Sciences, Par Divers Sçavans & Lûs Dans Ses Assemblées*, 10, 161–331.
- Delp, S. L., Loan, P., Basdogan, C., & Rosen, J. M. (1997). Surgical Simulation: An Emerging Technology for Training in Emergency Medicine. *Presence Teleoperators and Virtual Environments*, 6(2), 147–159. <https://doi.org/10.1162/pres.1997.6.2.147>
- Dorschky, E., Krüger, D., Kurfess, N., Schlarb, H., Wartzack, S., Eskofier, B. M., & van den Bogert, A. J. (2019). Optimal control simulation predicts effects of midsole materials on energy cost of running. *Computer Methods in Biomechanics and Biomedical Engineering*, 22(8), 869–879. <https://doi.org/10.1080/10255842.2019.1601179>
- Dunn, S., Constantinides, A., & Moghe, P. (2005). *Numerical Methods in Biomedical Engineering*. Academic Press.
- El-Halwagi, M. M. (Ed.). (2006). Overview of optimization. In *Process Systems Engineering* (pp. 285–314). Academic Press. [https://doi.org/10.1016/S1874-5970\(06\)80012-3](https://doi.org/10.1016/S1874-5970(06)80012-3)
- Eschweiler, J., Hawlitzky, J., Quack, V., Tingart, M., & Rath, B. (2017). Biomechanical model based evaluation of Total Hip Arthroplasty therapy outcome. *Journal of Orthopaedics*, 14, 582–588. <https://doi.org/10.1016/j.jor.2017.09.002>
- Esposito, E. R., & Miller, R. H. (2018). Maintenance of muscle strength retains a normal metabolic cost in simulated walking after transtibial limb loss. *PLoS ONE*, 13(1), 1–19. <https://doi.org/10.1371/journal.pone.0191310>
- Febrer-Nafria, M., Pàmies-Vilà, R., & Font-Llagunes, J. M. (2018). Foot-ground contact modelling for

- computational prediction of human walking motion. *The 5th Joint International Conference on Multibody System Dynamics*, 1–2.
- Flores, P. (2010). *MUBODYNA - Dynamic Analysis of Multibody Systems: A FORTRAN Program for Dynamic Analysis of Planar Multibody Systems - User's Manual Version 1.0*.
- Flores, P. (2022). Contact mechanics for dynamical systems: a comprehensive review. *Multibody System Dynamics*, *54*, 127–177. <https://doi.org/10.1007/s11044-021-09803-y>
- Flores, P., Ambrósio, J., Claro, J. C. P., & Lankarani, H. M. (2006). Influence of the contact–impact force model on the dynamic response of multi-body systems. *Proceedings of the Institution of Mechanical Engineers, Part K: Journal of Multi-Body Dynamics*, *220*, 21–34. <https://doi.org/10.1243/146441906X77722>
- Flores, P., Ambrósio, J., Pimenta Claro, J. C., & Lankarani, H. M. (2008). *Kinematics and Dynamics of Multibody Systems with Imperfect Joints: Models and Case Studies* (1st ed., Vol. 34). Springer Berlin, Heidelberg. <https://doi.org/10.1007/978-3-540-74361-3>
- Flores, P., & Lankarani, H. M. (2012). *Formulation for Planar Multibody Dynamics*.
- Flores, P., & Lankarani, H. M. (2016). *Contact Force Models for Multibody Dynamics* (Vol. 226). Springer International Publishing. <https://doi.org/10.1007/978-3-319-30897-5>
- Flores, P., Machado, M., Seabra, E., & Tavares da Silva, M. (2011). A Parametric Study on the Baumgarte Stabilization Method for Forward Dynamics of Constrained Multibody Systems. *Journal of Computational and Nonlinear Dynamics*, *6*(1), 1–9. <https://doi.org/10.1115/1.4002338>
- Gonçalves, F., Ribeiro, T., Ribeiro, A. F., Lopes, G., & Flores, P. (2022). A Recursive Algorithm for the Forward Kinematic Analysis of Robotic Systems Using Euler Angles. *Robotics*, *11*(1), 15. <https://doi.org/10.3390/robotics11010015>
- Güler, H. C., Berme, N., & Simon, S. R. (1998). A viscoelastic sphere model for the representation of plantar soft tissue during simulations. *Journal of Biomechanics*, *31*, 847–853. [https://doi.org/10.1016/S0021-9290\(98\)00085-2](https://doi.org/10.1016/S0021-9290(98)00085-2)
- Hall, S. J. (2012). *Basic Biomechanics* (6th ed.). McGraw-Hill.
- Hendricks, L. (2015). *Numerical Optimization*. Matlab Introduction. <https://matlab-introduction.readthedocs.io/en/latest/optimization.html#>
- Hertz, H. (1881). On the contact of elastic solids. *Journal Für Die Reine Und Angewandte Mathematik*, *92*, 156–171.
- Hunt, K. H., & Crossley, F. R. E. (1975). Coefficient of Restitution Interpreted as Damping in Vibroimpact. *Journal of Applied Mechanics*, *42*(2), 440–445. <https://doi.org/10.1115/1.3423596>

- Knudson, D. (2007). *Fundamentals of Biomechanics* (2nd ed.). Springer Science+Business Media, LLC.
- Kwiatkowski, R. (2021). *Gradient Descent Algorithm – a deep dive*. Towards Data Science. <https://towardsdatascience.com/gradient-descent-algorithm-a-deep-dive-cf04e8115f21>
- Lakany, H. (2008). Extracting a diagnostic gait signature. *Pattern Recognition*, *41*(5), 1627–1637. <https://doi.org/10.1016/j.patcog.2007.11.004>
- Lankarani, H. M., & Nikravesh, P. E. (1990). A Contact Force Model With Hysteresis Damping for Impact Analysis of Multibody Systems. *Journal of Mechanical Design*, *112*(3), 369–376. <https://doi.org/10.1115/1.2912617>
- Li, H., Chen, Y., Qiang, M., Zhang, K., Jiang, Y., Zhang, Y., & Jia, X. (2018). Computational biomechanical analysis of postoperative inferior tibiofibular syndesmosis: a modified modeling method. *Computer Methods in Biomechanics and Biomedical Engineering*, *21*(5), 427–435. <https://doi.org/10.1080/10255842.2018.1472770>
- Lopes, D. S., Neptune, R. R., Ambrósio, J., & Tavares da Silva, M. (2016). A superellipsoid-plane model for simulating foot-ground contact during human gait. *Computer Methods in Biomechanics and Biomedical Engineering*, *19*(9), 954–963. <https://doi.org/10.1080/10255842.2015.1081181>
- Máca, J., & Valášek, M. (2011). Interaction of human gait and footbridges. *Proceedings of the 8th International Conference on Structural Dynamics, EURODDYN 2011*, 1083–1089.
- Machado, M., Moreira, P., Flores, P., & Lankarani, H. M. (2012). Compliant contact force models in multibody dynamics: Evolution of the Hertz contact theory. *Mechanism and Machine Theory*, *53*, 99–121. <https://doi.org/10.1016/j.mechmachtheory.2012.02.010>
- Marques, F., Magalhães, H., Pombo, J., Ambrósio, J., & Flores, P. (2020). A three-dimensional approach for contact detection between realistic wheel and rail surfaces for improved railway dynamic analysis. *Mechanism and Machine Theory*, *149*, 103825. <https://doi.org/10.1016/j.mechmachtheory.2020.103825>
- MathWorks. (2022a). *Choose an ODE Solver*. <https://www.mathworks.com/help/matlab/math/choose-an-ode-solver.html>
- MathWorks. (2022b). *fmincon*. <https://www.mathworks.com/help/optim/ug/fmincon.html>
- MathWorks. (2022c). *Optimization Theory Overview*. <https://www.mathworks.com/help/optim/ug/optimization-theory-overview.html>
- Meireles, F. (2007). *Kinematics and Dynamics of Biomechanical Models Using Multibody Systems Methodologies (A Computational and Experimental Study of Human Gait)*. Universidade do Minho.
- Millard, M., & Kecskeméthy, A. (2015). A 3D Foot-Ground Model Using Disk Contacts. In *Interdisciplinary*

- Applications of Kinematics* (Vol. 26, pp. 161–169). Springer International Publishing, Cham.
https://doi.org/10.1007/978-3-319-10723-3_17
- Millard, M., McPhee, J., & Kubica, E. (2009). Multi-Step Forward Dynamic Gait Simulation. In C. Bottasso (Ed.), *Multibody Dynamics* (pp. 25–43). Springer Netherlands. https://doi.org/10.1007/978-1-4020-8829-2_2
- Miller, R. H., & Hamill, J. (2015). Optimal footfall patterns for cost minimization in running. *Journal of Biomechanics*, *48*, 2858–2864. <https://doi.org/10.1016/j.jbiomech.2015.04.019>
- Miller, R. H., Umberger, B. R., & Caldwell, G. E. (2012). Limitations to maximum sprinting speed imposed by muscle mechanical properties. *Journal of Biomechanics*, *45*, 1092–1097. <https://doi.org/10.1016/j.jbiomech.2011.04.040>
- Moreira, P. (2009). *Development of a Three-Dimensional Contact Model for the Foot-Ground Interaction in Gait Simulations*. Universidade do Minho.
- Moreira, P., Tavares da Silva, M., & Flores, P. (2009). Ground Foot Interaction in Human Gait: Modelling and Simulation. *7th EUROMECH Solid Mechanics Conference*, 1–13.
- Muscolino, J. E. (2017). *The Muscular System Manual: The Skeletal Muscles of the Human Body* (4th ed.). Elsevier.
- Neptune, R. R., Wright, I. C., & van den Bogert, A. J. (2000). A Method for Numerical Simulation of Single Limb Ground Contact Events: Application to Heel-Toe Running. *Computer Methods in Biomechanics and Biomedical Engineering*, *3*(4), 321–334. <https://doi.org/10.1080/10255840008915275>
- Neumann, D. A. (2010). *Kinesiology of the Musculoskeletal System: Foundations for Rehabilitation* (2nd ed.). Mosby.
- Nikravesh, P. (1988). *Computed-Aided Analysis of Mechanical Systems*. Prentice-Hall, Inc.
- Nikravesh, P. (2019). *Planar Multibody Dynamics: Formulation, Programming with MATLAB®, and Applications* (2nd ed.). Taylor & Francis, CRC Press,. <https://doi.org/10.1201/b22302>
- Oatis, C. A. (2009). *Kinesiology: The mechanics & pathomechanics of human movement* (2nd ed.). Lippincott Williams & Wilkins.
- Õunpuu, S., Davis, R. B., & DeLuca, P. A. (1996). Joint kinetics: methods, interpretation and treatment decision-making in children with cerebral palsy and myelomeningocele. *Gait & Posture*, *4*(1), 62–78. [https://doi.org/10.1016/0966-6362\(95\)01044-0](https://doi.org/10.1016/0966-6362(95)01044-0)
- Panero, J., & Zelnik, M. (1979). *Human dimension & Interior space*. Watson-Guptill Publications.
- Pérez-González, A., Fenollosa-Esteve, C., Sancho-Bru, J. L., Sánchez-Marín, F. T., Vergara, M., & Rodríguez-Cervantes, P. J. (2008). A modified elastic foundation contact model for application in 3D

- models of the prosthetic knee. *Medical Engineering & Physics*, 30(3), 387–398. <https://doi.org/10.1016/j.medengphy.2007.04.001>
- Perry, J. (1992). *Gait analysis: Normal and Pathological Function* (1st ed.). SLACK Incorporated.
- Raasch, C. C., Zajac, F. E., Ma, B., & Levine, W. S. (1997). Muscle coordination of maximum-speed pedaling. *Journal of Biomechanics*, 30(6), 595–602. [https://doi.org/10.1016/S0021-9290\(96\)00188-1](https://doi.org/10.1016/S0021-9290(96)00188-1)
- Rodrigues da Silva, M., Freitas, B., Andrade, R., Carvalho, Ó., Renjewski, D., Flores, P., & Espregueira-Mendes, J. (2021). Current Perspectives on the Biomechanical Modelling of the Human Lower Limb: A Systematic Review. *Archives of Computational Methods in Engineering*, 28, 601–636. <https://doi.org/10.1007/s11831-019-09393-1>
- Rodrigues da Silva, M., Marques, F., Tavares da Silva, M., & Flores, P. (2022). A compendium of contact force models inspired by Hunt and Crossley's cornerstone work. *Mechanism and Machine Theory*, 167, 104501. <https://doi.org/10.1016/j.mechmachtheory.2021.104501>
- Roemer, K. (2010). Biomechanical Modeling Applied To Human Movement Analysis. *XXVIII International Symposium of Biomechanics in Sports, July, 23–26*.
- Safartoobi, M., Dardel, M., & Daniali, H. M. (2021). Gait cycles of passive walking biped robot model with flexible legs. *Mechanism and Machine Theory*, 159, 104292. <https://doi.org/10.1016/j.mechmachtheory.2021.104292>
- Saraiva, L., Rodrigues da Silva, M., Marques, F., Tavares da Silva, M., & Flores, P. (2022). A review on foot-ground contact modeling strategies for human motion analysis. *Mechanism and Machine Theory*, 177, 105046. <https://doi.org/10.1016/j.mechmachtheory.2022.105046>
- Shampine, L. F., & Reichelt, M. W. (1997). The MATLAB ODE Suite. *SIAM Journal on Scientific Computing*, 18(1), 1–22. <https://doi.org/10.1137/S1064827594276424>
- Shourijeh, M. S., & McPhee, J. (2015). Foot-ground contact modeling within human gait simulations: from Kelvin-Voigt to hyper-volumetric models. *Multibody System Dynamics*, 35, 393–407. <https://doi.org/10.1007/s11044-015-9467-6>
- Siegler, S., Seliktar, R., & Hyman, W. (1982). Simulation of human gait with the aid of a simple mechanical model. *Journal of Biomechanics*, 15(6), 415–425. [https://doi.org/10.1016/0021-9290\(82\)90078-1](https://doi.org/10.1016/0021-9290(82)90078-1)
- Silva, P. C., Tavares da Silva, M., & Martins, J. M. (2010). Evaluation of the contact forces developed in the lower limb/orthosis interface for comfort design. *Multibody System Dynamics*, 24, 367–388. <https://doi.org/10.1007/s11044-010-9219-6>

- Skrinjar, L., Slavič, J., & Boltežar, M. (2018). A review of continuous contact-force models in multibody dynamics. *International Journal of Mechanical Sciences*, *145*, 171–187. <https://doi.org/10.1016/j.ijmecsci.2018.07.010>
- Standring, S. (2016). *Gray's Anatomy: The Anatomical Basis of Clinical Practice* (41st ed.). Elsevier.
- Taheri, H., & Zhao, C. X. (2020). Omnidirectional mobile robots, mechanisms and navigation approaches. *Mechanism and Machine Theory*, *153*, 103958. <https://doi.org/10.1016/j.mechmachtheory.2020.103958>
- Tavares da Silva, M. (2003). *Human Motion Analysis Using Multibody Dynamics and Optimization Tools*. Instituto Superior Técnico.
- Tavares da Silva, M., & Ambrósio, J. A. C. (2002). Kinematic data consistency in the inverse dynamic analysis of biomechanical systems. *Multibody System Dynamics*, *8*(2), 219–239. <https://doi.org/10.1023/A:1019545530737>
- Tavares da Silva, M., Ambrósio, J. A. C., & Pereira, M. S. (1997). Biomechanical Model with Joint Resistance for Impact Simulation. *Multibody System Dynamics*, *1*, 65–84. <https://doi.org/10.1023/A:1009700405340>
- Tortora, G. J., & Derrickson, B. (2010). *Introduction to the Human Body: the essentials of anatomy and physiology* (8th ed.). John Wiley & Sons, Inc.
- Trasolini, N. A., Nicholson, K. F., Mylott, J., Bullock, G. S., Hulburt, T. C., & Waterman, B. R. (2022). Biomechanical Analysis of the Throwing Athlete and Its Impact on Return to Sport. *Arthroscopy, Sports Medicine, and Rehabilitation*, *4*(1), e83–e91. <https://doi.org/10.1016/j.asmr.2021.09.027>
- Van Hulle, R., Schwartz, C., Denoël, V., Croisier, J.-L., Forthomme, B., & Brùls, O. (2020). A foot/ground contact model for biomechanical inverse dynamics analysis. *Journal of Biomechanics*, *100*, 109412. <https://doi.org/10.1016/j.jbiomech.2019.109412>
- Wan, B., & Shan, G. (2016). Biomechanical modeling as a practical tool for predicting injury risk related to repetitive muscle lengthening during learning and training of human complex motor skills. *SpringerPlus*, *5*, 441. <https://doi.org/10.1186/s40064-016-2067-y>
- Winter, D. A. (1984). Pathologic gait diagnosis with computer-averaged electromyographic profiles. *Archives of Physical Medicine and Rehabilitation*, *65*(7), 393–398. <http://www.ncbi.nlm.nih.gov/pubmed/6742998>
- Winter, D. A. (2005). *Biomechanics and Motor Control of Human Movement* (3rd ed.). John Wiley & Sons, Inc.
- Winter, D. A. (2009). *Biomechanics and Motor Control of Human Movement* (4th ed.). John Wiley & Sons,

Inc. <https://doi.org/10.1002/9780470549148>

Xie, Z., Li, L., & Luo, X. (2022). A foot-ground interaction model based on contact stability optimization for legged robot. *Journal of Mechanical Science and Technology*, *36*(2), 921–932. <https://doi.org/10.1007/s12206-022-0139-1>

Yadav, A. (2021). *How Does Gradient Descent Algorithm Work?* MATLAB Helper. <https://matlabhelper.com/blog/matlab/how-does-gradient-descent-algorithm-work/>

Appendix I – Optimizations Results

The detailed results of the optimal solution for each optimization are shown in this appendix.

Table I.1. Results obtained from the optimizations performed with three different approaches for the definition of the objective function: simulation time, objective function value, optimal solution values, circles arrangement and deformation registered for each circle

Parameters	Absolute value	Square	Cube	
	40.0839 min	1.1632 h	1.2738 h	
	$J = 69.9671$	$J = 38.8928$	$J = 24.2175$	
Circle 1	x^1 [m]	-0.0518491251470155	-0.0899999941640296	-0.0475943416457909
	y^1 [m]	-0.0393906630819456	0.0199999799924073	-0.0494671525536236
	r^1 [m]	0.0496748467669693	0.0977303604615632	0.0400000023593449
	k^1 [N/m ^{3/2}]	91472.7368523186	40000.0043727620	40000.0010899561
	c_r^1 [-]	0.931404628582939	0.300000062089286	0.949999995177022
	μ_c^1 [-]	0.288980868270326	0.182509829972697	0.299999993133613
Circle 2	x^2 [m]	0.0261047671820263	0.0174190609518387	0.0243272085466871
	y^2 [m]	-0.0273273510376784	-0.0382113955601078	-0.0417281851965196
	r^2 [m]	0.0783611313882680	0.0720788206007646	0.0692036549294389
	k^2 [N/m ^{3/2}]	81333.0275816798	79825.6914887128	73267.0053881352
	c_r^2 [-]	0.947323937846691	0.949999998772587	0.949999999722267
	μ_c^2 [-]	0.101399528305163	0.100000001700533	0.100000000241202
Circle 3	x^3 [m]	0.123487663612708	0.125999975014369	0.125959768187517
	y^3 [m]	-0.0650530286342784	-0.0628197265583963	-0.0624840250457698
	r^3 [m]	0.00528260439302679	0.00500000018642009	0.00500000004249970
	k^3 [N/m ^{3/2}]	171443.940034051	191684.178045047	187817.982784519
	c_r^3 [-]	0.830587925907759	0.733160141291290	0.669666339012370
	μ_c^3 [-]	0.256840230599321	0.233737791001910	0.206318106391331

Table I.1. (Continued)

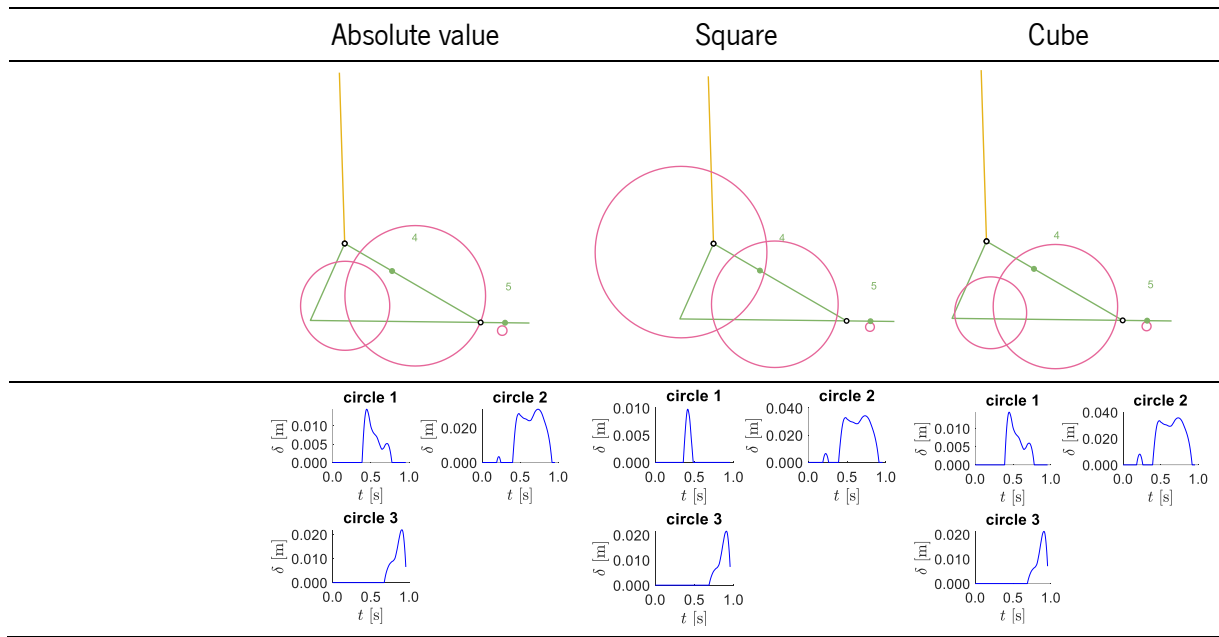
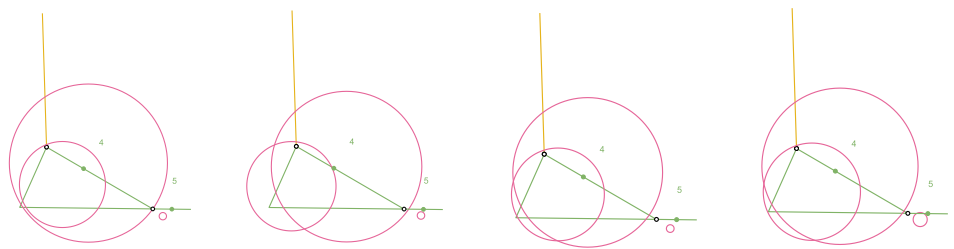


Table I.2. Results obtained from the optimizations performed with different weights for each component: simulation time, objective function value, optimal solution values, circles arrangement and deformation registered for each circle

Parameters	$w_1 = 1, w_2 = 1,$	$w_1 = 3, w_2 = 1,$	$w_1 = 1, w_2 = 3,$	$w_1 = 1, w_2 = 1,$	
	$w_3 = 1$	$w_3 = 1$	$w_3 = 1$	$w_3 = 3$	
	32.7862 min	29.4794 min	32.1823 min	42.4562 min	
	$J = 59.5477$	$J = 61.5484$	$J = 70.9911$	$J = 43.6112$	
Circle 1	x^1 [m]	-0.029880001580229	-0.059337619296876	-0.034042013063866	-0.031595684589175
	y^1 [m]	-0.022955892311147	-0.026007448205412	-0.024032853404429	-0.028344756991265
	r^1 [m]	0.061316459894652	0.062692152881704	0.062659811343786	0.066113608681935
	k^1 [N/m ^{3/2}]	358007.254664848	60163.1176785023	342746.156045324	212611.770282291
	c_r^1 [-]	0.935296915050365	0.914109243362881	0.944343239950238	0.945010565372750
	μ_c^1 [-]	0.286501513209191	0.279552166259736	0.206419885993584	0.138602808899114
Circle 2	x^2 [m]	0.006761423437602	0.017834245515927	0.005798580842639	0.006223782384759
	y^2 [m]	0.008002943431741	0.002432636467010	0.006202300863513	0.006642597503308
	r^2 [m]	0.112713483419635	0.105710777621313	0.101020058333383	0.106211528881309
	k^2 [N/m ^{3/2}]	70307.6712688777	98340.3619167409	97508.2994372973	15261.7310405757
	c_r^2 [-]	0.940367953953484	0.946279012270217	0.943032431884713	0.942345080063622
	μ_c^2 [-]	0.103806015365960	0.102463112924927	0.106488957242783	0.105399211289834

Table I.2. (Continued)

	$w_1 = 1, w_2 = 1, w_3 = 1$	$w_1 = 3, w_2 = 1, w_3 = 1$	$w_1 = 1, w_2 = 3, w_3 = 1$	$w_1 = 1, w_2 = 1, w_3 = 3$
x^3 [m]	0.113757055068767	0.123128993301128	0.118025834788009	0.116159370902503
y^3 [m]	-0.066414450909115	-0.064940279054549	-0.068388677732853	-0.064420035018166
r^3 [m]	0.005217677383433	0.005244472328703	0.005178779450060	0.009554796829983
k^3 [N/m ^{3/2}]	277616.979263205	189422.832434102	219498.147459558	201973.668286658
c_r^3 [-]	0.886596486561927	0.784537152475946	0.940100385190604	0.928128835603263
μ_c^3 [-]	0.219830233807815	0.258489349041566	0.179387756388975	0.196468650994033



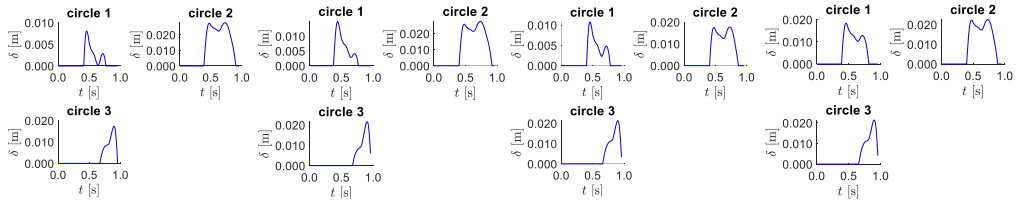


Table I.3. Results obtained from the optimizations performed with different weights for the normal contact force: simulation time, objective function value, optimal solution values, circles arrangement and deformation registered for each circle

	$w_1 = 3, w_2 = 1, w_3 = 1$	$w_1 = 5, w_2 = 1, w_3 = 1$	$w_1 = 10, w_2 = 1, w_3 = 1$
Parameters	29.4794 min	30.2760 min	42.7354 min
	$J = 61.5484$	$J = 60.9049$	$J = 58.7934$
x^1 [m]	-0.059337619296876	-0.0469197184107885	-0.0585154001863755
y^1 [m]	-0.026007448205412	-0.0245845170640143	-0.0239424833381920
r^1 [m]	0.062692152881704	0.0646152707409038	0.0653740203370361
k^1 [N/m ^{3/2}]	60163.1176785023	69586.3448506172	48042.2489410720
c_r^1 [-]	0.914109243362881	0.911374309469984	0.882438042023281
μ_c^1 [-]	0.279552166259736	0.295479423356325	0.263859158621709

Table I.3. (Continued)

	$w_1 = 3, w_2 = 1, w_3 = 1$	$w_1 = 5, w_2 = 1, w_3 = 1$	$w_1 = 10, w_2 = 1, w_3 = 1$	
Circle 2	x^2 [m]	0.017834245515927	0.0218059531078360	0.0294098094078077
	y^2 [m]	0.002432636467010	-0.00147845185636913	-0.0353340637186228
	r^2 [m]	0.105710777621313	0.101312406075407	0.0703340648984460
	k^2 [N/m ^{3/2}]	98340.3619167409	96744.1796157937	88699.1992667915
	c_r^2 [-]	0.946279012270217	0.947199052980423	0.947921235960139
	μ_c^2 [-]	0.102463112924927	0.103380713264854	0.104276949436917
Circle 3	x^3 [m]	0.123128993301128	0.121611751393944	0.125081970698060
	y^3 [m]	-0.064940279054549	-0.0656481790916719	-0.0631937504364688
	r^3 [m]	0.005244472328703	0.00554674141243399	0.00582673517748603
	k^3 [N/m ^{3/2}]	189422.832434102	166944.325204332	170058.573313197
	c_r^3 [-]	0.784537152475946	0.896998424288154	0.819276178358362
	μ_c^3 [-]	0.258489349041566	0.251471145133103	0.260281851045516

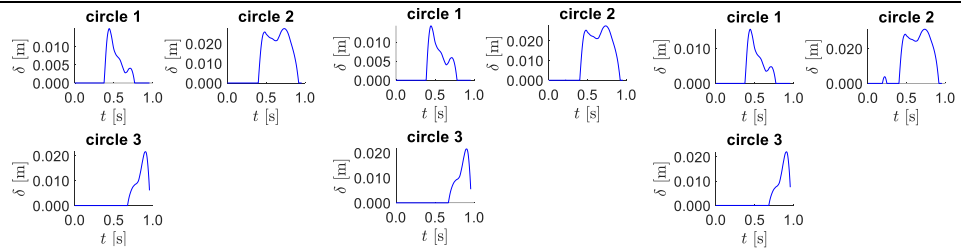
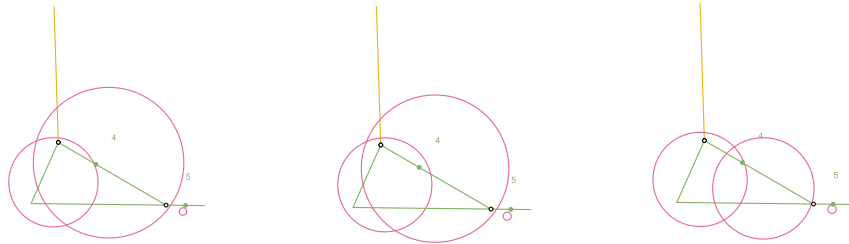


Table I.4. Results obtained from the optimizations performed with different number of circles: simulation time, objective function value, optimal solution values, circles arrangement and deformation registered for each circle

Parameters	2 circles	3 circles	4 circles	
	17.4021 min	30.2760 min	1.2829 h	
	$J = 79.7097$	$J = 60.9049$	$J = 64.4905$	
Circle 1	x^1 [m]	-0.0550836069499121	-0.0469197184107885	-0.0611893927455937
	y^1 [m]	-0.0328539618614885	-0.0245845170640143	-0.0142611978600249
	r^1 [m]	0.0554039859770372	0.0646152707409038	0.0732983634529163
	k^1 [N/m ^{3/2}]	120864.899171467	69586.3448506172	49601.2656032485
	c_r^1 [-]	0.920751696098002	0.911374309469984	0.648488223774429
	μ_c^1 [-]	0.260948402314856	0.295479423356325	0.242960685554087
Circle 2	x^2 [m]	0.0625213823559498	0.0218059531078360	0.0224714983439461
	y^2 [m]	-0.00139054287160450	-0.00147845185636913	-0.0335656104839206
	r^2 [m]	0.0929245007256398	0.101312406075407	0.0728063186785116
	k^2 [N/m ^{3/2}]	164225.792523086	96744.1796157937	88322.2374229034
	c_r^2 [-]	0.946201386508549	0.947199052980423	0.947737943723191
	μ_c^2 [-]	0.100763115872392	0.103380713264854	0.102852200808672
Circle 3	x^3 [m]	-	0.121611751393944	0.0844628271469532
	y^3 [m]	-	-0.0656481790916719	0.00361453132647913
	r^3 [m]	-	0.00554674141243399	0.0719716856305403
	k^3 [N/m ^{3/2}]	-	166944.325204332	46328.0974866249
	c_r^3 [-]	-	0.896998424288154	0.702405999449174
	μ_c^3 [-]	-	0.251471145133103	0.152925449338915
Circle 4	x^4 [m]	-	-	0.124677829048996
	y^4 [m]	-	-	-0.0641203630891000
	r^4 [m]	-	-	0.00541126679758649
	k^4 [N/m ^{3/2}]	-	-	165480.065589068
	c_r^4 [-]	-	-	0.774024159515308
	μ_c^4 [-]	-	-	0.285073898656879

Table I.4. (Continued)

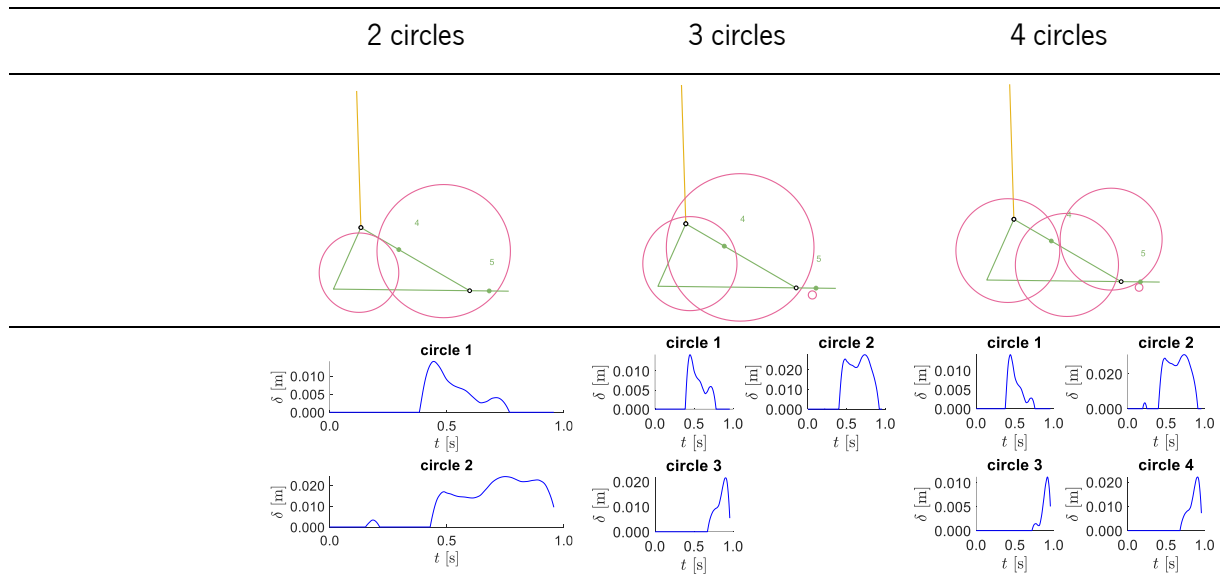


Table I.5. Initial guess, lower and upper limits and results obtained from the optimization of the friction coefficient for each circle: simulation time, objective function value, optimal solution values, circles arrangement and deformation registered for each circle

Parameters	x_0	lb	ub	7.5227 min $J = 71.6954$
Circle 1 $\mu_c^1 [-]$	0.11	0.1	0.5	0.263603413613223
Circle 2 $\mu_c^2 [-]$	0.11	0.1	0.5	0.100001329705190
Circle 3 $\mu_c^3 [-]$	0.11	0.1	0.5	0.413526498778733

